A STUDY ON ENERGY SEPARATION MECHANISM IN RANQUE-HILSCH VORTEX TUBE

(ボルテックスチューブのエネルギー分離機構に関する研究)

A Thesis Submitted for the Degree of

DOCTOR OF PHYLOSOPY

March 2015

Date of submission : 28 December 2014

Graduate School of Science and Engineering
Kagoshima University

MOHD HAZWAN BIN YUSOF

Table of Contents

Nomenclature

c_p	:	Specific heat at constant pressure [J/(kg·K)]
D	:	Inner diameter of tube [mm]
D_{vc}	:	Inner diameter of vortex chamber [mm]
d	:	Diameter of cold exit [mm]
e	:	Internal energy per unit mass [J/kg]
g	:	Gravitational acceleration [m/s^3]
h	:	Specific enthalpy [J/kg]
k	:	Thermal conductivity [W/(m·K)]
L	:	Length of tube [mm]
L_{vc}	:	Length of vortex chamber [mm]
M_{oc}	:	Representative Mach number defined as $M_{oc} = V_{\theta c}/\sqrt{\gamma RT_\infty}$
M_{omax}	:	Representative Mach number defined as $M_{omax} = V_{\theta max}/\sqrt{\gamma RT_\infty}$
M_r	:	Radial Mach number
M_z	:	Axial Mach number
M_θ	:	Tangential Mach number
$\dot{m}_{cold}$	:	Mass flow rate of cold flow [kg/s]
$\dot{m}_{hot}$	:	Mass flow rate of hot flow [kg/s]
$\dot{m}_{in}$	:	Mass flow rate of inlet [kg/s]
P_r	:	Laminar Prandtl number
P_{rt}	:	Turbulent Prandtl number
p_{in}	:	Inlet pressure [MPa]
p_{atm}	:	Atmospheric pressure [MPa]
p	:	Static pressure [MPa]
Q	:	Transferred heat per unit volume [W/m^3]
$\dot{Q}_c$	:	Cooling capacity [W]
Δq_{loss}	:	Heat loss per unit mass [J/kg]
R	:	Gas constant [J/(kg·K)]
R_e	:	Reynolds number
r	:	Radial distance [mm]
r_c	:	Radial position at $V_\theta = V_{\theta c}$ [mm]
T_{in}	:	Inlet temperature [K]
$T_{t,cold}$	:	Total-temperature at the center of cold flow [K]
$\bar{T}_{t,cold}$	:	Mixing temperature of cold flow [K]
$\bar{T}_{t,hot}$	:	Mixing temperature of hot flow [K]
$\Delta T_{t,cold}$	:	Temperature differences of cold flow (center) [K]
$\Delta \bar{T}_{t,cold}$	:	Temperature differences of cold flow (mixing) [K]

$\Delta\bar{T}_{t,hot}$: Temperature differences of hot flow (mixing) [K]
T_s : Static temperature [K]
T_0 : Total temperature [K]
T_e : Measured temperature at sonic nozzle exit [K]
T_{atm} : Ambient temperature [K]
t : Time [s]
V_r : Radial velocity [m/s^2]
V_θ : Tangential velocity [m/s^2]
$V_{\theta c}$: Tangential velocity of Rankine vortex [m/s^2]
$V_{\theta max}$: Maximum tangential velocity [m/s^2]
V_z : Axial velocity [m/s^2]
v_{in} : Flow velocity at inlet [m/s^2]
v_{cold} : Velocity of cold flow [m/s^2]
v_{hot} : Velocity of hot flow [m/s^2]
W_1 : Work done by pressure gradient on fluid element [W/kg]
W_2 : Compression work done by pressure gradient on fluid element [W/kg]
W_3 : Work done by viscous shear force [W/kg]
W_4 : Heat generated in fluid element [W/kg]
x : Distance from cold exit along center line [mm]
x_s : Length of reversed flow [mm]
z : Axial distance [mm]
z_{hot} : Height difference between hot exit and inlet [m]

Greek letters

ε : Cold fraction
Γ_∞ : Vortex circulation
γ : Specific heat ratio
η_{sep} : Energy separation efficiency
η_{flux} : Energy separation flux energy
η_{ex} : Exergy efficiency
η_{is} : Isentropic efficiency
ρ : Density [kg/m^3]
ρ_∞ : Density at far distance [kg/m^3]
σ : Normal stress [Pa]
τ : Tangential stress [Pa]
μ : Viscous coefficient[Pa·s]
Φ : Energy dissipation function [W/ m^3]
θ : Angle of total temperature probe [°]

Figure captions

Table captions

Abstract

A vortex tube (VT) is a simple and useful fluid dynamic device, used to obtain both cold and hot flows from compressed gas at room temperature. It can produce a cold flow measuring around −30°C, and a hot flow of up to around 130°C. Until now, the theory and model analysis of the energy/temperature separation inside of VT is proposed by a number of researchers. From those theories, it is generally accepted that the generation of the cold flow is caused by an adiabatic expansion, which occur after a compressed gas flows through an inlet nozzle. However, details about the physics of the cold flow generation, from the fluid dynamics view point still remain unclear.

The objective of this study is to clarify the energy separation mechanism (ESM) of VT. Therefore, in order to accomplish this objective, experimental and analytical studies were carried out. In order to clarify the flow structure of the cold exit flow, the total temperature and Pitot pressure of a cold flow center were measured. In addition, two simple flow visualization techniques were used to observe the reversed flow at the cold exit. The mixing temperature of cold and hot flows were also measured to clarify the performance of VT used in this research.

In Chapter 1, the basic idea about a VT, such as its history, the types, the example of usage, and the advantages/disadvantages of a VT is introduced. A proposed flow pattern inside a Counter-flow VT is also explained. In the literature section, the researches on the geometrical optimization of the VT, and the flow pattern inside a VT are included with a discussion on the contrary points of the researches. The objectives of this thesis are also described in this chapter.

Chapter 2 describes the experimental apparatus and procedures of the total temperature/pressure measurement methods, and the flow visualization techniques. The specifications of the equipment and measurement devices are shown in this chapter. There are two simple flow visualization techniques. Both techniques use needle and oil paint droplet. The first technique uses an oil paint droplet, on a 0.75mm-diameter needle. The oil paint droplet on the needle is positioned along the centerline of the cold flow. The movement of the oil paint droplet represents the flow direction of the cold flow. Another technique uses a 0.70mm-diameter needle with 10 small holes which can exudate colored oil (exudation needle). The exudation needle is inserted into the cold flow along the centerline. Then the colored oil is injected to the exudation needle little by little and exuded from the small holes. The flow direction of the colored oil on the exudation needle represents the flow direction of the cold flow.

In Chapter 3, the development of total temperature probe with the objective

and structure of the probe is explained. Those probes are named as Type 1, 2, and 3. An evaluation experiment is conducted using the Type 1, 2, and 3 to determine the effects of probe angle along the centerline of a sonic jet nozzle on the measurement accuracy. Results show that the largest measurement error for Type 1, 2, and 3 are $-1.3°C$, $-1.1°C$, and $-0.7°C$, respectively. From these results, the effect of the angle of the thermocouple on the total temperature measurement is negligibly small.

Chapter 4 reports the results of total temperature/pressure measurements and flow visualization at cold exit. The experiments of the effects of the cold fraction on the measurement were carried out with the Type 3 total temperature probes and Pitot pressure probe. From the results, a negative and positive gauge pressure regions are measured. It implies the possibility of a direct/reversed flow at the cold exit. To clarify the flow direction, two kinds of flow visualization are conducted. The flow direction of the cold flow is determined by the movement of the oily paint droplet. From the results, a reversed flow is observed around the center of cold exit at a smaller cold fraction. The length of reversed flow increases as the cold fraction decreases, which implies the decrease in the pressure at the core of the vortex chamber. A lower pressure in the vortex chamber means a lower static/total temperatures at the core of vortex chamber and a higher static/total temperatures at the outer region of the vortex in the vortex chamber. This is the effect of cold fraction on the EMS at an arbitrary inlet pressure. When the inlet pressure increases at an arbitrary cold fraction, the tangential velocity increases, which results in a lower static/total temperatures at the core of the vortex chamber and a higher static/total temperatures at the outer region of the vortex in the vortex chamber.

Chapter 5 describes a mathematical model analysis of compressible vortex flow with a review of some literatures. The basic equations, the laminar vortex solutions, turbulent vortex solutions, and problems with VAB model are explained. The improvement of the VAB model is conducted by replacing the laminar Prandtl number with a laminar plus turbulent Prandtl numbers. The results show that the total temperature is roughly independent of the summation of laminar and turbulent Prandtl numbers. The EMS in a turbulent compressible vortex is discussed and proposed, by examining the VAB model. The results show that a hotter gas in the peripheral region of the vortex is mainly caused by heat generated by viscous dissipation, and colder gas in the vortex core is mainly generated by viscous shear work done on the surface of the fluid element to the surrounding gas.

Finally, the conclusions of this study based on the implementation of objectives are summarized in Chapter 6.

1. Introduction

1.1 Introduction of vortex tube

A vortex tube (VT) is a simple and useful fluid dynamic device, used to obtain both cold and hot flows from a compressed gas at room temperature. It can produce a cold flow measuring around −30°C, and a hot flow of up to around 130°C. In 1930's, Ranque was the first to have discovered the energy/temperature separation phenomenon [1]. The first invented vortex tube by Ranque is shown in Fig. 1.1. Later in 1947, the flow mechanism of the vortex tube was investigated by Hilsch[2]. Since then, the vortex tube is also known as The Ranque-Hilsch Vortex Tube (RHVT).

There are a lot of advantages to VT, such as being light, small, with no moving parts, no need for maintenance, and an instant supply of cold flow. But, VT has low thermal efficiency and low coefficient of performance (COP), which is defined by the following equation;

$$\mathrm{COP}=\frac{\varepsilon c_p\left(T_{in}-\bar{T}_{t,cold}\right)}{\frac{\gamma}{\gamma-1}RT_{in}\left[\left(\frac{p_{in}}{p_{atm}}\right)^{\frac{\gamma-1}{\gamma}}-1\right]} \tag{1.1}$$

where ε is the cold fraction, c_p is the specific heat at constant pressure, T_{in} is the inlet temperature, $\bar{T}_{t,cold}$ is the mixing temperature of cold flow, γ is the specific heat ratio, R is the gas constant, p_{in} is the inlet pressure, and p_{atm} is the atmospheric pressure.

Figure 1.2 shows the comparison of COP between VT and other conventional cooling devices. As shown in the figure, the COP of VT is much lower compared to other cooling devices. But, compared to other conventional cooling devices, VT has a lot more merits to overwhelm the disadvantage, such as being small, lightweight, cheap, environmentally-friendly (no need for refrigerant), maintenance free (no moving part), and using a non-explosive device (no need of electrical power input). The VT has been mainly used as a device to cool small area, for example, electrical devices, thermal sensors, controlling cabins, cutting tools and areas under thermal stresses [3]. In addition to that, VT is also expected to be used

as an oxygen collector of aero-propulsion engine for a subsonic-to-supersonic vehicle in in-flight condition [4], or as a device to clean exhaust gas of an internal combustion engine [5] as shown in Figs. 1.3 and 1.4, respectively.

There are 2 types of VT as shown in Fig. 1.5. Figure 1.5(a) is Uni-flow VT which consists of a vortex chamber, multiple or a single inlet nozzle, a control valve, and a tube. The center of the control valve at the end of the tube is an exit where a cold flow is discharged (cold exit). The peripheral area of the control valve is another exit where a hot flow is discharged (hot exit). Figure 1.5(b) is Counter-flow VT which consists of a vortex chamber, multiple or a single inlet nozzle, a control valve, and a tube. The cold exit is located at the center of the tube near inlet nozzle and hot exit is located at the peripheral of control valve at the other end. According to previous researches [6-7], the performance of counter-flow VT is better than the uni-flow VT. Therefore, in this research, I focus on counter-flow VT.

Next, a generally thought to occur flow pattern inside the Counter-flow VT is explained. As was shown in Fig. 1.5(b), compressed air enters a VT through a single or multiple tangential nozzles, and a high-speed vortical flow is generated in the vortex chamber. A part of the rotational flow follows the tube wall towards the opposite end; hot end. Then, this flow exits as a hot flow at the hot exit. The core flow, is forced back towards the vortex chamber by a control valve, and exits as a cold flow at the cold exit. The temperatures of cold and hot flows can be changed by adjusting a cold fraction ε, which is a ratio of the mass flow rate of a cold flow, $\dot{m}_{cold}$, to the inlet mass flow rate, $\dot{m}_{in}$;

$$\varepsilon = \frac{\dot{m}_{cold}}{\dot{m}_{in}} \tag{1.2}$$

The cold fraction is adjusted by axially moving the control valve left or right. From the definition of Eq.(1.2), the cold fraction value varies from 0 to 1. Cold fraction ε = 0 means, no flow exits from the cold exit, and ε = 1 means all flow inside the tube is discharged from the cold exit. A smaller value of the cold fraction produces a lower temperature of the cold flow, and a larger value of the cold fraction produces a higher temperature, closer to inlet temperature, of the cold flow [8]. For the hot flow, lower value of cold fraction produces a lower temperature of the hot flow, closer to inlet temperature, and higher value of cold fraction produces

higher temperature of the hot flow [8]. Therefore, to obtain a lower temperature of cold flow, the value of cold fraction should be smaller, and to obtain a higher temperature of hot flow, the value of cold fraction should be larger.

The performance of VT is affected by the parameter of inlet nozzle, tube, control valve etc. Nowadays, many researchers are focusing on improving the performance of VT by changing geometrical parameters of VT. According to research works conducted in the past [6, 9-11], there are several ways to evaluate the performance of energy separation of the VT, in addition to COP in Eq.(1.1). For example, temperature difference $\Delta T_{t,cold}$, $\Delta \bar{T}_{t,cold}$ and $\Delta \bar{T}_{t,hot}$, total temperature difference $\Delta \bar{T}_t$, cooling capacity $\dot{Q}_c$, energy separation efficiency η_{sep} [9], energy separation flux energy η_{flux} [10], exergy efficiency η_{ex} [6], and isentropic efficiency η_{is} [11] defined by the following equations;

Temperature difference (inlet-cold)

$$\Delta T_{t,cold} = T_{in} - T_{t,cold} \quad \text{; Center temperature} \tag{1.3}$$

$$\Delta \bar{T}_{t,cold} = T_{in} - \bar{T}_{t,cold} \quad \text{; Mixing temperature} \tag{1.4}$$

Temperature difference (hot-inlet)

$$\Delta \bar{T}_{t,hot} = \bar{T}_{t,hot} - T_{in} \tag{1.5}$$

Total temperature difference (hot-cold)

$$\Delta \bar{T}_t = \bar{T}_{t,hot} - \bar{T}_{t,cold} \tag{1.6}$$

Cooling capacity

$$\dot{Q}_c = \dot{m}_{cold} c_p \Delta \bar{T}_{t,cold} \tag{1.7}$$

Energy separation efficiency

$$\eta_{sep} = \frac{T_{in} - \bar{T}_{t,cold}}{\frac{v_{in}^2}{2c_p} + T_s} \tag{1.8}$$

Energy flux separation efficiency

$$\eta_{flux} = \frac{\dot{m}_{cold}}{\dot{m}_{in}} \times \frac{c_p\left(T_{in} - \bar{T}_{t,cold}\right)}{\frac{\gamma}{\gamma-1} R T_{in}\left[\left(\frac{p_{in}}{p_{atm}}\right)^{\frac{\gamma-1}{\gamma}} - 1\right]} = \text{COP} \tag{1.9}$$

Exergy efficiency

$$\eta_{ex} = \frac{\sum \dot{E}_{out}}{\sum \dot{E}_{in}} = \frac{\sum \dot{E}_{out,cold} + \sum \dot{E}_{out,hot}}{\sum \dot{E}_{in}} \tag{1.10}$$

where,

$$\sum \dot{E}_{out,cold} = \dot{m}_{cold}\left[c_p(\bar{T}_{t,cold} - T_{atm}) - T_{atm}\left(c_p ln\frac{\bar{T}_{t,cold}}{T_{atm}} - Rln\frac{p_{cold}}{p_{atm}}\right)\right] + \dot{m}_{cold}\frac{v_{cold}^2}{2}$$

$$\sum \dot{E}_{out,hot} = \dot{m}_{hot}\left[c_p(\bar{T}_{t,hot} - T_{atm}) - T_{atm}\left(c_p ln\frac{\bar{T}_{t,hot}}{T_{atm}} - Rln\frac{p_{hot}}{p_{atm}}\right)\right] + \dot{m}_{hot}\frac{v_{hot}^2}{2} + \dot{m}_{hot}gz_{hot}$$

$$\sum \dot{E}_{in} = \dot{m}_{in}\left[c_p(T_{in} - T_{atm}) - T_{atm}\left(c_p ln\frac{T_{in}}{T_{atm}} - Rln\frac{p_{in}}{p_{atm}}\right)\right] + \dot{m}_{in}\frac{v_{in}^2}{2}$$

Isentropic efficiency

$$\eta_{is} = \frac{T_{in} - \bar{T}_{t,cold}}{T_{in}\left[1 - \left(\frac{p_{atm}}{p_{in}}\right)^{\left(\frac{\gamma-1}{\gamma}\right)}\right]} \tag{1.11}$$

where T_{in} is the inlet temperature, $T_{t,cold}$ is the total temperature of cold flow at the center of cold exit, $\bar{T}_{t,hot}$ is the mixing temperature of hot flow, v_{in} is the flow velocity at inlet, T_s is the static temperature of expansion gas at vortex chamber, T_{atm} is atmospheric temperature, $\dot{m}_{hot}$ is the mass flow rate of hot flow, v_{cold} is the velocity of cold flow, v_{hot} is the velocity of hot flow, g is gravitational acceleration, z_{hot} is the height difference between the hot exit and the inlet

Until now, the theory and model analysis of the energy/temperature separation inside VT is proposed by a lot of researchers [12-15]. From those theories, it is generally accepted that the generation of the cold flow is caused by an adiabatic expansion, which occurs after a compressed gas flows through an inlet nozzle. However, details about the physics of the cold flow generation, from the fluid dynamics view point still remain unclear. The theory on the generation of the hot flow is also still incomplete. The vortex flow in VT produces a pressure distribution inside VT where the core pressure of the tube is lower, and the peripheral pressure is higher. According to the theory of fluid dynamics, the lower pressure is caused by expansion of compressed gas, which generates a colder flow. Inversely, a higher pressure is produced by compression of gas, which generates a hotter flow. However, according to the past experimental and numerical researches [16-17], the pressure at the peripheral region of the tube is actually lower than the inlet pressure, which denies the theory of the compression inside the tube. Therefore, the theory of the energy/temperature separation inside VT still remains unclear and debatable.

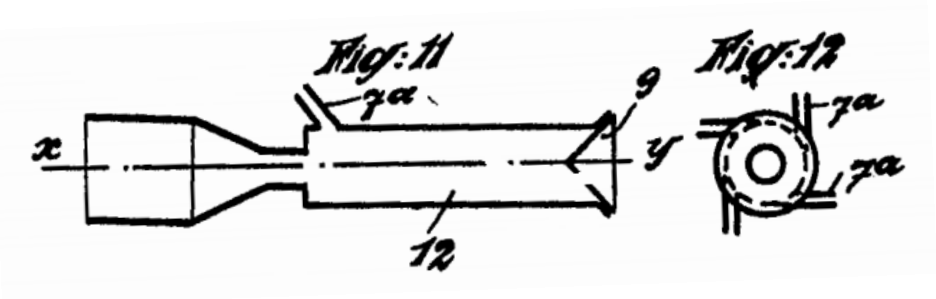

Fig. 1.1 Vortex tube invented by George Ranque [18]

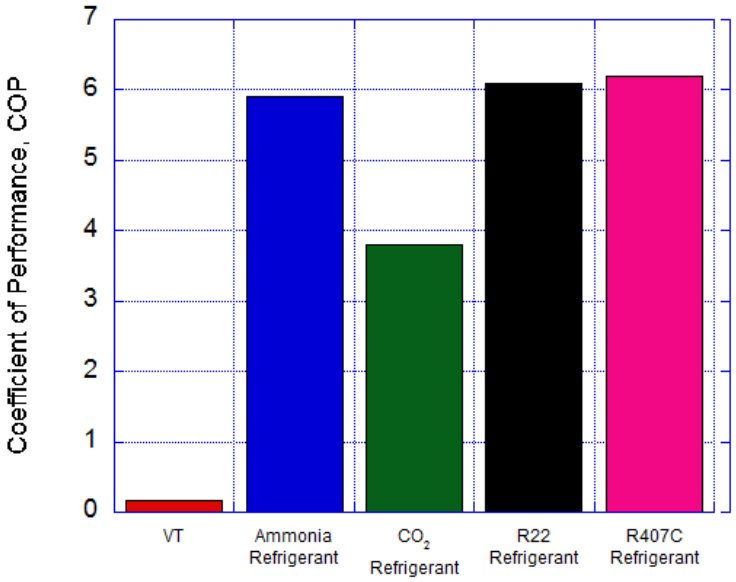

Fig. 1.2 Comparison of COP between vortex tube and other cooling devices [19]

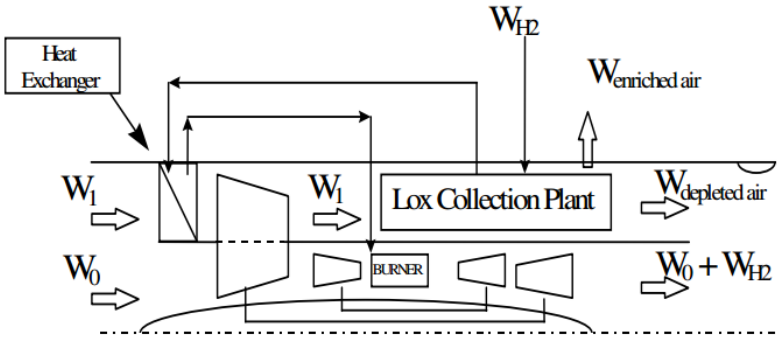

Fig. 1.3 Integrated liquid-O_2 collector plant architecture [4]

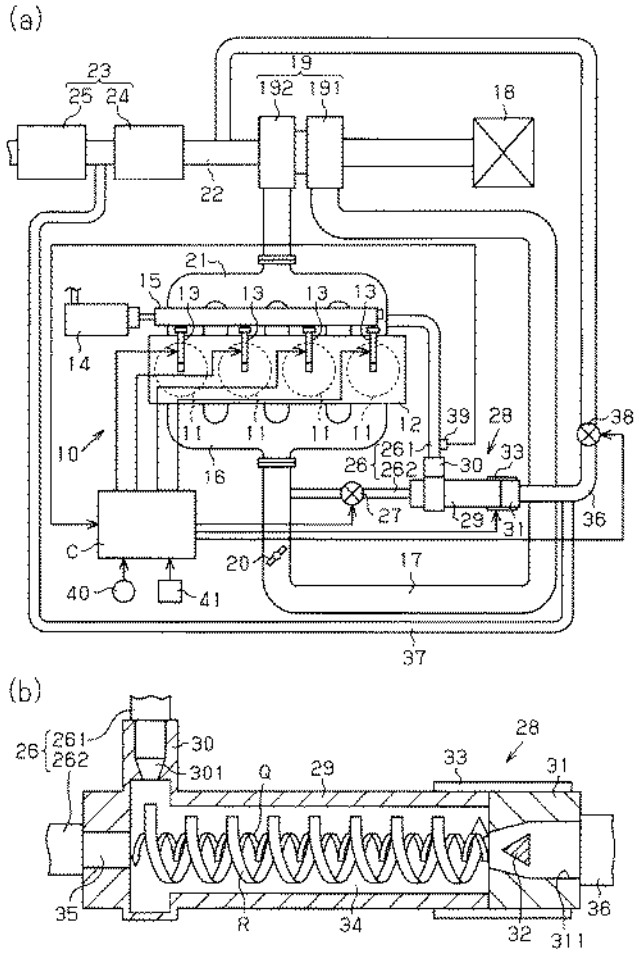

Fig. 1.4 Application of VT as an exhaust device in internal combustion engine [5]

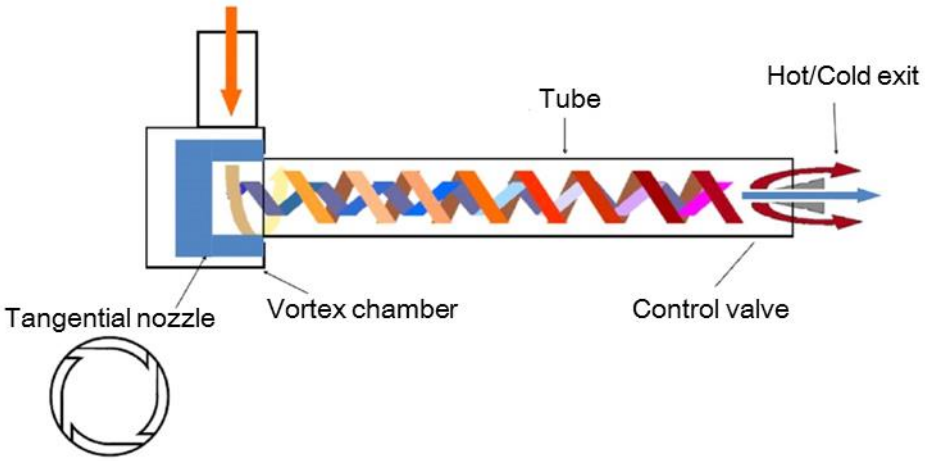

(a) Uni-flow type

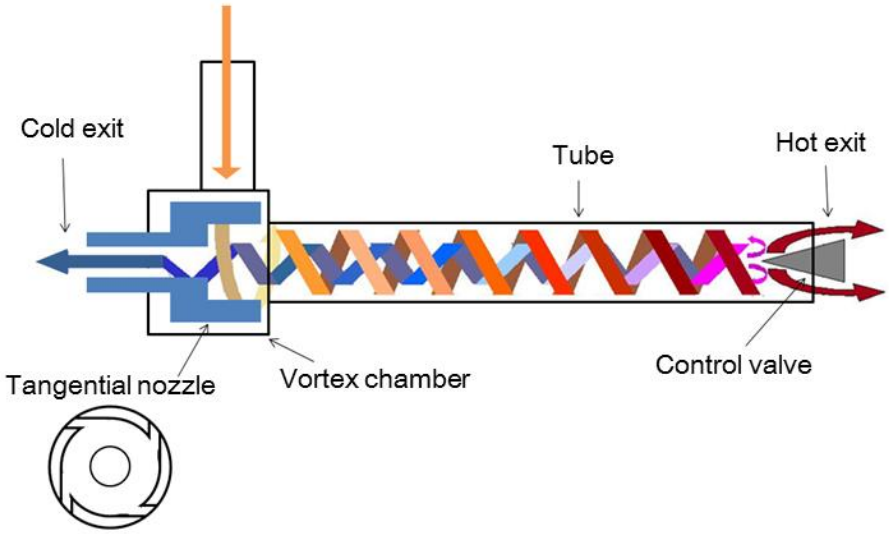

(b) Counter-flow type

Fig. 1.5 Classification of vortex tube

1.2 Literature review

Several numerical and experimental works had been done to investigate the performance of the VT. Takahama[20] studied the energy separation efficiency, velocity distribution, and temperature distribution inside the tube, experimentally. He reports a formula for the profiles of velocity, temperature and energy of air flowing in a standard vortex chamber. Later, Takahama et al.[9] studied the effects of divergent tube with a divergent angle of 1.75° on the performance of VT. They report that the performance of divergent vortex chamber is better than the straight tube with the same length of tube. But, they studied on only one divergent vortex chamber without changing the angle of the divergent. Saidi et al.[21] studied the effects of parameter on the performance of VT by changing diameter and length of main tube, diameter of cold exit, shape of entrance nozzle, and types of working gas. They used a tube with an inner diameter of 18 mm. They report the optimum value of length to inner diameter ratio (L/D) is 55.5, cold exit diameter is 50% of inner diameter of tube, and diameter of inlet nozzle is 3.5 mm with 3 inlets. They also report that helium is better than oxygen or air as the working gas for a higher performance of VT. Behera et al.[22] performed a Computational Fluid Dynamics (CFD) analysis and experimental investigation to optimize the geometry of VT. They reports that the optimum size of the cold exit is 58% of the diameter of the tube. Nimbalkar[23] performed similar experiments to determine the optimum size of the cold exit. He reports that the optimum diameter of the cold exit is 50% of the diameter of the tube, which is same as Saidi et al.[21] but 8% smaller than the result of Behera et al.[22]. Wu et al.[24] proposes a new nozzle with an equal Mach number gradient and flow velocity at the inlet nozzle. They report that the cooling effect with the new nozzle is improved compared to the conventional nozzle. Aydin et al.[8] proposed a new helical type of vortex generator for a counter-flow VT. They report that the new helical type of vortex generator has an obvious and superior effect on temperature separation with a temperature difference between cold flow and inlet flow is up to 45.5℃ at inlet pressure of 0.5MPa. Markal et al.[25] investigated the effect of the control valve's head angle of a counter-flow VT. They report that this effect is generally negligible in a large length to tube inner diameter ratio. Chang et al.[26] investigated the effect of a divergent vortex chamber to the performance of the VT, just like Takahama et al.[9], with variation

of divergent angle of tube. They report that the performance of the VT can be improved by using the divergent tube with a divergent angle not more than 6°. Avci[27] studied the effects, of nozzle aspect ratio and the nozzle number of a helical vortex generator, on the performance of the VT. He reports that the temperature difference increases with increasing nozzle aspect ratio and single nozzle leads to better performance than the VT with 2 and 3 nozzles.

Uluer et al.[28] used an artificial neural network (ANN) for modeling the performance of the counter flow VT. They performed an experiment using a VT with 2, 3, 4, 5, and 6 inlet nozzles. The input parameters are inlet pressure, the inlet nozzle number and the cold fraction. The obtained temperature data is used as output parameters for the ANN. They report that ANN model can be trained to provide satisfactory estimations of temperature gradient. Korkmaz et al.[29] also used ANN to predict the performance of VT. They modeled the VT with ANN using experimental data to study the effects of conical valve angle, inlet pressure and length of the tube to the performance of VT. They report that ANN can be used to predict the performance of VT and is a reliable option in modeling the thermo-fluids systems. Khazaei et al.[30] investigated the effects of gas properties and geometrical parameters on performance of a vortex tube using a CFD model. They report that the cold temperature difference increases by using working gas with a larger specific heat ratio, and the hot exit dimension and its shape have a negligible effect on temperature distribution in a VT.

Several researchers studied the flow structure inside VT numerically and experimentally. Xue et al.[31] studied the flow structure in a VT, which is immerged under water, using air bubble as seeding particle. They used water as the working fluid, so no compression and expansion occur inside the tube. They report the axial and swirl velocity of the flow inside the tube and the image of flow visualization inside the tube. Later, Xue et al.[16] used a Cobra probe to measure the pressure inside a large VT with an inner diameter of 60 mm and a length 2000 mm. They calculate the velocity of flow inside VT based on the measured pressures. They report that the gradually changed static pressure distributions along the VT axis indicates the transformation of a forced vortex at cold exit side to a free vortex at hot exit side. They also proposed a flow pattern with a stagnation point exists inside VT. Behera et al.[17] numerically investigated the flow behavior and energy

separation inside VT. They report a different flow pattern from Xue et al.[16] with no stagnation point inside the tube.

Several researchers published review papers on the VT. Eiamsa-ard et al.[3] summarized the experimental, theoretical, analytical and numerical studies on VT. They report a guideline of constructing a high performance VT and inconsistencies between each research. Xue et al.[32] published a critical review of temperature separation in a vortex tube. They summarized the theories and main factors of the energy separation mechanism (ESM) and proposed the important point for clarifying the ESM.

From the literatures reviewed in this section, it can be understood that the performance of VT is affected by the parameters including inlet nozzle number, cold exit diameter, inlet diameter, tube length, etc. At this point, the optimal geometry to obtain a higher performance of counter flow VT is experimentally well known. Even with similar parameters, the results obtained by each researcher are different with each other. But, the optimal geometry of the counter flow VT is similar to each other. On the contrary, the flow pattern inside the tube, which is a key point of the ESM, is still remaining unclear. One of the reasons of this will be attributed to the difficulty in measuring a vortical high-speed flow in a small radius tube. It can be concluded from the literature review that the optimal geometry of counter flow VT is obtained experimentally, but the ESM is remaining unclear even with a lot of researches which has conducted in the past 80 years.

1.3 Objective

In this thesis, I perform experimental and analytical studies of VT in order to clarify the ESM of counter flow VT. This is because the author believes that deeper understanding of ESM in VT enables us to raise various energy related efficiencies introduced in this chapter, leading VT to apply to a wider engineering field, including refrigeration. However, the ESM of VT is not fully understood despite of many research works conducted in the past. Several researchers have experimentally, theoretically and numerically studied, the velocity, temperature and pressure inside VT [16-17], proposing several mechanism about thermal energy separation. However, the flow discharged from the cold exit has not been studied well.

In this research, a special attention is paid to the cold flow discharged from the cold exit. This is because the energy separation in the VT is expected to occur mainly in a vortical flow in a vortex chamber. Therefore, the flow structure and temperature distribution in the cold flow, which is close to the vortex chamber, is expected to be closely related to that of the vortical flow in the vortex chamber for obtaining insights about the ESM in the VT. The objectives of this study are summarized as follows:

(1) To clarify the flow structure of vortical cold flow at the cold exit by the measurement of total temperature and Pitot pressure, and flow visualization.

(2) To clarify the relationship between the structure of cold flow and EMS in the VT, especially in the vortex chamber.

(3) To clarify the physics about the EMS occurring in a turbulent compressible vortex by mathematical model analysis, in order to assist the understanding of ESM in VT.

1.4 Thesis outline

In order to accomplish the objectives of this study, experiments and mathematical model analysis are carried out. The outline of the chapters in this thesis is given as follows;

Chapter 1 introduces the basic idea about a VT; explaining the history, the types, the example of usage, and the advantages/disadvantages of a VT. A proposed flow pattern inside a counter flow VT is also explained. In the literature section, the researches on the geometrical optimization of the VT, and the flow pattern inside a VT are included with a discussion on the inconsistencies about the results obtained by different researchers. Then, the objectives of this thesis are also expressed in this chapter.

Chapter 2 describes the experimental apparatus and procedures of the total temperature/pressure measurements at the cold exit, and the flow visualization techniques. The specifications of equipment and measurement devices are shown in this chapter. In flow visualization techniques, a needle with 10 holes, and an oil paint droplets are used.

Chapter 3 explains the development of total temperature probe with the objective and structure of the probes. An evaluation experiment is conducted to determine the measurement accuracy of the originally developed probe and the results are discussed.

Chapter 4 reports the results of total temperature/pressure measurements and flow visualization at the cold exit. The experiments were carried out with the invented total-temperature probe and Pitot pressure probe. The effects of the cold fraction on the measurement results are explained. The flow direction of the cold flow is determined by flow direction of the oil paint droplet on the needle. The movement of the oil paint is recorded with a video camera and a high speed camera. From these results, the expected flow pattern is discussed.

Chapter 5 describes a mathematical model analysis of isolated unconfined compressible vortex flow with a review of some literatures. The basic equations, the laminar vortex solutions, turbulent vortex solutions, and problems with VAB model are explained. The improvement of the VAB model is conducted by replacing the laminar Prandtl number with a laminar plus turbulent Prandtl numbers. The EMS in a turbulent compressible vortex is discussed and proposed,

by examining the VAB model in detail.

Chapter 6 summarizes the conclusions of this study based on the implementation of objectives.

2. Experimental Apparatus and Methods

In this chapter, experimental apparatus used in this research is explained. In addition, pressure/temperature measurement methods and flow visualization methods are also described.

2.1 Experimental apparatus

Figure 2.1 shows a schematic diagram of the experimental setup of counter-flow VT used in this study. Dehumidified compressed air up to 1MPa is continuously supplied to air tanks of $1m^3 \times 2$ units. Then, the air is supplied to the vortex chamber of ⑧ VT, through ① mass flow meters, ③ stagnation chamber and ⑤ pressure control valve. Then, a vortical flow is generated through the inlet tangential nozzles in the vortex chamber. The cold flow exit is located near the inlet of the tangential nozzles, the left end of ⑧ VT in the figure. The hot flow exit is at the opposite end of the VT. The inlet temperature and pressure were measured by ④ temperature/humidity sensor and ⑦ digital manometer, respectively. The inlet pressures and mass flow rate were manually controlled by ⑤ pressure control valve. The flow temperature discharged from the cold and hot exit was measured by ⑨ total temperature probe. The pressure discharged from the cold exit was measured by ⑪ Pitot pressure probe. The distances between the tip of the total temperature probe and Pitot pressure probe to the cold exit plane were adjusted by a traverser. The measured temperature was displayed by ⑥ temperature/humidity indicator and ⑩ temperature indicator, and these data was recorded manually. The analog voltage signals from the ⑬ positive pressure sensor, ⑭ negative pressure sensor, and ⑦ digital manometer were converted to digital signals by ⑮ A/D converter and were sent to ⑯ personal computer. The specification of the equipment and devices used in this experiment are shown in Table 2.1.

The dimensional details of the VT used in this research are shown in Fig. 2.2. It has an inner vortex chamber diameter D_{vc} = 26mm with a length L_{vc} = 5mm, inner tube diameter D = 14mm, a length to inner diameter ratio L/D = 20, a cold exit diameter d = 5mm, and four tangential nozzles. The dimension of this VT, L/D = 20 and $d/D \approx 0.36$, is based on the optimal geometry of VT from Ref.[33]. It should be noted here that the definition of the tube length, L, may somewhat differs

from researchers to researchers. All the parts of the VT used in this study are made of stainless steel.

Figure 2.3 shows the tangential nozzle with cold exit pipe, which is used as a vortex generator. The cold exit pipe is located on the back side of the tangential nozzle with a length of 67mm. The cold gas flows through the cold exit pipe and exits the tube. As shown in this figure, the rectangular cross sectional area of the tangential nozzle is width 4mm $\times$ height 1.5mm $\times$ 4 nozzles = 24mm^2.

Figure 2.4 shows the calculated operating time of a compressed gas, which is stored in 2m^3 tank with pressure of 1MPa and temperature of 300K as initial conditions. In this calculation, compressed air enters the VT at a regulated inlet pressure setting from 0.3 to 0.6 MPa. Note that in this calculation, the flow is assumed to be choked at the tangential nozzle (throat) during the operation, and the air in the tank is assumed to experience isentropic change of pressure and density. This figure shows the maximum operating time of the VT when fully stored air in the tank is consumed without supplying air to the tank from the compressor. The figure shows that the operating time varies from 13.3 to 3.5 minutes, depending on the regulated inlet pressure. In this research, however, the compressor is kept running while performing every experiments.

Figure 2.5 shows the control valve, which is used to adjust the mass flow rate of hot and cold flow that are discharged from the hot exit and cold exit, respectively.

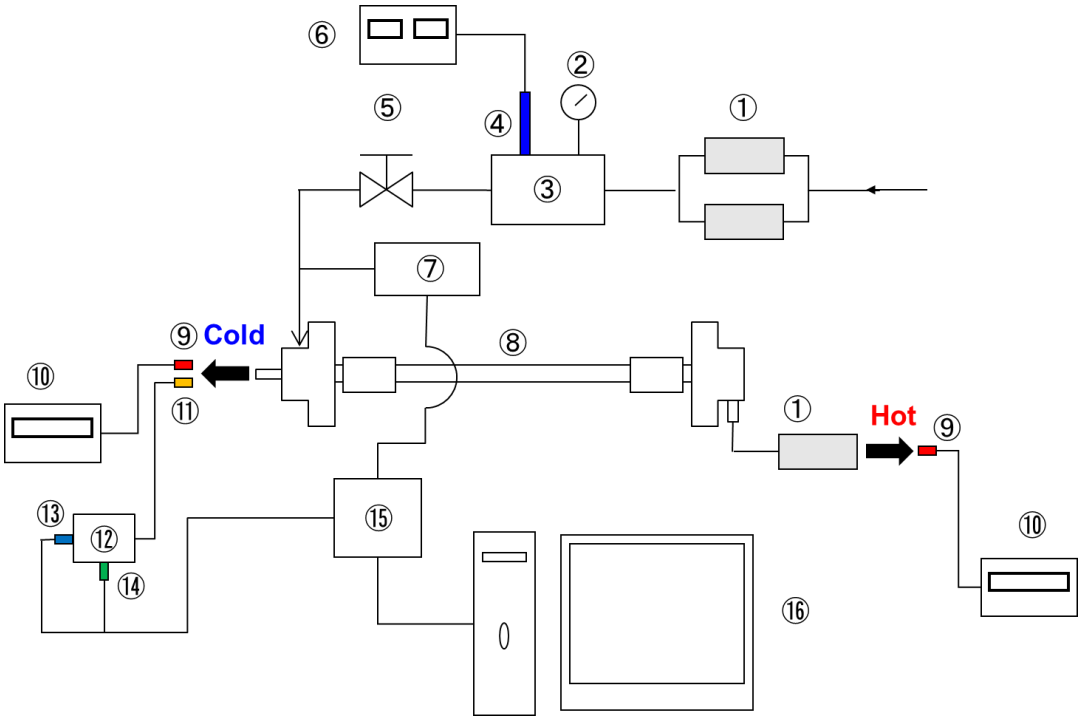

Fig. 2.1 Experimental setup for temperature and pressure measurement of VT ; ①Mass Flow Meter, ②Bourdan Tube Pressure Gauge, ③Stagnation chamber, ④ Temperature/humidity sensor, ⑤ Valve, ⑥ Temperature/humidity indicator, ⑦Digital manometer, ⑧Vortex tube, ⑨Total temperature probe, ⑩Temperature indicator, ⑪Pitot pressure probe, ⑫Stagnation chamber, ⑬Positive pressure sensor, ⑭Negative pressure sensor, ⑮A/D converter, ⑯Personal computer.

Table 2.1 Specification of equipment and devices used in this experiment

(1) Compressor	Maker : HITACHI Model code : PBD-5.5HB6 Power : 5.5kW Max. pressure : 1.37MPa Flow rate : 550L/min
(2) Air dryer	Model code : HDF-25HXA Power : 250W Max. pressure : 1.37MPa
(3) Pressure reducer	Maker : YAMATOSANGYOU Co. Model code : YM-303
(4) Mass flow meter	Maker : SUNX Model code : FM-216-AR2 Rated flow rate : 1000 L/min Serial No. : 9408-005, 9406-007 Analog voltage output : DC 1~5 V Power source voltage : DC 12~24 V Rated pressure range : −0.09~0.7 MPa Maximum usable pressure : 1.0 MPa
(5) Digital manometer	Model number : 30-1 5MP-A Measurement range : 0 ~ 1.5MPa (abs.) Analog voltage output : DC 0~1.5V Power source voltage : AC 100V±10%
(6) A/D converter	Maker : SUN HAYATO Co. Sampling speed : 1kHz Channel number : 16
(7) Personal computer	Maker : mouse computer Model number : 0812LM-i442S3-PL22W OS : Windows XP
(8) Bread board	Maker : SUN HAYATO Co.

(9) Positive pressure sensor	Maker : Panasonic (SUNX) Model number : DPH-102-M5 (-R) Measurement range : 0 ~ 1.0 MPa,gage Analog voltage output : DC 1~5V Power source voltage : DC 12~15V
(10) Negative pressure sensor	Maker : Panasonic (SUNX) Model number : DPH-103-M5 (-R) Measurement range : 0~ −101kPa,gage Analog voltage output : DC 1~5V Power source voltage : DC 12~15V
(11) Thermocouple	Type 1 Maker : CHINO Type : K Outer diameter : 1 mm Model number : KT98B 7256F Measurement range : −200~630°C Type 2 Maker : YAMARI Type : T Outer diameter : 0.5 mm Model number : 355920 Measurement range : −40~125°C Type 3 Maker : OKAZAKI Type : K Outer diameter : 0.1 mm Model number : GB69962 Measurement range : −270~1372°C
(12) Temperature digital indicator	Maker : CHINO Model number : D1094X004 Voltage resolution : 0.8μV (−200～500℃)

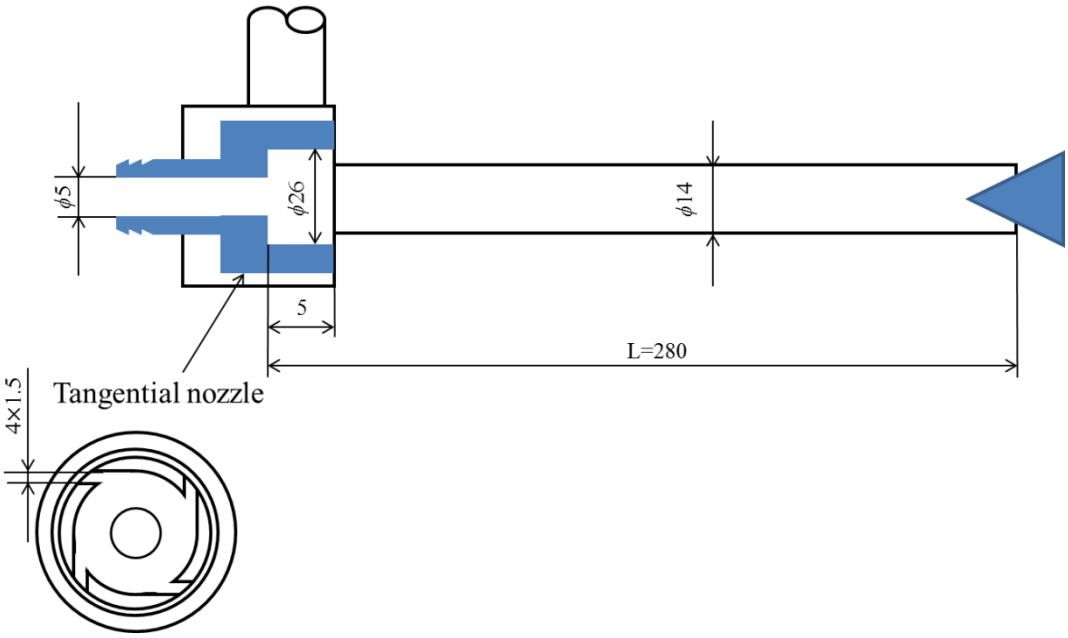

Fig. 2.2 Dimension of vortex tube

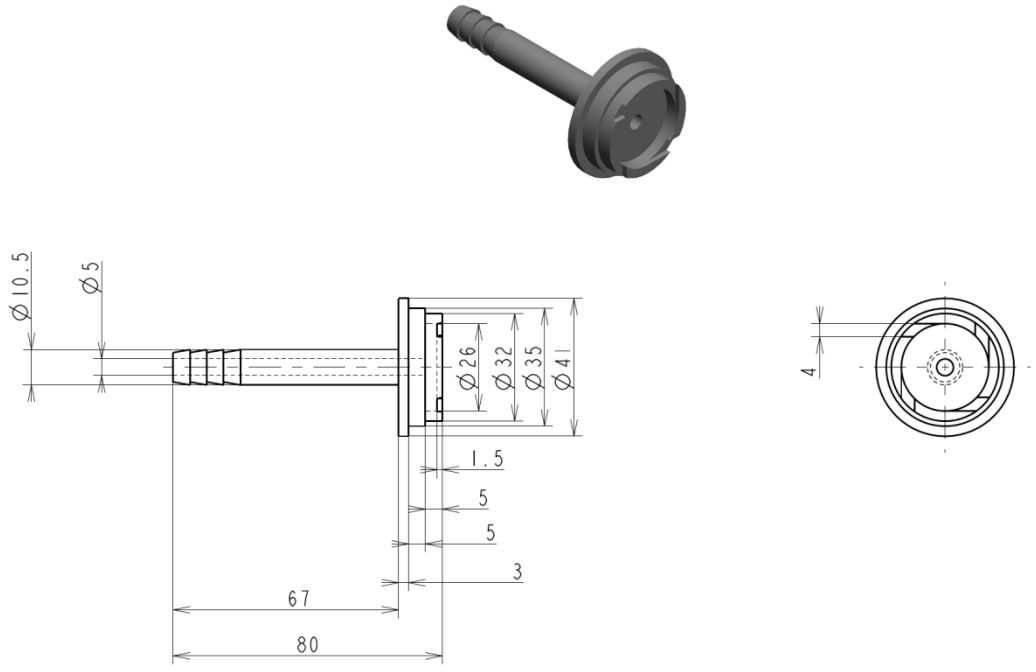

Fig. 2.3 Tangential nozzle with cold exit pipe

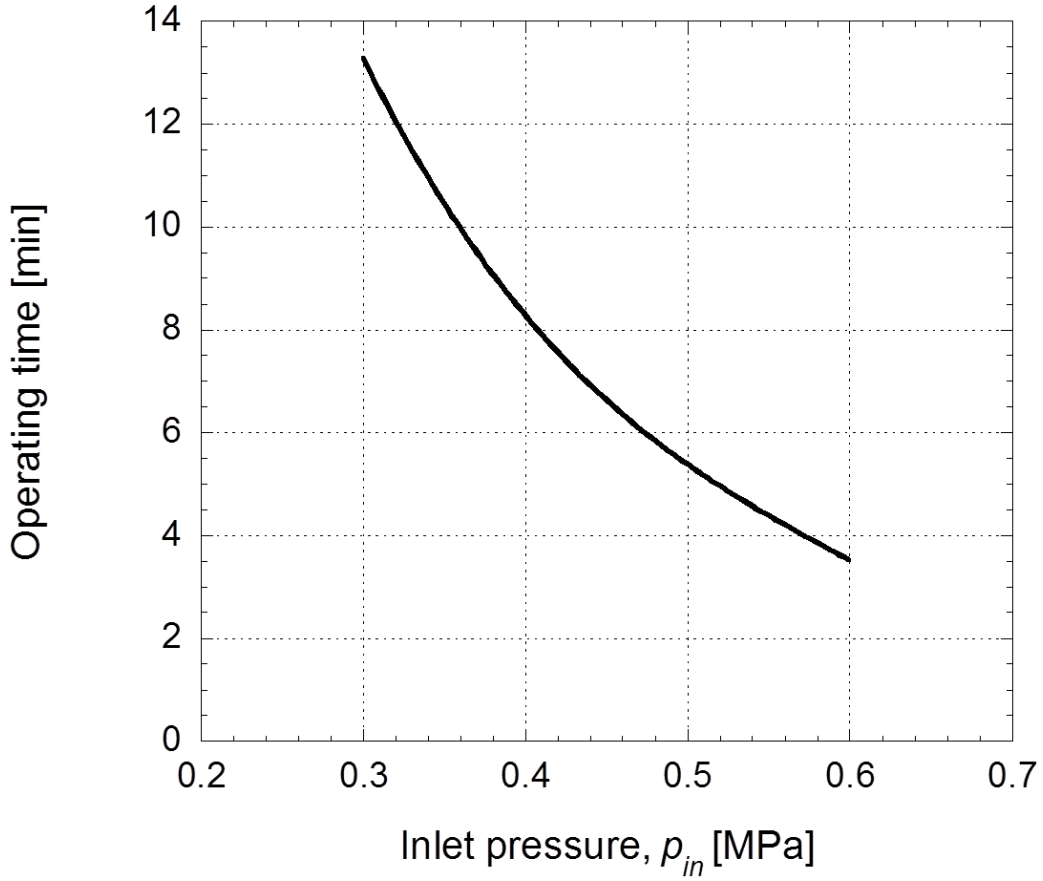

Fig. 2.4 Operating time at each inlet pressure

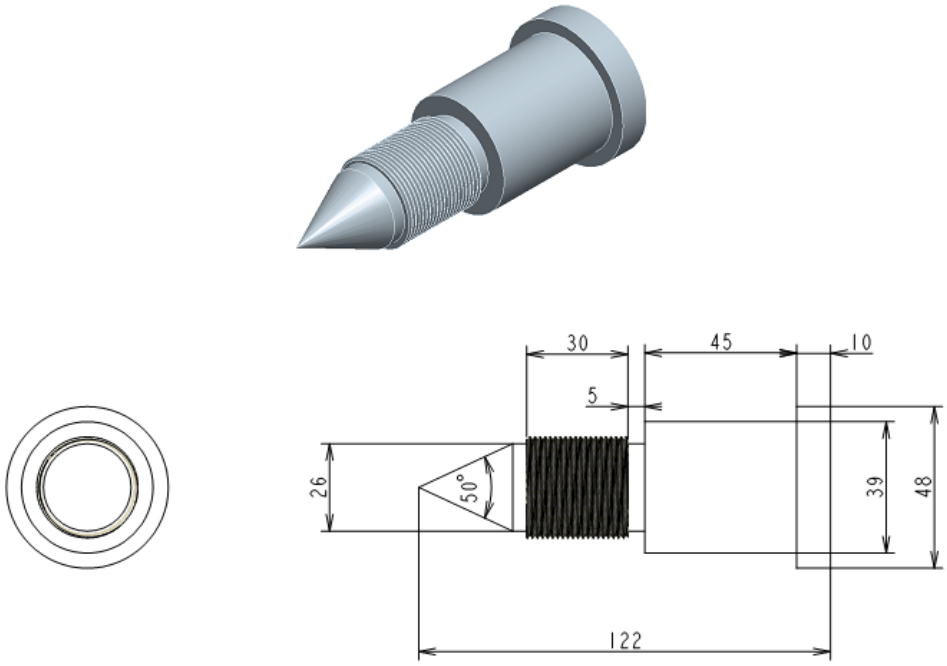

Fig. 2.5 Control valve

2.2 Total temperature probe and Pitot pressure probe

In this research, I am focusing on measuring total temperature and Pitot pressure of the cold flow. This is because energy separation in the VT is expected to occur mainly in a vortical flow in a vortex chamber. Therefore, the flow structure and temperature distribution in the cold flow, which is close to the vortex chamber, is expected to be closely related to that of the vortical flow in the vortex chamber. Accordingly, the flow stucture of the cold flow is expected to provide us with some insights about the ESM in the VT. In the literatures published in the past, the temperature measurements of the cold flow are conducted, but the obtained measurement data cannot be judged whether it is total temperature or static temperature. Regardless to say, the measurement of a static temperature is difficult. Additionally, the total temperature is much more important than the static temperature on the cold flow characteristic of VT, from the view point of thermal performance.

In this research, therefore, the measurement of the total temperature of the cold flow is conducted. To measure a total temperature of a flow with a total temperature probe as accurate as possible, the flow velocity around the measuring point should be low enough. In this research, 3 total temperature probes, which are expected to be able to measure total temperature, are created. An experiment is conducted to measure the measurement error of the created total temperature probes and the details will be explained in detail in Chapter 3.

A Pitot pressure probe is also created to measure the Pitot pressure of the cold flow. Figure 2.6 shows the dimension. This probe measures only stagnation pressure, not static pressure. It has inner/outer diameter of 0.13/0.31mm at the tip, respectively. The tip length is 25mm.

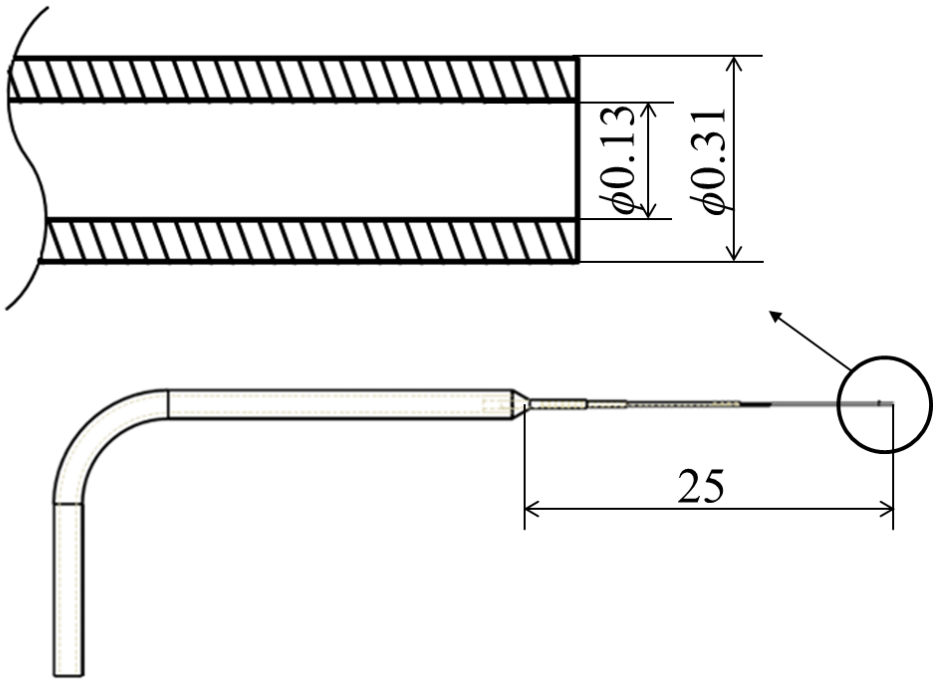

Fig. 2.6 Pitot pressure probe

2.3 Flow visualization technique

In order to understand the flow pattern of the cold flow from the cold exit, flow direction along the center line was visualized. This is because a negative gauge pressure is measured at the cold exit, implying the possibility of a reversed flow, which will be explained later in Chapter 4. The flow visualizations are conducted to verify this possibility.

In this study, two simple flow visualization techniques were created. The first technique uses an oil paint droplet, on a 0.75mm-diameter needle. The Figure 2.7 shows the experimental setup for observation of reversed flow at cold exit using needle and oily paint. The needle, on which the oil paint droplet is put, is held by a XZ traverser, placed left side in the figure. The position of the needle is adjustable by the traverser. The oil paint droplet on the needle is positioned along the centerline of the cold flow.

The close-up image of the needle and the cold exit is shown in Fig. 2.8. As shown in this figure, a small drop of oil paint is put on a needle which is then inserted into the cold flow along the centerline. The distance of the oil paint droplet center, from the cold exit, is fixed at $x \sim 3$mm. The movement of the oil paint represents the direction of the flow along the needle.

Another visualization technique uses a 0.70mm-diameter needle with 10 small holes which can exudate colored oil (exudation needle). Figure 2.9 schematically shows its layout. The exudation needle is inserted into the cold flow along the centerline. Then the colored oil is supplied to the exudation needle from a syringe and the oil exudates from the small holes. The position of the exudation needle is controlled by a traverser, which is the same traverser as was seen in Fig. 2.7. The flow direction of the colored oil on the exudation needle represents the flow direction of the cold flow. The movement of the colored oil, which exudate the needle, is recorded by a high-speed camera, which was supplied by NAC Image Technology.

Figure 2.10 shows the dimension of the exudation needle. This needle has an outer diameter of 0.7mm and 10 holes with 0.3mm diameter. The distance between each hole is 1mm and the distance from the tip of the needle to the first hole is 6mm.

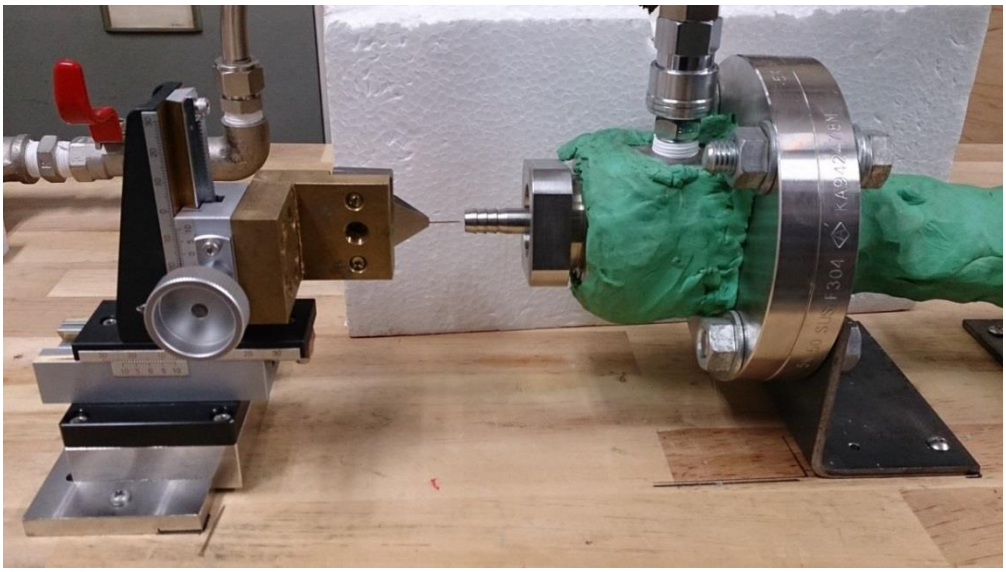

Fig. 2.7 Experimental setup for observation of reversed flow at cold exit using needle and oil paint droplet

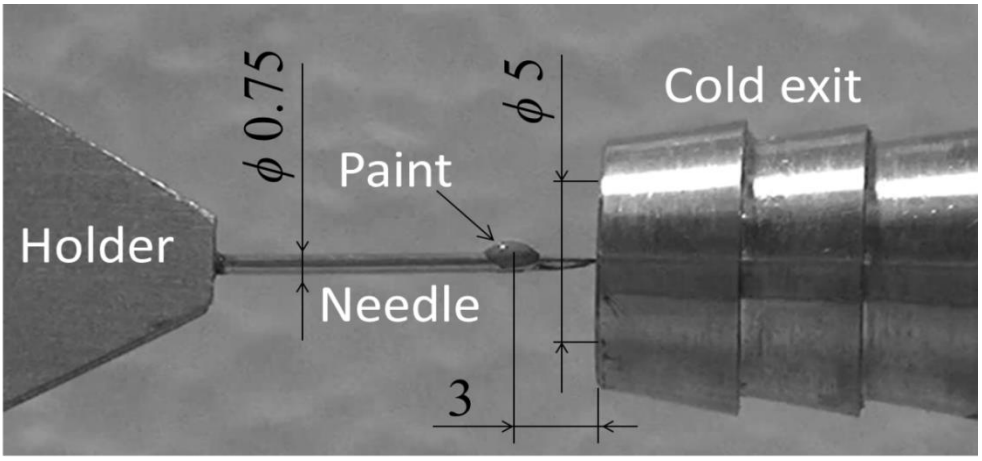

Fig. 2.8 Visualization setup for cold flow direction using needle and oil paint droplet

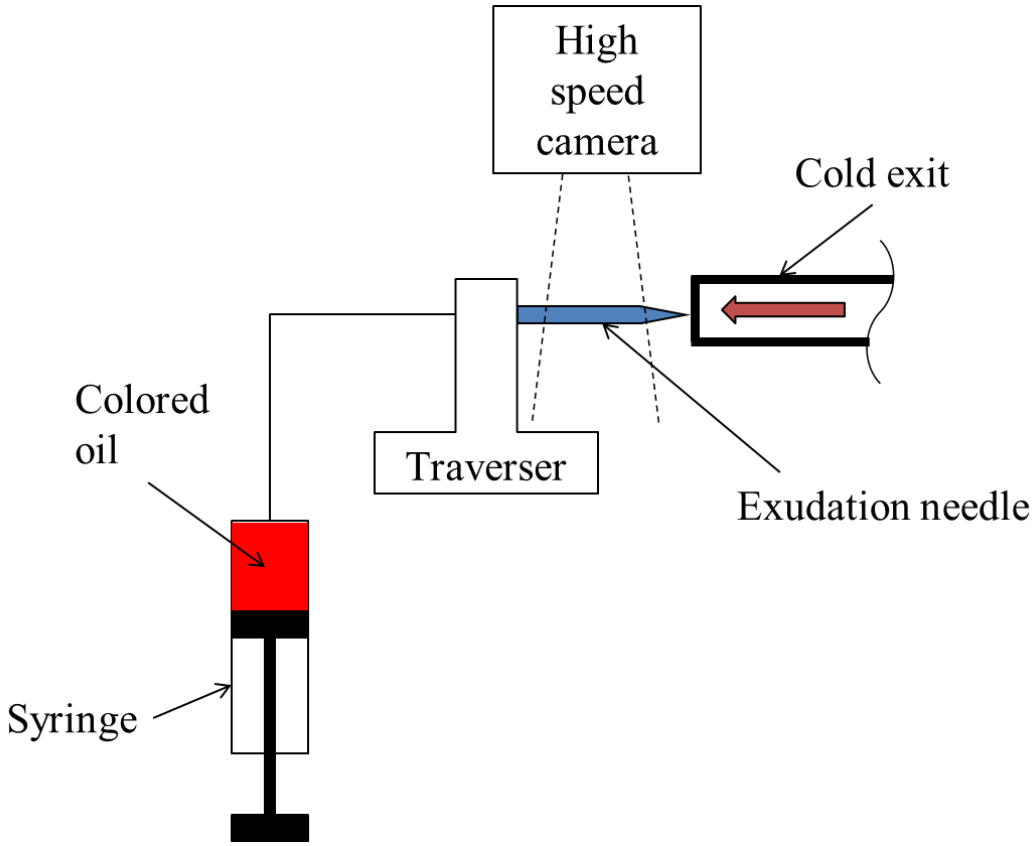

Fig. 2.9 Experimental setup for observation of reversed flow at cold exit using exudation needle

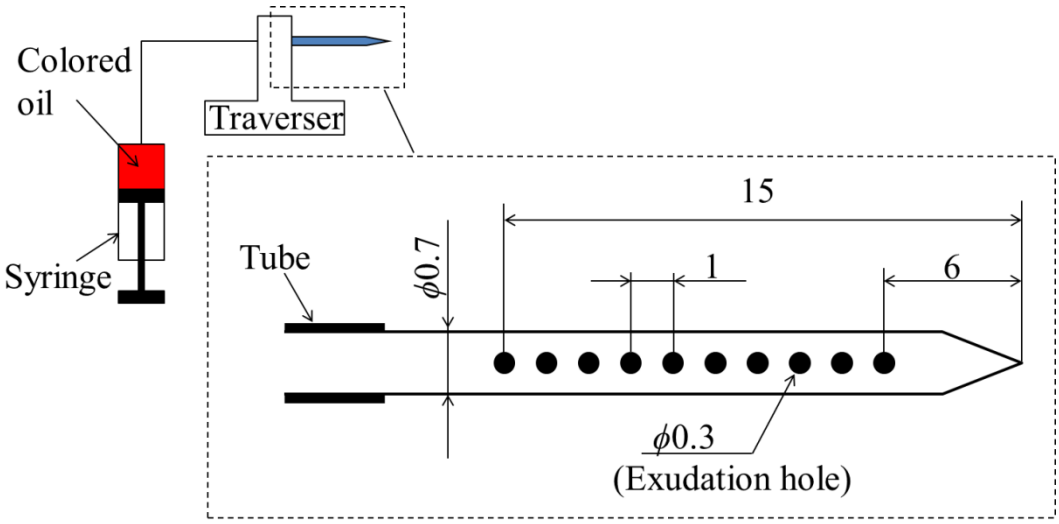

Fig. 2.10 Dimension of exudation needle (unit : mm)

3. Development of Total Temperature Probe

In this chapter, the development of originally designed total temperature probe, to measure the vortical cold flow of VT, and its development history is explained.

3.1 Objective

In this research, I am focusing on measuring total temperature and Pitot pressure of the cold flow. This is because energy separation in the VT is expected to occur mainly in a vortical flow in a vortex chamber. Therefore, the flow structure and temperature distribution in the cold flow, which is close to the vortex chamber, is expected to be closely related to that of the vortical flow in the vortex chamber. Therefore, the information of vortical cold flow from the cold exit is expected to provide insights about the ESM in the VT. In the literatures published in the past, the temperature measurement of the cold flow has been conducted, but the obtained measurement data cannot be clearly judged whether it is total temperature or static temperature. The measurement of a static temperature is difficult because insertion of a probe into a flow unacceptably changes the static temperature at the measurement point. On the other hand, a total temperature at cold/hot exits are much more important than a static temperature in order to evaluate the thermal performance of VT. Therefore, I focus on measuring the total temperature in this research.

When measuring the total temperature of a flow, we need to remember the relation between static temperature and total temperature in a flow;

$$T_s = T_t / \left[1 + \frac{\gamma-1}{2} M^2\right] \tag{2.1}$$

where T_s, T_t, γ, and M is the static temperature, the total temperature, the specific heat ratio and the Mach number, respectively. From Eq.(2.1), it is clearly understood that static temperature decreases as the Mach number increases. In order to measure the total temperature as precisely as possible, the flow must be decelerated enough at the temperature measurement point of the probe.

Figure 3.1 shows an example of conventional total temperature probe[34] used in a high-enthalpy flow. As can be seen in the figure, a thermocouple is inserted in a shield. There are vent holes to discharge the flow and introduce the fresh gas into

the probe. The flow inside the probe should be decelerated as much as possible, to sufficiently recover the kinetic energy of the gas flow as a dynamic temperature. It should be noted that the flow inside the tube must not be in a stagnation state, which will lower the measured temperature by thermocouple than actual total temperature of the gas because the tip of the thermocouple is expected to suffer from inner wall temperature of shield pipe by heat conduction in a hot flow. Therefore, the vent hole is supposed to be as small as possible to sufficiently decelerate the flow in the probe. Figure 3.2 shows the experimentally obtained relation between the vent hole to entrance area ratio and measured total temperature in Ref.[34]. From this figure, it is understood that the vent hole area should be less than 25% (1/4) of the entrance area of the probe. It should be noted that this total temperature probe can only be use if the direction of the flow is known. The flow discharged from the cold exit of the VT is a vortical flow. Therefore, a total temperature probe which can measure a total temperature in a vortical flow is needed.

In this research, 3 types of total temperature probe are created. An evaluation experiment is conducted to determine the measurement error of the probes. A vortical flow is suitable to validate the probes, however, total temperature in a vortical flow is unknown, and therefore, it cannot be used for the evaluation test. Therefore, in this research, a subsonic flow discharged from a sonic nozzle in different angles is used. The details of the procedure and results will be explained in the next 2 sections.

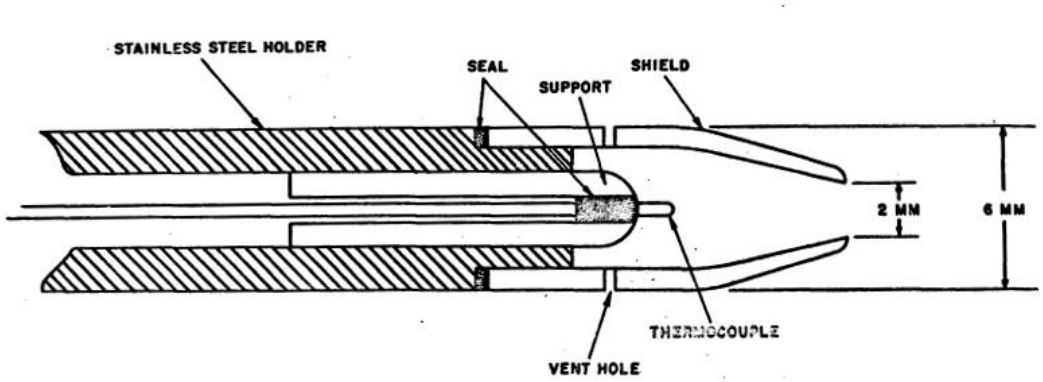

Fig. 3.1 Example of conventional total-temperature probe used in a high-enthalpy flow[34]

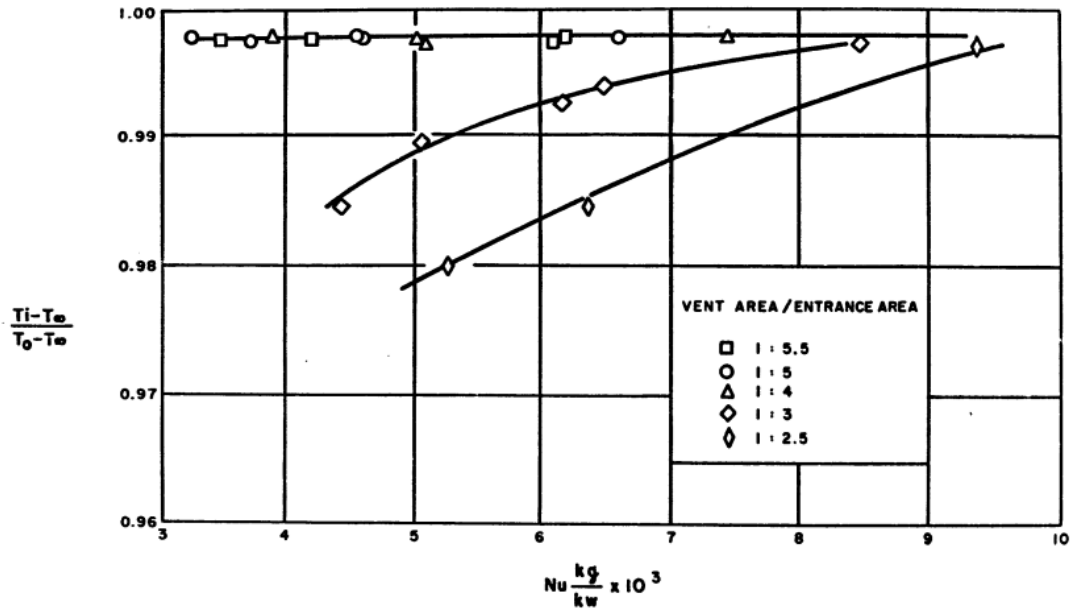

Fig. 3.2 Variation of total temperature probe performance with vent to entrance area ratio[34]

3.2 Structure of probe and evaluation test

In this research, 3 total-temperature probes are created. The first created total temperature probe is shown in Fig. 3.3. It is named as Type 1. The probe is made by inserting a K-type ϕ1 thermocouple, into an acrylic pipe, which has inner/outer diameter of 1.2/5.0mm and length of 27.0mm. Approximately, 1mm of the tip of the thermocouple is protruding from the rod, to create a stagnation state when inserted in flow. According to research works conducted in the past, it is found that most researchers use a T-type thermocouple to measure the temperature of the cold flow. Therefore, a similar total temperature probe as the Type 1 using a T-type thermocouple, which is named Type 2, was created.

Figure 3.4 shows the Type 2 probe. It is made by inserting a T-type ϕ0.5 thermocouple, into an acrylic pipe, which has inner/outer diameter of 0.6/3.0mm and length of 21.5mm. Approximately, 0.5mm of the tip of the thermocouple is protruding from the rod, to create a stagnation state when inserted in flow. Note that the diameter of the T-type thermocouple is smaller than the K-type thermocouple. This is because a smaller diameter probe is preferable considering the cold exit diameter of 5mm.

After performing experiments with these two probes, it was found that the flow at the tip of the thermocouple is not decelerating enough to measure a total temperature, as will be explained later in this chapter. Therefore, a sponge is used to cover the tip of the Type 2, which is named as Type 3. Figure 3.5 shows the Type 3 probe. It is expected that a sponge can be used to decelerate the flow around the tip of the thermocouple. The summary of the dimensions of the Type 1, 2, and 3 probes are shown in Table 3.1

A vortical cold flow is discharged from the cold exit of VT. To measure a total temperature of the flow, it is important to place a temperature measurement probe along the vector direction of the flow. Or, the probe is required that the measurement value is not sensitive to the setting angle between the probe axis and flow direction (measurement angle). In this research, an evaluation experiment is conducted to determine the relation of measurement angle and measured temperature. In the evaluation experiment, a sonic nozzle with a ϕ10mm exit diameter is used. The sonic nozzle is installed on a stagnation chamber. A compressed gas, which is stored in $2m^3$ tank with pressure of 1MPa as initial

conditions, enters the stagnation chamber by way of pressure regulation valves. The inlet pressure in the stagnation chamber was varied from 0.12 ~ 0.2MPa, which was measured with a digital manometer. The total temperature of the compressed gas was assumed to be atmospheric temperature during the experiment. The created probes were placed in the potential core of the jet flow, which was discharged from the sonic nozzle, along the centerline of the jet flow. The measurement angle of the probe was changed from 0 ~ 90°.

Figure 3.6 shows the measurement angle θ of the created total temperature probe. $\theta = 0°$ represents an angle when the total temperature probe is horizontal with the centerline of the sonic nozzle. $\theta = 90°$ represents an angle when the total temperature probe is perpendicular to the centerline of the sonic nozzle. The measurement results will be explained later in the next section.

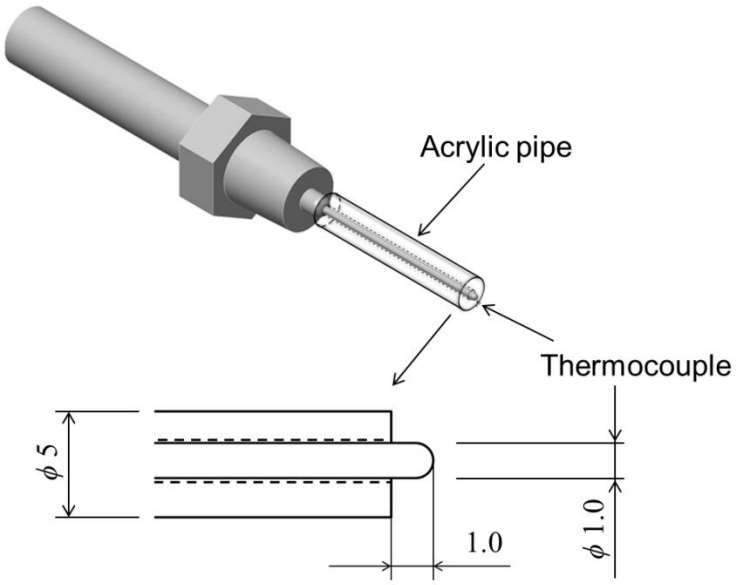

Fig. 3.3 Type 1 total temperature probe without sponge (K-Type thermocouple)

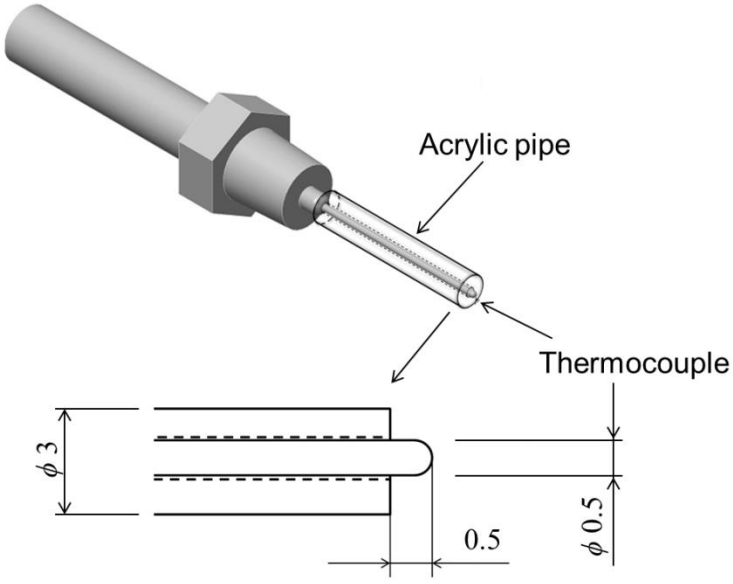

Fig. 3.4 Type 2 total temperature probe without sponge (T-Type thermocouple)

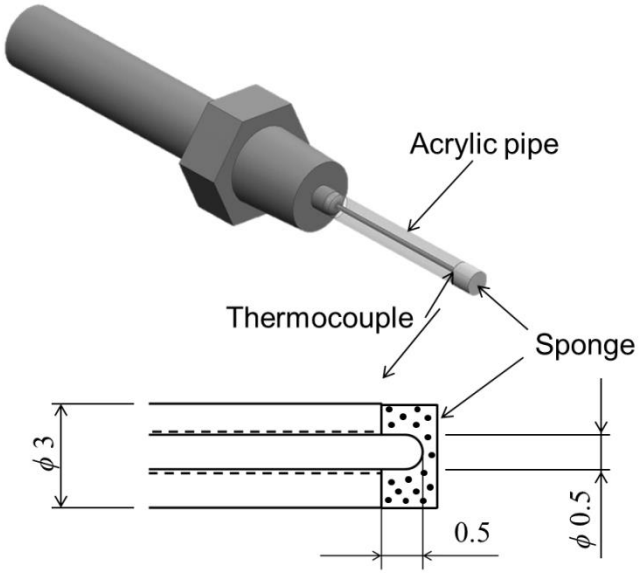

Fig. 3.5 Type 3 total temperature probe with sponge (T-Type thermocouple)

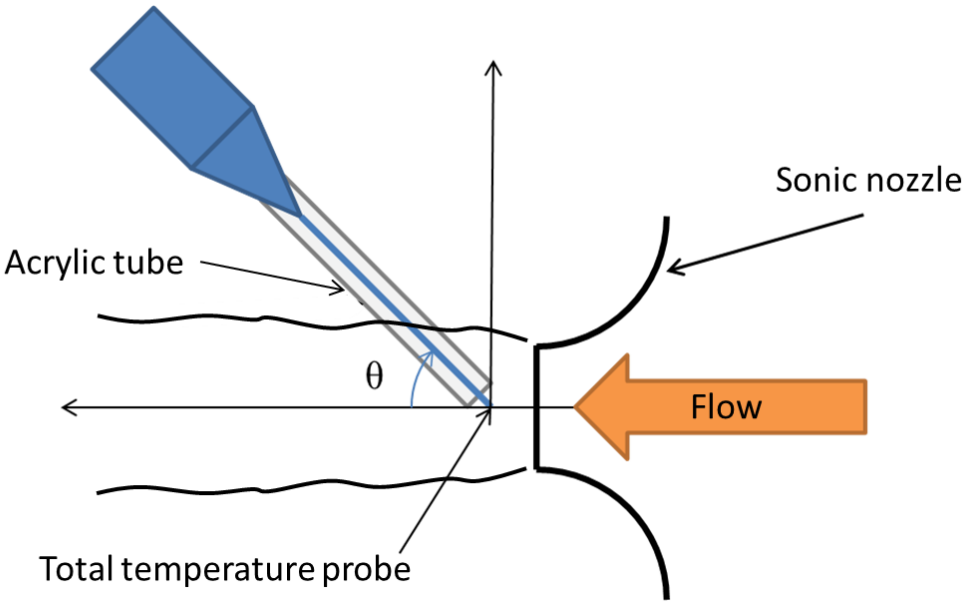

Fig. 3.6 Angle of total temperature probe

Table 3.1 Dimensions of the created total temperature probes

Probe Type	1	2	3
Thermocouple type	K	T	T
Sheath diameter	1mm	0.5mm	0.5mm
Sheath length	27mm	21.5mm	21.5mm
Outer diameter of acrylic pipe	5mm	3mm	3mm
Inner diameter of acrylic pipe	1.2mm	0.6mm	0.6mm
Sponge at the tip	No	No	Yes
Protrude length of thermocouple	1mm	0.5mm	0.5mm

3.3 Results and discussion

An evaluation experiment was performed to obtain the temperature measurement error of each created probes. In this experiment, the inlet pressure of the stagnation chamber was varied from 0.12 to 0.20MPa. The measurement angle of those probes, as shown in Fig. 3.6, was varied from 0° to 90°, where 0° means the probe to be horizontal with the centerline of the sonic nozzle, and 90° means the probe to be perpendicular to the center line of the sonic nozzle. The total temperature of the gas inside the chamber, which is the inlet temperature, is assumed to be equal to atmospheric temperature, which is measured by a thermocouple. Atmospheric temperature was measured before and after the experiment. The averaged value of the measured temperature was used as the total temperature inside chamber.

The results of temperature measurement of Type 1, 2 and 3 are shown in Fig. 3.7 (a), (b), and (c), respectively. The vertical axis of those figures show the measured temperature divided with the inlet temperature, T_e/T_{in}, and the horizontal axis shows the measurement angle of probe, θ. From these results, the largest measurement errors of Type 1, 2 and 3 are −1.3°C, −1.1°C, and −0.7°C, respectively. From these figures, it is clear that the Type 3 probe, which has a sponge covering the tip of the thermocouple, has the smallest measurement error. The effect of the measurement angle of the thermocouple on the total temperature measurement is negligibly small for the Type 3 probe. Therefore, the Type 3 is chosen to measure the total temperature of cold flow.

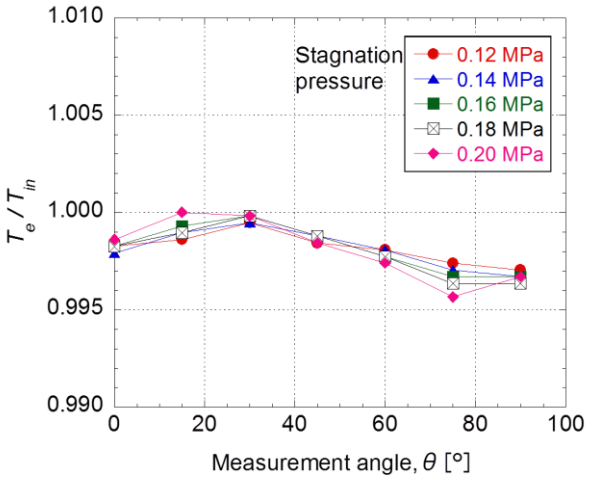

(a) Type 1

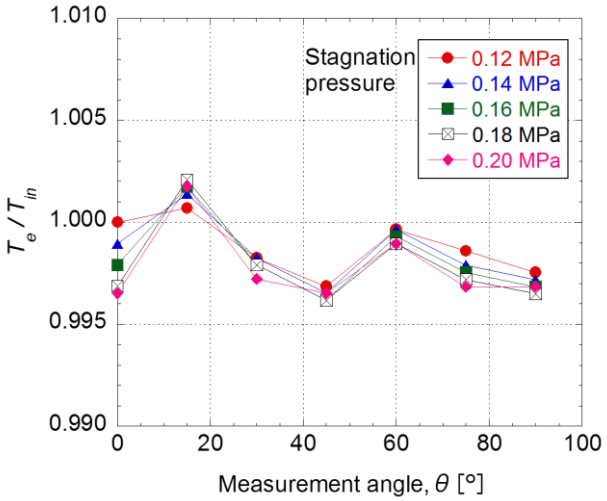

(b) Type 2

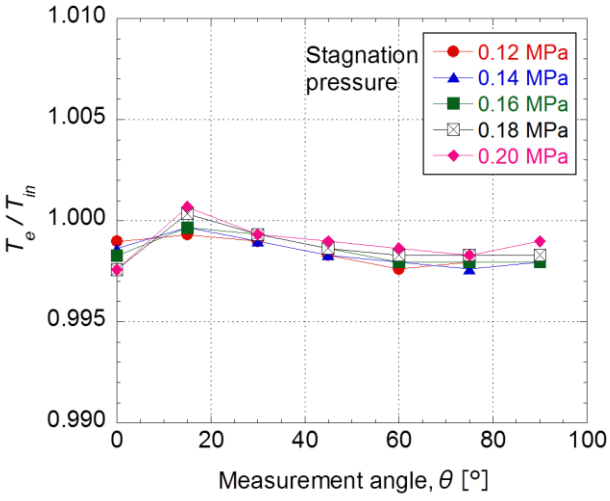

(c) Type 3

Fig. 3.7 Measured temperature at sonic nozzle exit at different angle

3.4 Conclusions

To measure the total temperature at the cold exit, 3 different probes were created. Those probes were named as Type 1, Type 2 and Type 3, respectively. Each of them was created by inserting a thermocouple into an acrylic tube with the tip of the tube is protruding from the rod. The tip of the Type 3 was covered with sponge to decelerate the flow at the tip of the thermocouple. An evaluation experiment was conducted in a subsonic air jet flow, whose stagnation temperature to be atmospheric temperature, from a converging nozzle to determine the relationship between the measurement angle and measured temperature. During the experiment, the measurement angle setting was varied from 0 ~ 90° to see whether the probe is usable in a vortical flow.

It was found from the experimental results that, the largest measurement errors of Type 1, 2 and 3 are −1.3°C, −1.1°C, and −0.7°C, respectively. From those 3 probes, it is found that the Type 3 probe, which has a sponge at the tip of the thermocouple, has the smallest measurement error. The effect of the measurement angle on the measured total temperature is negligibly small.

4. Flow Measurement at Cold Exit

In this chapter, the experimental results measured by the created total temperature probes and Pitot pressure probe at the cold exit is presented and discussed. In addition, a simple flow visualization method was used to observe the reversed flow at the cold exit, and the mixing temperature of cold and hot flows is measured to determine the cooling capacity and heat loss of VT.

4.1 Experimental procedure

4.1.1 Cold fraction setting

The performance of the VT can be controlled by adjusting the cold fraction, which is a ratio of cold flow mass flow rate to inlet mass flow rate. The cold fraction can be controlled by the control valve installed at the hot exit of the tube (see Fig. 2.2). By turning the control valve, the cross-sectional area of the hot exit is adjusted. So, when this cross-sectional area increases, the mass flow rate of the hot flow increases. Simultaneously, the mass flow rate of the cold flow decreases. It should be noted that even if the setting of the control valve is unchanged, the cold fraction is different depending on the setting of inlet pressure. In this subsection, how to adjust the control valve at arbitrary inlet pressure for 0.2 ~ 0.6MPa and cold fraction for $0.1 < \varepsilon < 1.0$ is explained.

In this experiment, I measured two mass flow rate readings; inlet and hot flow. Since the inlet mass flow rate is equal to the total mass flow rate of cold and hot flows ($\dot{m}_{in} = \dot{m}_{cold} + \dot{m}_{hot}$), the cold fraction can be calculated as below;

$$\varepsilon = \frac{\dot{m}_{cold}}{\dot{m}_{in}} = 1 - \frac{\dot{m}_{hot}}{\dot{m}_{in}} \tag{4.1}$$

When measuring the cold fraction, the valve is turned anticlockwise to open the gap between the conical part of the control valve and inner tube. Then, the compressed gas is supplied into the VT at desired inlet pressure. Equation (4.1) is used to calculate the cold fraction from the measured mass flow rate. When the cold fraction is higher than the target value, the valve is turned anticlockwise again to enlarge the gap between the conical part of the control valve and inner tube. When the cold fraction is lower than the target value, the valve is turned clockwise. This procedure is repeated at every inlet pressure.

4.1.2 Pressure measurement

The pressure at the cold exit was measured with a Pitot pressure probe. For pressure measurement, the Pitot pressure probe was inserted into the cold flow along the centerline of the cold exit, at a distance of 3mm (x = 3mm) from the exit, as shown in Fig. 4.1. The inlet pressure is varied from 0.2 to 0.6MPa. The cold fraction is varied from 0.1 to 1.0.

4.1.3 Flow visualization

In this experiment, two flow visualization techniques were created. The first technique uses an oil paint droplet, on a 0.75mm-diameter needle. The oil paint droplet on the needle was positioned along the centerline of the cold flow at x = 3mm, as shown in Fig. 4.2. The movement of the oil paint droplet represents the flow direction of the cold flow.

Another flow visualization technique uses a 0.70mm-diameter needle (SUS tube) with 10 small holes which can exudate colored oil (exudation needle). The exudation needle was inserted into the cold flow along the centerline and moved along x direction by a traverser, as shown in Fig. 4.3. Then, the colored oil was supplied to the exudation needle little by little and exuded from the small holes. The exudation needle was moved along the centerline to determine the length of reversed flow. The movement of the colored oil, which exudate the needle, was recorded by a high speed camera to observe the length of the reversed flow which occurs at the cold exit. In all the flow visualization experiments, the inlet pressure of the VT was set at 0.4MPa. The cold fraction was varied from 0.15 to 0.46.

4.1.4 Temperature measurement

The total temperature probe of Type 1, 2, and 3 were used to measure the total temperature difference of cold flow, $\Delta T_{t,cold}$ at p_{in} = 0.4MPa. Cold fraction was varied from 0.1 to 0.9. The type 3 was used to measure the total temperature of the cold flow at cold exit. The type 3 probe was inserted into the cold flow along the centerline of the cold exit at x = 3mm, as shown in Fig. 4.4. The inlet pressure was varied from 0.2 to 0.6MPa. The cold fraction was varied from 0.1 to 1.0.

To evaluate the performance of VT, mixing temperature of cold and hot flows were measured. Due to the existence of radial temperature distribution at cold exit, a mixing chamber is installed at the cold exit as shown in Fig. 4.5 to measure the

mixing temperature. As is indicated in this figure, an acrylic pipe, which was inserted into a PVC pipe, was attached to the cold exit through an adiabatic tube. It should be noted that the inner diameter of acrylic pipe is equal to the diameter of cold exit (d_c = 5mm). A copper mesh wire was installed at the exit end of the PVC pipe. This copper mesh was used to enhance mixing of the cold flow, which was discharged from the acrylic pipe. An evaluation experiment was conducted to assure that the cold flow is properly mixed, by measuring 10 different radial points at the end of the PVC pipe during the experiments. The result shows that negligible temperature distribution, less than 0.4°C, exists at the end of the PVC pipe.

Another evaluation experiment was also conducted to determine the effect of the mesh on the cold flow by installing and uninstalling the mesh. If the mesh disturbs the cold flow, more flow will go to the hot exit. Therefore, the cold fraction was checked for the "mesh installed condition" and "without mesh condition" under the same setting of control valve. The result shows that the difference of the cold fraction when the mesh is installed was less than 4.2%. Therefore, the effect of the mesh on the flow condition is negligible. The mixing temperature of the hot flow was measured at the exit nozzle of a stagnation chamber located after the mass flow meter. The experimental conditions of inlet pressure and cold fraction are same as that for measuring center temperature at cold exit (p_{in} = 0.2 ~ 06MPa, ε = 0.1 ~ 0.9).

From the measured mixing temperature of the cold and hot flows, the cooling capacity (refer to Eq.(1.7)) and non-dimensional heat loss from VT to ambient air derived from the total-enthalpy conservation equation are calculated. The non-dimensional heat loss from the VT can be calculated by the following equation;

$$\frac{\Delta q_{loss}}{c_p T_{atm}} = \frac{\varepsilon \Delta \bar{T}_{t,cold}}{T_{atm}} - \frac{(1-\varepsilon)\Delta \bar{T}_{t,hot}}{T_{atm}} \tag{4.2}$$

where Δq_{loss} is the heat loss per unit mass of working gas, c_p is the specific heat, T_{atm} is the ambient temperature of 300K, $\bar{T}_{t,cold}$ is the mixing temperature of cold flow, and $\bar{T}_{t,hot}$ is the mixing temperature of hot flow. Calculated result will be explained later in section 4.2.3.

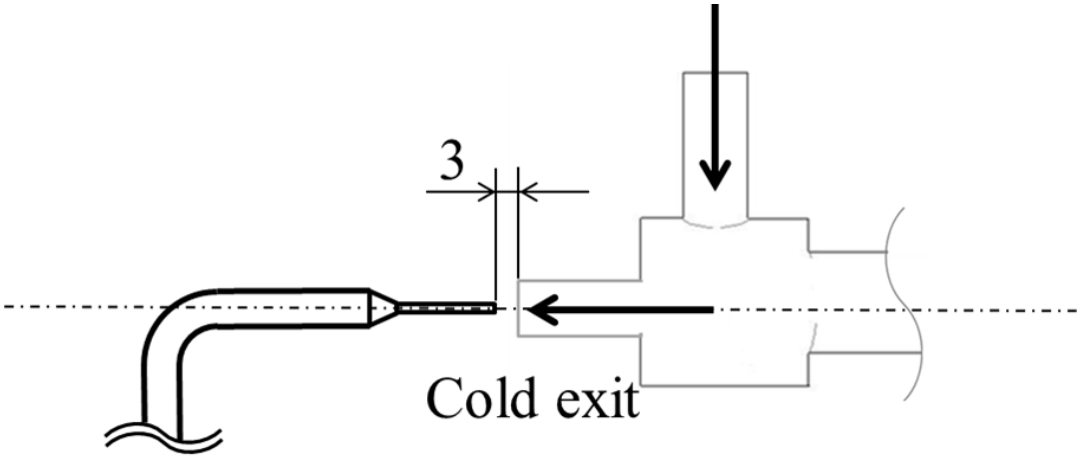

Fig. 4.1 Setup of Pitot pressure probe

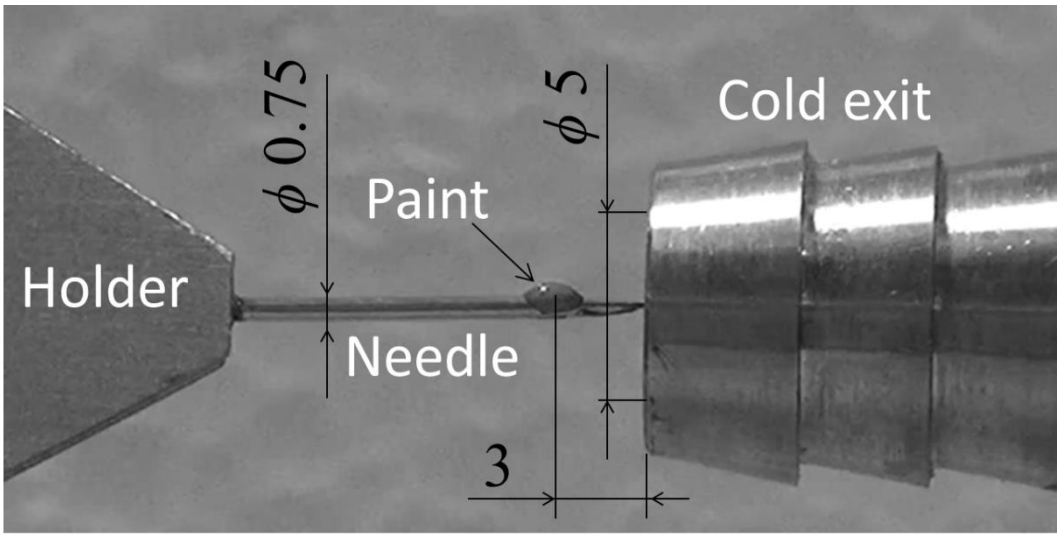

Fig. 4.2 Visualization setup for cold flow direction using needle and oil paint droplet

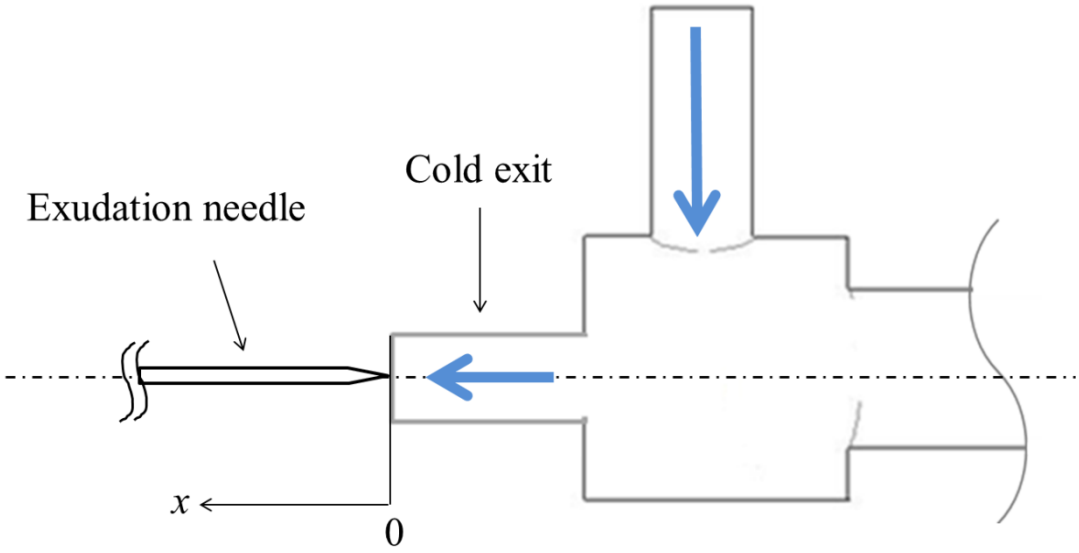

Fig. 4.3 Set up of exudation needle in cold flow

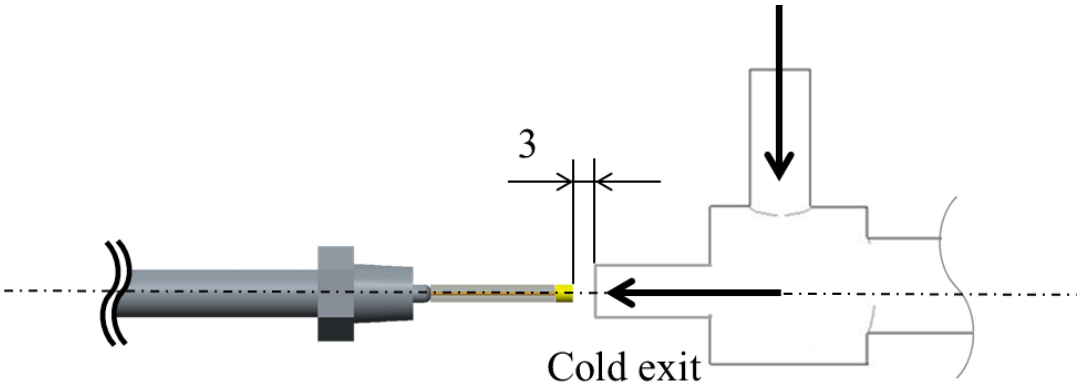

Fig. 4.4 Measurement point of Type 3 total temperature probe

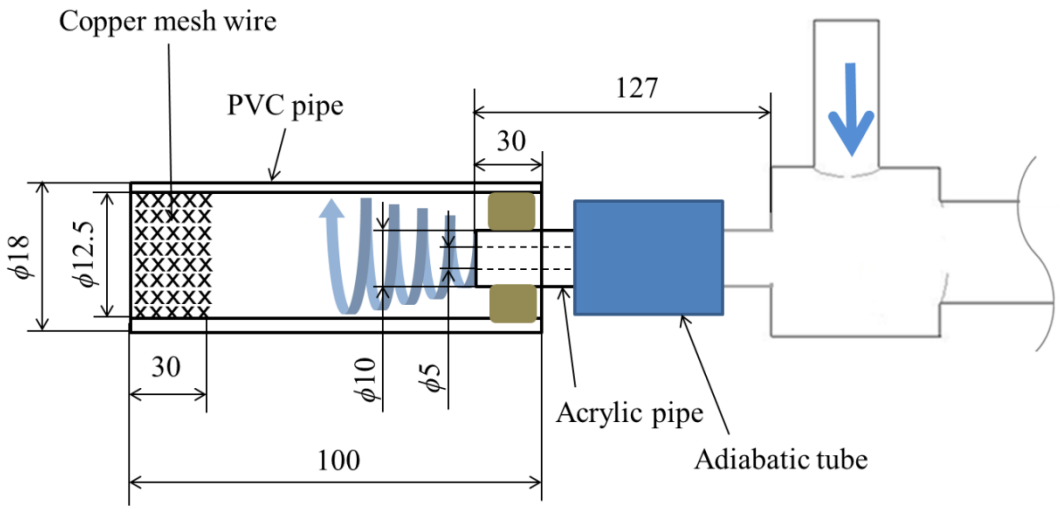

Fig. 4.5 Schematic diagram of the experimental setup for measuring mixing temperature of cold flow

4.2 Results and discussion

4.2.1 Pressure measurement

In order to understand the flow pattern at the cold exit, Pitot pressure of cold flow was measured, by the probe, which was shown in Fig.4.1, at x = 3mm from the cold exit plane, along the centerline. Figure 4.6 shows a contour map of the measured Pitot pressure, divided by atmospheric pressure, p_i / p_a, at x = 3mm. The horizontal axis of the figure shows the inlet pressure, p_{in}, and the vertical axis shows the cold fraction, ε. It can be seen from this figure that at a specific inlet pressure, when the cold fraction decreases from unity, the non-dimensionalized Pitot pressure inverts from $p_i / p_a > 1$ to $p_i / p_a < 1$. The existence of $p_i / p_a < 1$ implies the possible occurrence of a reversed flow around the central part of the cold flow. This reversed flow will be discussed in the next section.

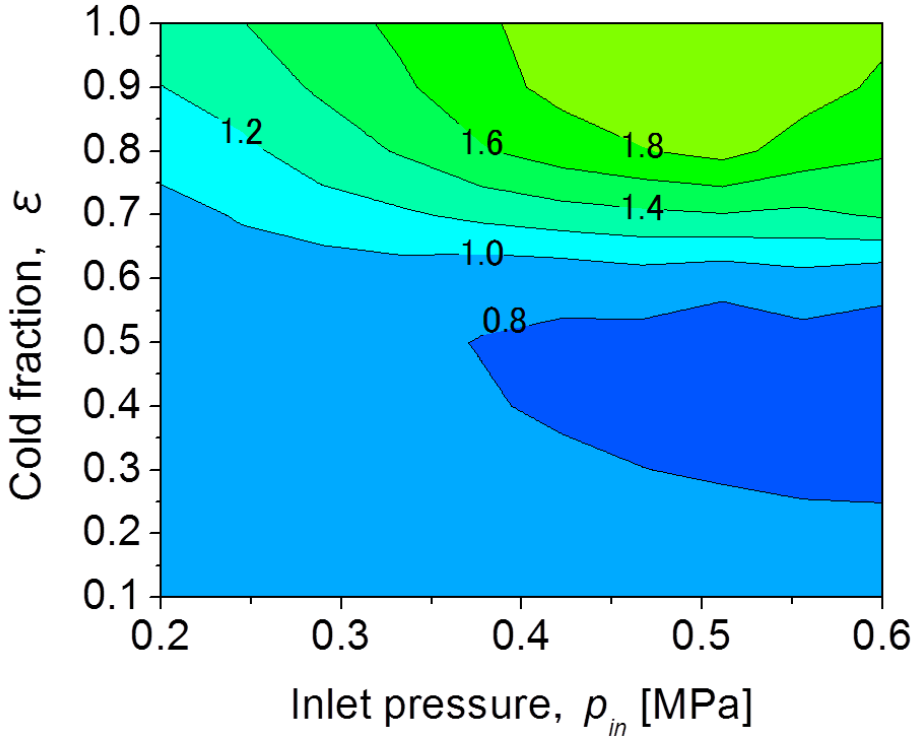

Fig. 4.6 Contour map of non-dimensionalized Pitot pressure p_i/p_a at x = 3mm from cold exit

4.2.2 Flow visualization

Figure 4.7 (a) shows the flow visualization result at p_{in} = 0.2MPa, ε = 0.84. The initial position of the oil droplet is also shown in the figure. It can be seen from the figure that the droplet moves in the downstream direction, showing the direct flow at x = 3mm along the centerline. Figure 4.7 (b) shows the result at p_{in} = 0.2MPa, ε = 0.71. In this figure, it is seen that the droplet remains at initial position, x = 3 mm, indicating a stagnation point, which corresponds to the boundary point of direct/reversed flow. Figure 4.7 (c) shows the result at p_{in} = 0.2MPa, ε = 0.33. It is obvious from the figure that the droplet moves upstream toward the cold exit, indicating the existence of a reversed flow at x = 3mm. From Fig. 4.7, it can then be understood that a reversed flow exists at the cold exit.

Figure 4.8 (a), (b), and (c) show the flow visualization results at p_{in} = 0.5MPa, and ε = 0.58, 0.31, and 0.17, respectively. It can be seen from these figures that a direct flow occurs at ε = 0.58, a reversed flow occurs at ε = 0.17, and the droplet remains at initial position, x = 3mm, at ε = 0.31, indicating a stagnation point, which corresponds to the boundary point of direct/reversed flow. Same visualization experiments were also performed at p_{in} = 0.3, 0.4, 0.6MPa, respectively, at cold exit.

Figure 4.9 shows the contour map of the Pitot pressure at x = 3mm along the centerline, non-dimensioned by atmospheric pressure, the similar figure to Fig. 4.6, with a thick boundary line of direct/reversed flows determined by the flow visualization results explained in Figs. 4.7 and 4.8. It should be noted from Fig. 4.9 that, the reversed flow occurs when the Pitot pressure is lower than atmospheric pressure. In addition, it can also be observed from Fig. 4.9 that, at an arbitrary inlet pressure, when the cold fraction is decreased from 1.0, a direct flow inverts to a reversed flow at a specific value of the cold fraction. This inversion occurs at a smaller value cold fraction with a larger inlet pressure. The generation of the reversed flow at the cold exit of VT has recently been reported by Ameri et al.[35] and Dutta et al.[36] using a numerical simulation without any experimental validation. To the best of my knowledge, the experimental observation of a reversed flow at the cold exit of a counter-flow VT is for the first time discussed in this work [37].

Figure 4.10 (a), (b), (c), and (d) show the flow visualization results using exudation needle at ε = 0.15, 0.24, 0.34, and 0.46, respectively, at p_{in} = 0.4MPa.

The cold exit, not shown in the picture, is located on the right side of the captured area. From these figures, the stagnation point of the cold flow along the centerline is observed at each cold fraction, ε. The distance of the stagnation point from the cold exit, x_s, which represents the length of the reversed flow measured from the cold exit, is plotted in Fig. 4.11. The horizontal axis shows the distance of the stagnation point from the cold exit, x_s, and the vertical axis shows the cold fraction, ε. From this figure, it is clearly understood that x_s increases when the cold fraction decreases. The increase in x_s implies the decrease in the pressure at the core of the vortex chamber when the cold fraction decreases. Therefore, decrease in the cold fraction is thought to lead decrease in the pressure at the core of the vortex chamber.

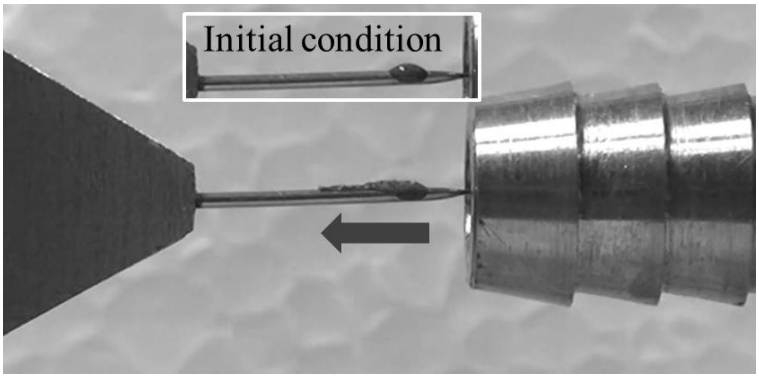

(a) ε = 0.84

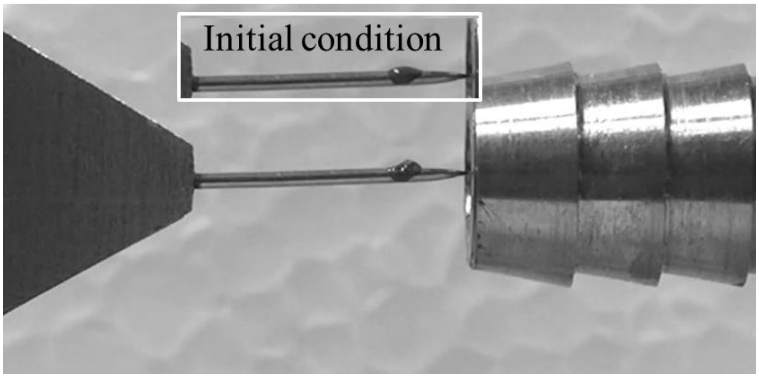

(b) ε = 0.71

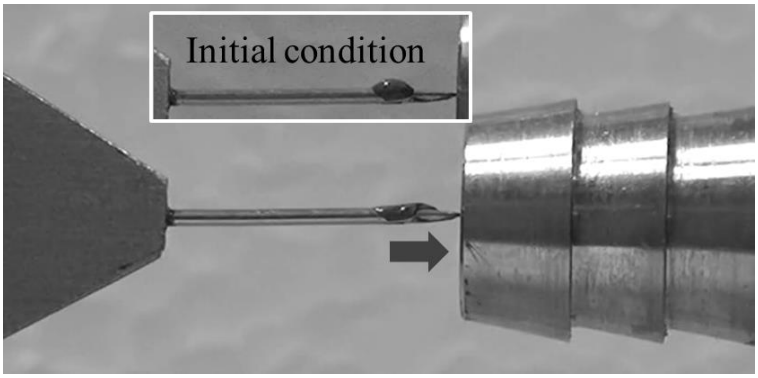

(c) ε = 0.33

Fig. 4.7 Visualization results at p_{in} = 0.2MPa

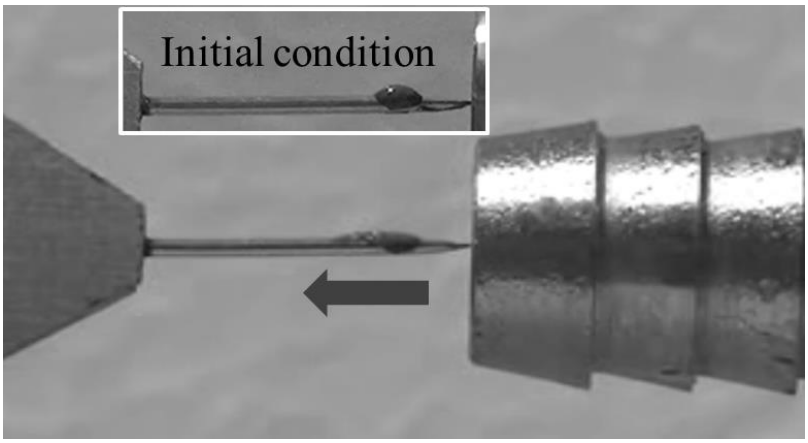

(a) ε = 0.58

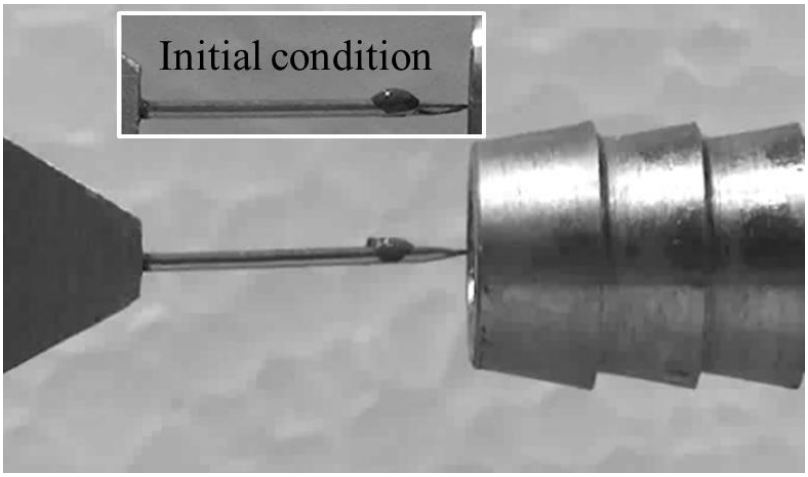

(b) ε = 0.31

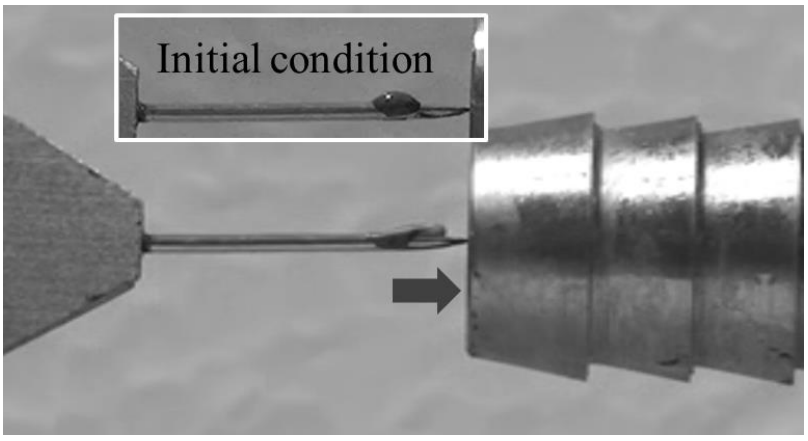

(c) ε = 0.17

Fig. 4.8 Visualization results at p_{in} = 0.5MPa

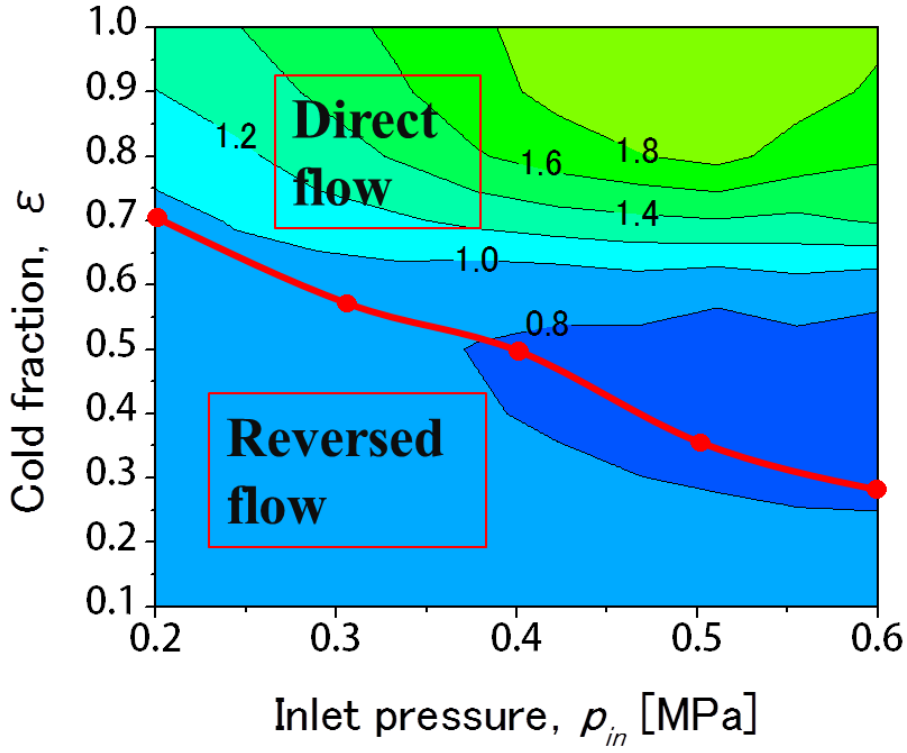

Fig. 4.9 Direct/reversed flow boundary line on contour map of non-dimensionalized Pitot pressure at x = 3mm on centerline

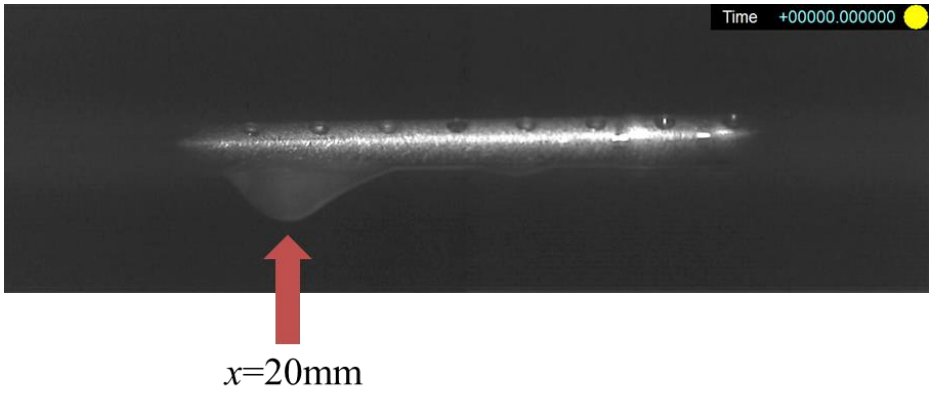

(a) ε = 0.15

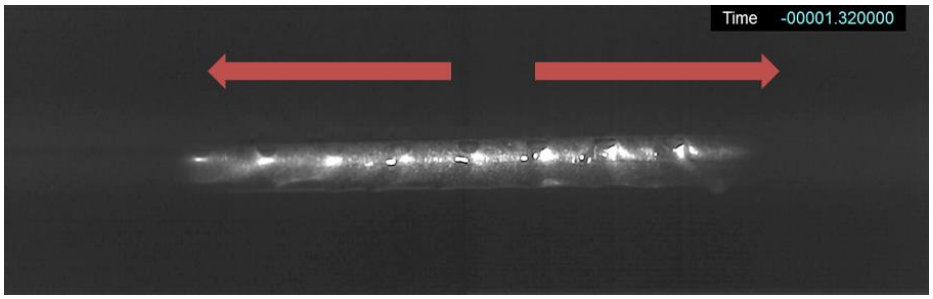

(b) ε = 0.24

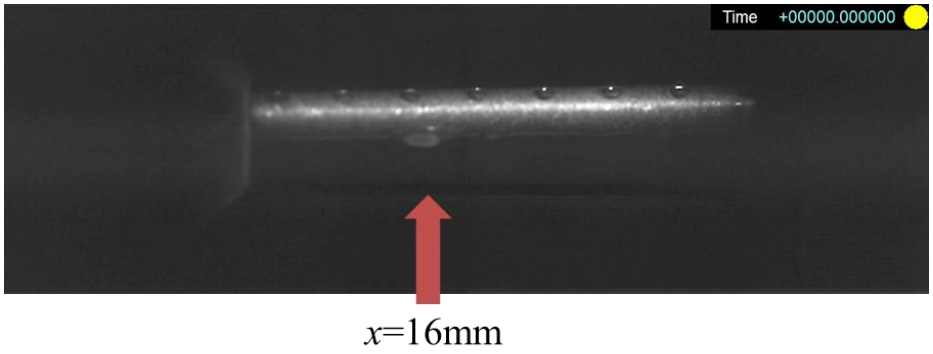

(c) ε = 0.34

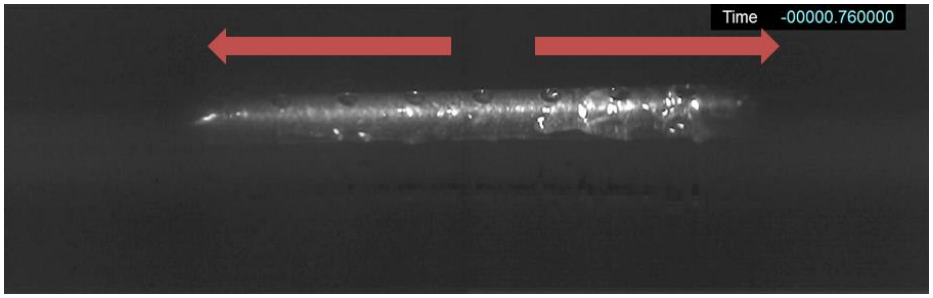

(d) ε = 0.46

Fig. 4.10 Visualization results at p_{in} = 0.4MPa

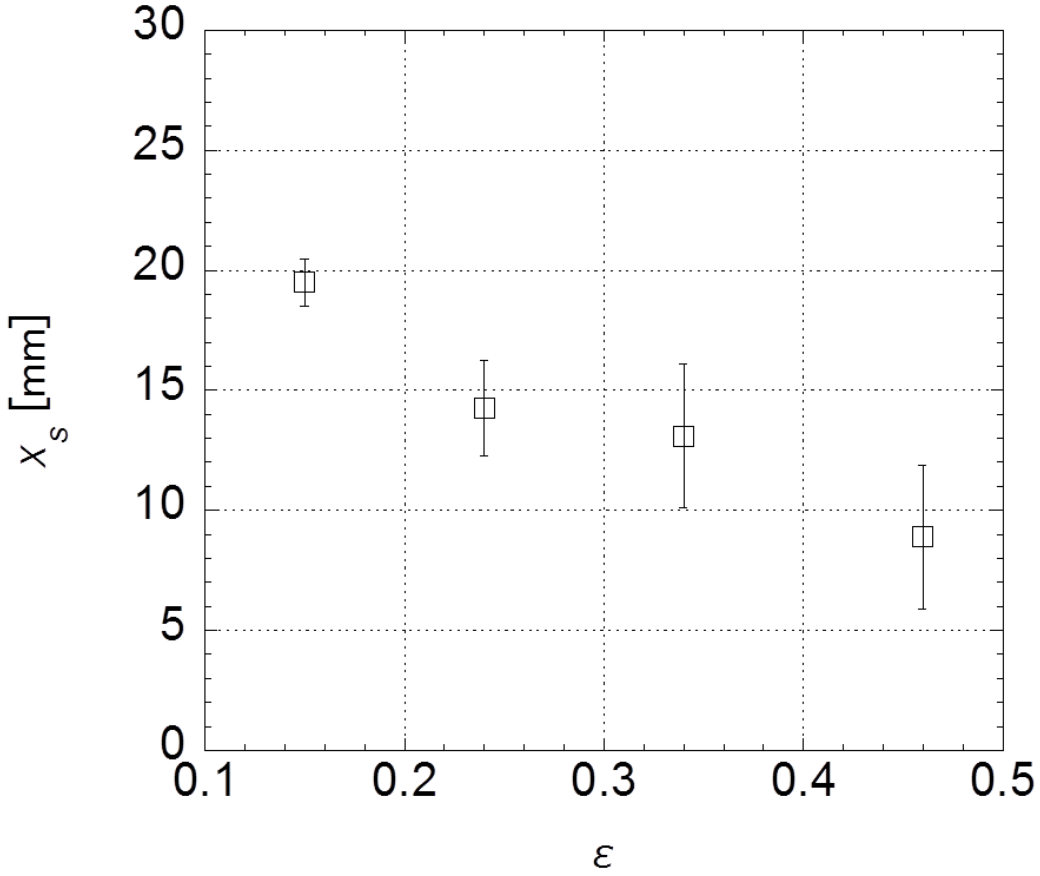

Fig. 4.11 Axial distance of stagnation point measured from cold exit at p_{in} = 0.4MPa

4.2.3 Temperature measurement

Figure 4.12 shows the results of the temperature measurement using the Type 1, 2, and 3 at p_{in} = 0.4MPa, ε = 0.1~0.9, and x = 3mm along the centerline. The vertical axis shows the temperature differences between inlet and cold flow temperature, $\Delta T_{t,cold}$. The horizontal axis shows the cold fraction, ε. From the figure, it is understood that the Type 3 measures the lowest temperature, which indicates its ability to measure the most accurate total temperature among the three probes.

Figure 4.13 shows a contour map of $\Delta T_{t,cold}$ in the cold flow measured at x = 3mm along the centerline. The thick curved line in the figure represents the boundary line of the direct/reversed flows, which is the same line as in Fig. 4.9. It can be seen from Fig. 4.13 that, at an arbitrary inlet pressure, $\Delta T_{t,cold}$ is almost constant in the reversed flow area regardless of the cold fraction variation. On the other hand, in the direct flow area, $\Delta T_{t,cold}$ increases at any arbitrary inlet pressure when the cold fraction is decreased from 1.0. In other words, the maximum $\Delta T_{t,cold}$ measured at x = 3mm along the centerline occurs around the boundary of direct/reversed flow or smaller ε area in the figure at an arbitrary inlet pressure. From the pressure and temperature measurement results, it is clear that the occurrence of a reversed flow around the center of the cold exit is closely related to the amount of temperature decrease in the cold flow. This observation is supported by the mathematical model analysis of an unconfined compressible vortex conducted by Katanoda and Mohd Hazwan[38], in which a static/total temperature, as well as a static pressure, at the center of a vortex flow is lower when a representative Mach number of the vortex increases, that is, the inlet pressure increases.

The mixing temperature of cold flow for p_{in} = 0.2 ~ 06MPa, ε = 0.1 ~ 0.9 are shown in Fig. 4.14. The horizontal axis of the figure shows the cold fraction, ε, and the vertical axis shows the temperature difference of mixing cold flow, $\Delta \bar{T}_{t,cold}$. It can be seen from this figure that $\Delta \bar{T}_{t,cold}$ increases as the cold fraction decreases. When the inlet pressure increases from 0.2MPa to 0.5MPa, $\Delta \bar{T}_{t,cold}$ increases at an arbitrary cold fraction. At p_{in} = 0.6MPa, $\Delta \bar{T}_{t,cold}$ is almost the same as that at p_{in} = 0.5MPa.

The mixing temperature of hot flow at p_{in} = 0.2 ~ 06MPa, ε = 0.1 ~ 0.9 are shown in Fig. 4.15. The horizontal axis of the figure shows the cold fraction, ε, and

the vertical axis shows the temperature difference of mixing hot flow, $\Delta\bar{T}_{t,hot}$. It can be seen from this figure that $\Delta\bar{T}_{t,hot}$ decreases as the cold fraction decreases. However, $\Delta\bar{T}_{t,hot}$ is less than 4K at p_{in} = 0.2MPa. When p_{in} is greater than or equal to 0.3MPa, $\Delta\bar{T}_{t,hot}$ increases as the inlet pressure increases at a cold fraction larger than 0.2. At a cold fraction smaller than 0.2, $\Delta\bar{T}_{t,hot}$ is around 5K at p_{in} = 0.2 ~ 0.6MPa. From Figs. 4.14 and 4.15, it can be concluded that, to obtain a lower temperature of cold flow, the value of cold fraction should be smaller. To obtain a higher temperature of hot flow, the value of cold fraction should be larger.

Figure 4.16 shows the cooling capacity of the VT. The horizontal axis of the figure shows the cold fraction, ε, and the vertical axis shows the cooling capacity, $\dot{Q}_c$[W]. From this figure, it can be understood that cooling capacity increases as the inlet pressure increases. At p_{in} = 0.3 ~ 06MPa, when the cold fraction decreases from 1, the cooling capacity increases until it reaches a maximum value, then cooling capacity decreases to 0 at ε = 0. Cooling capacity decreases at a small cold fraction due to the decrease in the mass flow rate of cold flow. The maximum value of cooling capacity in this research is obtained at p_{in} = 0.6MPa and ε = 0.4.

In order to see the heat balance of the VT, the contour map of non-dimensional heat loss of VT, $\Delta q_{loss}/c_p T_{atm}$, is shown in Fig. 4.17. The horizontal axis of the figure shows the cold fraction, ε, and the vertical axis shows the inlet pressure, p_{in}. This figure shows the existence of positive value of heat loss, which represents that heat is released from the VT to ambient air, and negative value of heat loss, which represents that heat is absorbed by the VT from ambient air. But, the heat loss is as small as within ±1.6% compared to the enthalpy of inlet air. Therefore, the VT used in this experiment is almost thermally insulated.

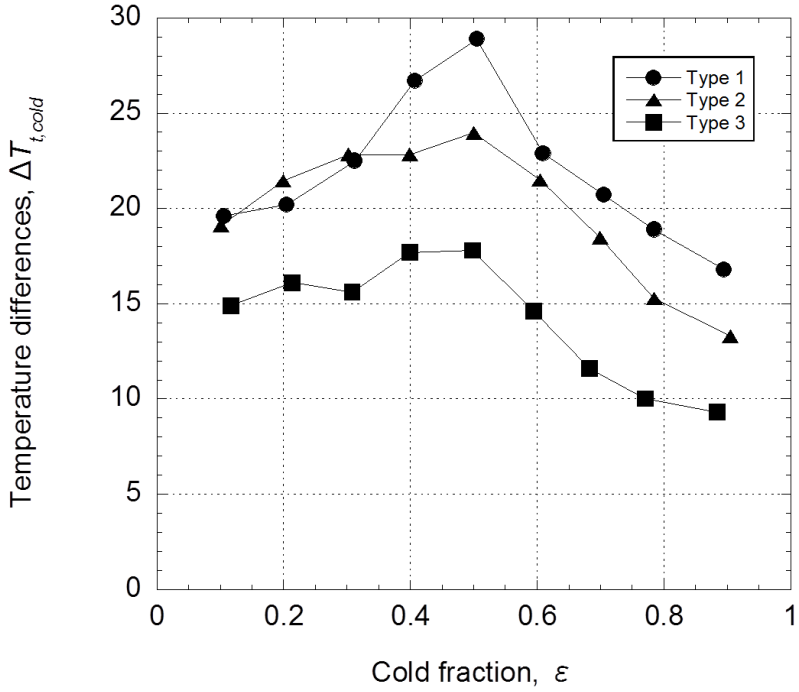

Fig. 4.12 Comparison of temperature measurement results obtained by three probes

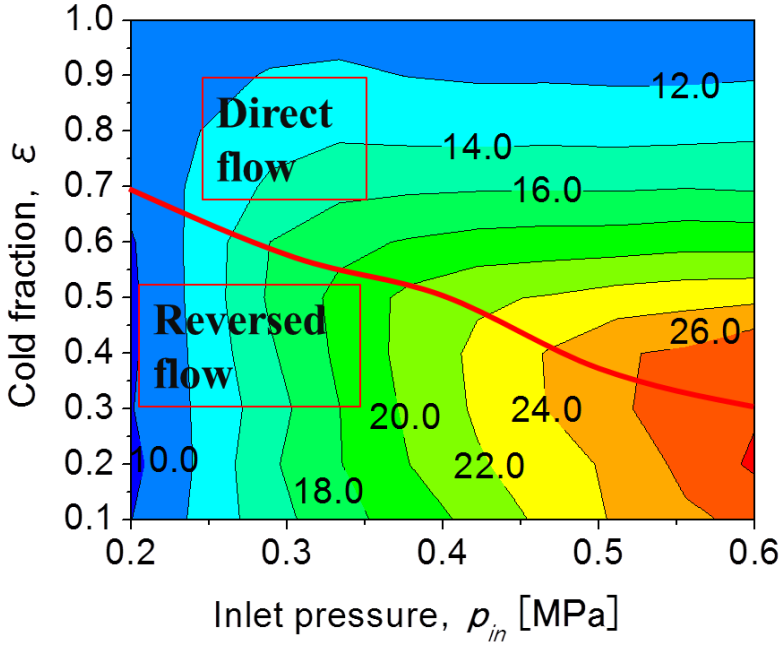

Fig. 4.13 Direct/reversed flow boundary line on contour map of total temperature differences $\Delta T_{t,cold}$ at x = 3mm on centerline

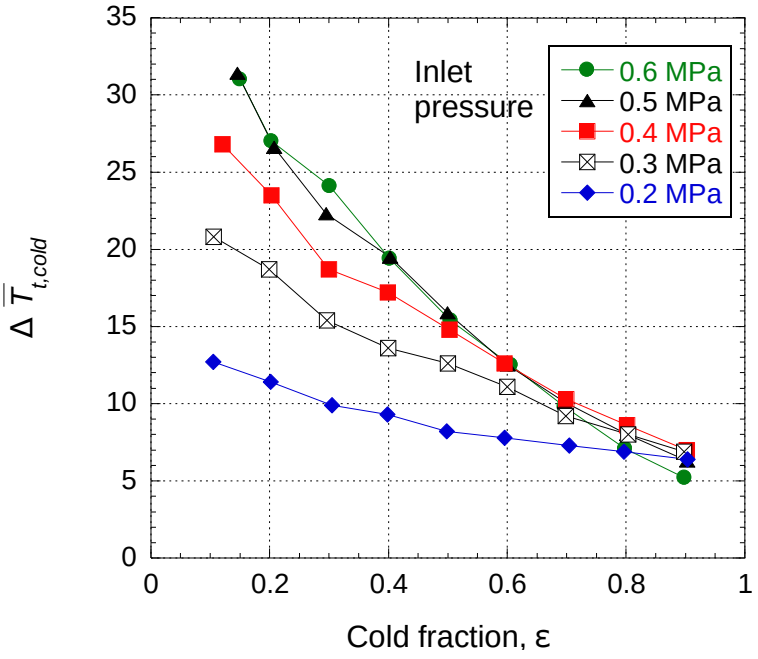

Fig. 4.14 Mixing temperature of cold flow

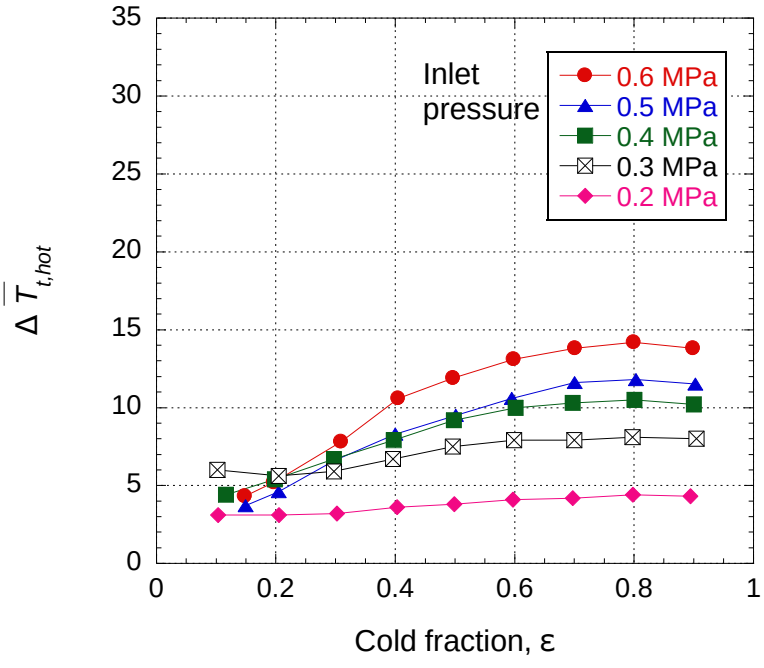

Fig. 4.15 Mixing temperature of hot flow

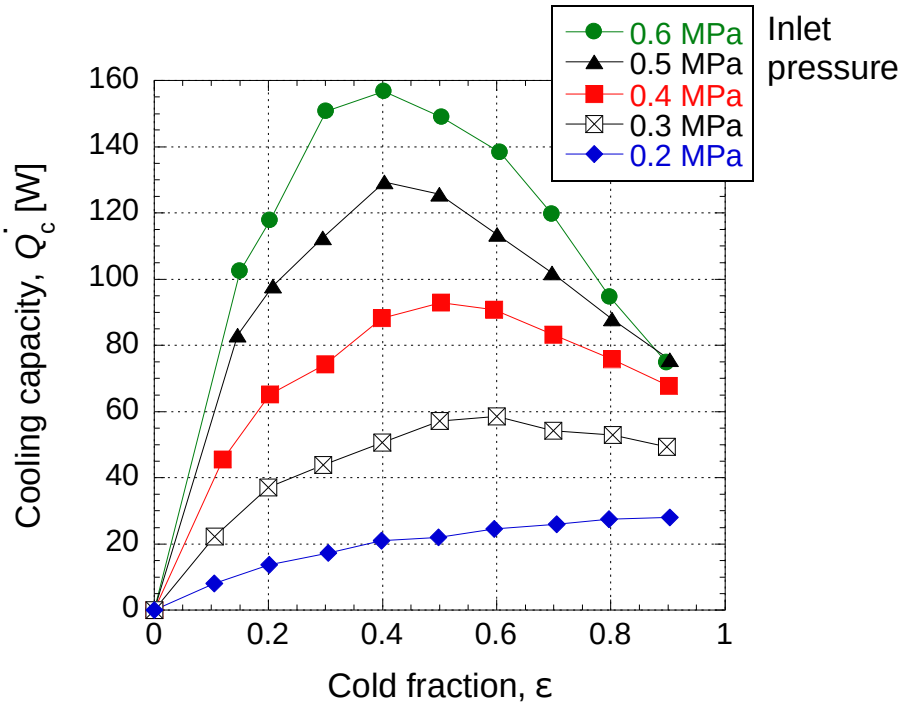

Fig. 4.16 Cooling capacity of VT

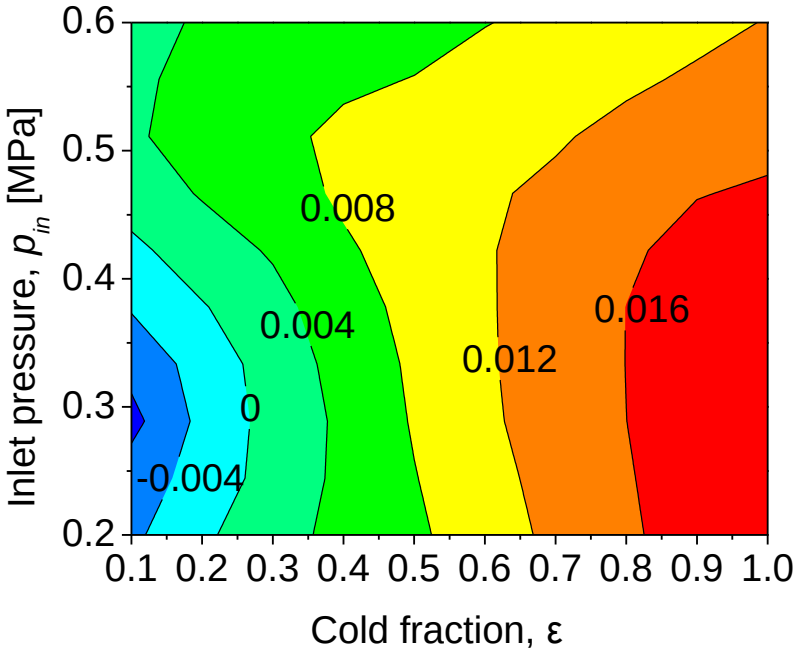

Fig. 4.17 Non-dimensional heat loss of VT, $\Delta q_{loss}/c_p T_{atm}$

4.2.4 Expected flow pattern

According to the literatures published in the past, some researchers performed experimental and numerical experiments to study the flow pattern inside of vortex tube [16-17]. Xue et al.[16] used a Cobra probe to measure the pressure inside a large VT with an inner diameter of 60 mm and a length 2000 mm. They proposed a flow pattern with a stagnation point exists inside of VT. According to their reports, a forced vortex formed near the inlet nozzle is transformed to a free vortex at the hot end side of the tube. The flow at the core of the tube is reversed to the cold exit before reaching the control valve and creates a stagnation point inside the tube. On the way moving to the cold exit, energy is transferred radially outwards from the core region. However, they didn't report the reversed flow at the cold exit which is supposed to occur. Behera et al.[17] numerically investigated the flow behavior and energy separation inside of VT. They report a different flow pattern in the VT from Xue et al.[16] with no stagnation point inside the tube. According to their reports, two layer of flow with different direction exist in the tube; a flow at the center of the tube moving from the control valve towards the cold exit of the tube, and another flow at the peripheral of the tube moving in a different direction which exits the tube from the hot exit. They also report that the energy separation occurs due to viscous shear in tangential direction. Just like Xue et al.[16], they didn't report about the reversed flow at the cold exit, which is believed to be one of the important factors to clarify the ESM.

Based on the experimental and analytical results obtained in this study and with aid of other works, expected flow patterns of the cold flow and in the vortex chamber are proposed in this subsection. Figure 4.18 shows the schematic flow pattern downstream of the cold exit pipe, based on the results of Figs. 4.9 and 4.12, when the cold fraction decreases at an arbitrary inlet pressure. At a larger cold fraction, Fig. 4.18(a), a shorter reversed flow region develops at the cold exit; the stagnation point of the reversed flow, x_s, is located at x_s < 3mm. At a medium cold fraction, Fig. 4.18(b), the stagnation point moves downstream to around x_s = 3mm. At a smaller cold fraction, Fig. 4.18(c), the reversed flow region extends more downstream; x_s > 3mm. According to numerical investigation by Dutta et.al.[36], shown in Fig. 4.19, the upstream end of above mentioned reversed flow closes inside of the cold exit pipe to form a recirculation vortex at a smaller cold fraction. Therefore, this recirculation zone shown in Fig. 4.18 is also thought to form a

recirculation vortex inside of the cold exit pipe. It should be noted that in Ref.[36] the pressure boundary condition at cold exit is fixed at 0.1MPa. From my measurement result, the Pitot pressure at the cold exit is lower than 0.1MPa for a smaller cold fraction. Therefore, the reversed flow region inside of cold exit tube should become larger than the simulation result obtained in Ref.[36].

Figure 4.20 shows the expected flow pattern inside and outside of the cold exit pipe. The recirculation vortex in the cold exit pipe is expected to be longer as the cold fraction decreases at an arbitrary inlet pressure. On the other hand, according to Takahama et al.[39] and Ahlborn et al.[40], the absolute value of the axial velocity at the center and radius of the central part decreases when decreasing the cold fraction. Therefore, the fluid dynamic cross-sectional area in the cold exit pipe must be smaller for a smaller cold fraction. Here, a smaller fluid dynamic cross-sectional area in the cold exit pipe means a larger cross-sectional area of the recirculation vortex. This enlargement of the radius of the recirculation vortex results in the elongation of the recirculation vortex at a smaller cold fraction.

From these results, the ESM of VT can be concluded as is shown in Fig. 4.21, regarding the effects of cold fraction and inlet pressure. The effect of cold fraction on ESM at an arbitrary inlet pressure can be explained as follows. From the experimental results obtained in the present study, when the cold fraction decreases from unity, the length of reversed flow, x_s increases. The increase in x_s implies the decrease in the pressure at the core of the vortex chamber when the cold fraction decreases. From the analytical studies, which will be explained in Chapter 5, when the pressure inside of the vortex chamber decreases, the tangential velocity increases. Simultaneously, the representative Mach number of the vortex increases. As a result, the static/total temperatures at the core of vortex decrease, and the static/total temperature in the outer region of the vortex increase.

Next, the effect of inlet pressure on the ESM at an arbitrary cold fraction can be explained as follows. When the inlet pressure increases, the tangential and Mach number increase, which results in a lower static/total temperatures at the core of vortex chamber and a higher static/total temperatures at the outer region of the vortex in the vortex chamber.

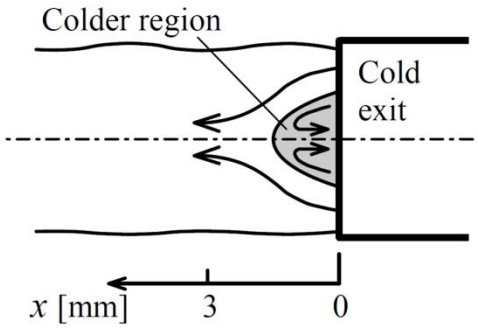

(a) Larger ε

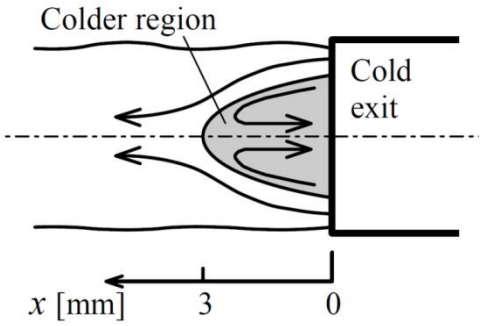

(b) Medium

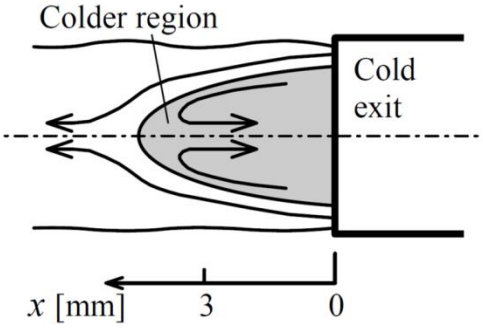

(c) Smaller ε

Fig. 4.18 Variation of expected flow pattern at the cold exit depending on ε at an arbitrary p_{in}

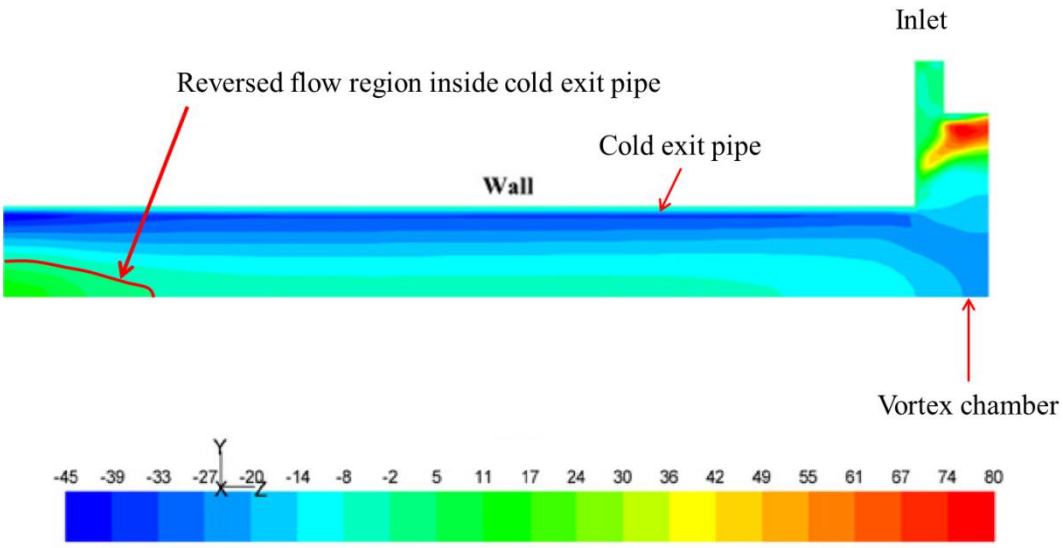

Fig. 4.19 Axial velocity distribution inside of cold exit pipe at a smaller cold fraction[36]

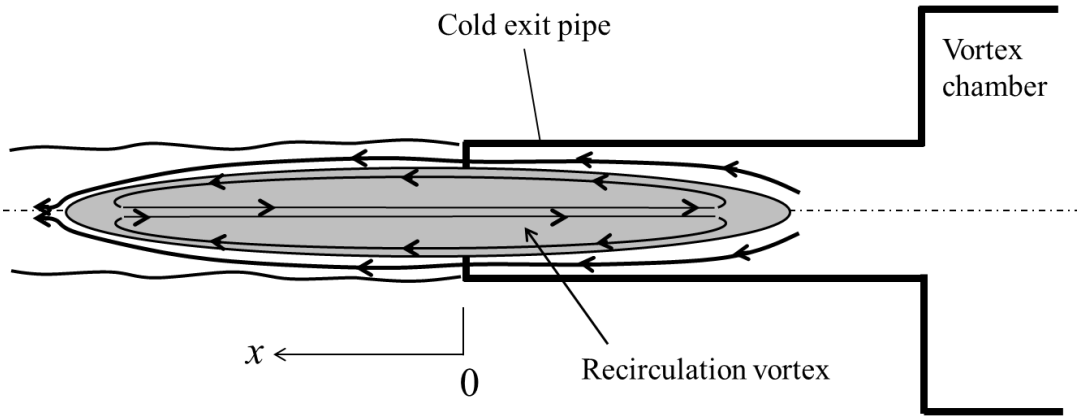

Fig. 4.20 Expected flow pattern inside of the cold exit at a lower cold fraction

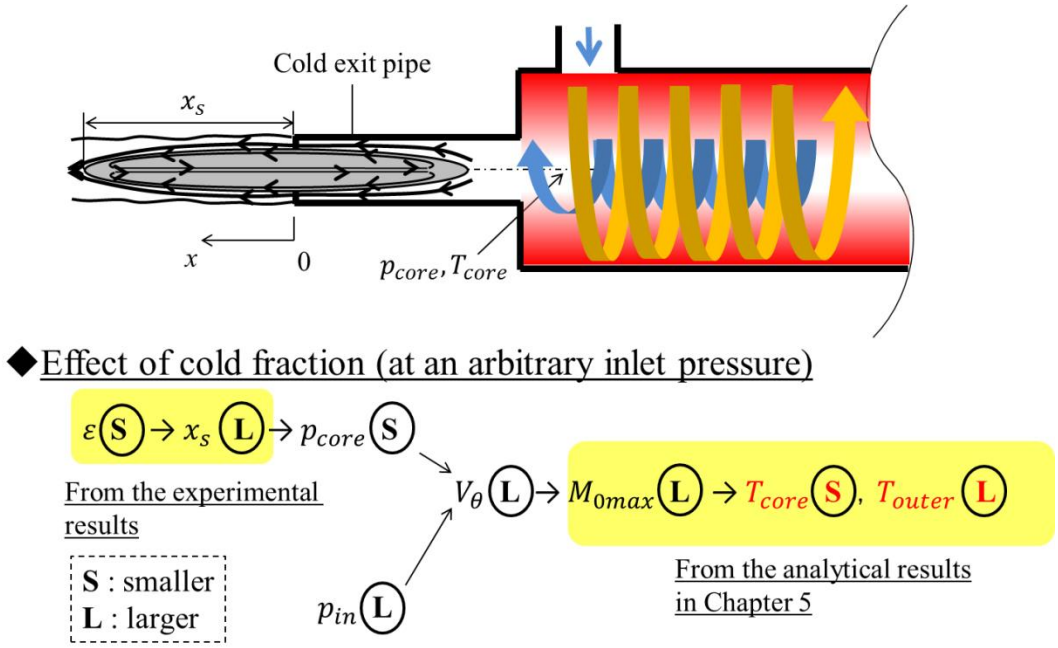

Fig. 4.21 Energy separation mechanism inside of VT

4.3 Conclusions

An experimental study of the Ranque-Hilsch VT was conducted, in order to clarify the flow structure of the cold exit flow. The total temperature and Pitot pressure of a cold flow center were measured. In addition, a simple flow visualization method was used to observe the reversed flow at the cold exit, and the mixing temperature of cold and hot flows is measured to determine the cooling capacity and heat loss of VT. The results obtained in this study are summarized as follows;

Structure of cold flow

(1) At a specific inlet pressure, when the cold fraction decreases from unity, the non-dimensionalized Pitot pressure inverts from $p_i / p_a > 1$ to $p_i / p_a < 1$.
(2) The flow visualization results indicate that a reversed flow is generated in the central part of the cold exit. The axial length of the reversed flow, measured from the cold exit, increases with decreasing the cold fraction at an arbitrary inlet pressure.
(3) A recirculation vortex is formed inside of the cold exit pipe.
(4) The total temperature at the center of cold exit in the reversed flow is lower than that in the direct flow at the cold exit.
(5) The mixing temperature of cold flow increases when the cold fraction decreases. On the other hand, the mixing temperature of hot flow decreases when the cold fraction decreases.
(6) The maximum cooling capacity of VT is obtained at $p_{in} = 0.6$MPa and $\varepsilon = 0.4$.

ESM of counter flow VT

(7) When the cold fraction decreases from unity at an arbitrary inlet pressure, the pressure at the center of vortex chamber decreases since the axial length of reversed flow increases. A lower pressure in the vortex chamber means a lower static/total temperatures at the core of vortex chamber and a higher static/total temperatures at the outer region of the vortex in the vortex chamber.
(8) When the inlet pressure increases at an arbitrary cold fraction, the tangential velocity increases, which results in a lower static/total temperatures at the core of the vortex chamber and a higher static/total temperatures at the outer region of the vortex in the vortex chamber.

5. Mathematical Model Analysis of Compressible Vortex Flow

The driving force of energy separation in VT is a high-speed vortical flow caused in a vortex chamber. In this chapter, mathematical model of an unconfined isolated compressible vortex is introduced under the expectation that the ESM in an unconfined vortex is almost the same as that in a confined vortex, which can be seen in the VT. The physical reason of ESM in an unconfined isolated compressible vortex will be provided in this chapter based on the mathematical model.

5.1 Background

The ESM in VT has been tried to explain by many researchers. Mack[41] solved radial momentum and energy conservation equations along with irrotational and rotational tangential velocity formulas for unconfined compressible laminar vortex. He shows that total temperature of the vortical flow decreases towards the vortex center if Prandtl number is larger than a specific value. Sibulkin[44] solves the unsteady momentum and energy equations for two-dimensional, axisymmetric flow of gas/liquid in a cylinder with finite radius for the purpose of clarifying the ESM in VT. He used finite difference method to solve the equations under the assumption of M (Mach number) << 1. Although he discusses transient energy transfer process in a confined two dimensional vortex for a set of specific initial conditions, his results does not explain the ESM in VT because his numerical solutions of physical properties, including temperature, become uniform in the entire flow field at a time of inifinity. Takahama and Soga[39] and Takahama[45] propose flow model by solving two-dimensional, axisymmetric conservation equations of mass, radial momentum and energy with empirical tangential velocity in the peripheral region of the vortex, under the assumption of constant density. Based on the model analysis and experiment, they explain the ESM in the counter-flow VT by turbulent mixing and heat transfer at the boundary of cold/hot flows; while flowing axial unit-length from hot- to cold-end, more heat is transferred from inner to outer gas compared to the amount of increase in kinetic energy of the inner flow, resulting in a lower temperature at the cold end and a higher temperature at the hot exit. However, the occurrence of heat transfer from colder core to hotter peripheral flow is impractical. Ahlborn, et al.[46] shows the upper limit of hotter gas temperature and lower limit of colder gas temperature of

counter-flow VT from his mathematical model. However, his model incorporates several empirical equations derived from his experimental data with relatively large statistical dispersion. Not only his model does not explain the physical reason of ESM but also validity and universality of his model are unclear.

Amitani et al.[47] tries to clarify ESM by numerically solving axisymmetric Euler equations. However, they use impractical boundary conditions in order to mimic a vortical flow, making their numerical results unreliable. Recently, turbulent numerical simulations of counter-flow VT has been conducted by many researchers [17, 36, 48-49]. They propose based on the numerical results that the energy separation occurs due to the balance between viscous shear work and heat transfer along the boundary surface of cold and hot flow regions in the VT. However, the ESM in the vortex chamber is not well explained.

Besides numerical simulation, mathematical modeling of compressible vortex is also evolving. Vatistas and Aboelkassem[42] proposes mathematical model of laminar unconfined compressible vortex which is intended to apply to the vortical flow in VT. But their model is applicable only for laminar flow although the flows in VT in most cases are expected to be turbulent. Badwal[43] extended their laminar model to turbulent vortex. Although the mathematical model of Refs.[42] and [43] are for an unconfined vortex, they employ only several acceptable assumptions, making the model reliable. In this research, mathematical model derived in Refs.[42] and [43] is called VAB model, which is used in the present analysis with improvement.

It is well known that the thermal efficiency of the uni-flow tube is generally lower than that of the counter-flow tube [7]. It means that the counter-flow VT has additional ESM compared to uni-flow VT. Figure 5.1 shows complicated flow pattern proposed in Ref.[50]. Although the mathematical model of unconfined vortex, schematically shown in Fig. 5.2, is more directly applicable to an uni-flow VT, the author believes that its physics of ESM is also true for the vortical flow generated in a vortex chamber in a counter-flow VT.

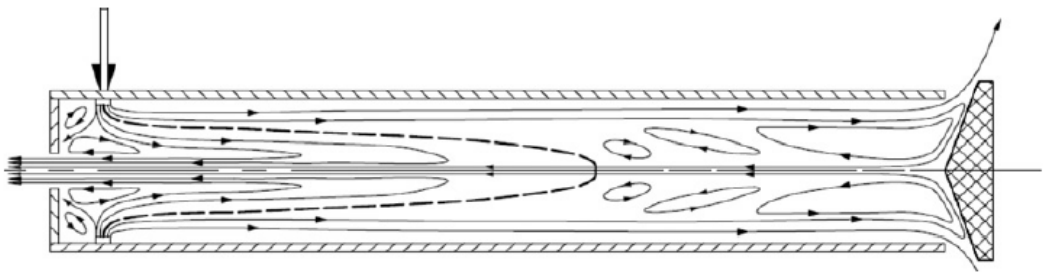

Fig. 5.1 Flow pattern in a counter-flow VT proposed in Ref.[50]

5.2 Review of VAB model

5.2.1 Basic Equations

The basic equations for compressible axisymmetric vortex are the equations of mass continuity, Navier-Stokes, and energy in cylindrical coordinate (r, θ, z), and are written as;

$$\frac{\partial \rho}{\partial t}+\frac{1}{r}\frac{\partial(\rho V_r r)}{\partial r}+\frac{1}{r}\frac{\partial(\rho V_\theta)}{\partial \theta}+\frac{\partial(\rho V_z)}{\partial z}=0 \tag{5.1}$$

$$\frac{DV_r}{Dt}-\frac{V_\theta^2}{r}=\frac{1}{\rho}\left(\frac{\partial \sigma_r}{\partial r}+\frac{\sigma_r}{r}-\frac{\sigma_\theta}{r}+\frac{\partial \tau_{r\theta}}{r\partial \theta}+\frac{\partial \tau_{zr}}{\partial z}\right) \tag{5.2}$$

$$\frac{DV_\theta}{Dt}+\frac{V_r V_\theta}{r}=\frac{1}{\rho}\left(\frac{\partial \sigma_\theta}{r\partial \theta}+\frac{\partial \tau_{r\theta}}{\partial r}+\frac{\tau_{r\theta}}{r}+\frac{\tau_{\theta r}}{r}+\frac{\partial \tau_{z\theta}}{\partial z}\right) \tag{5.3}$$

$$\frac{DV_z}{Dt}=\frac{1}{\rho}\left(\frac{\partial \tau_{rz}}{\partial r}+\frac{\tau_{rz}}{r}+\frac{\partial \tau_{\theta z}}{r\partial \theta}+\frac{\partial \sigma_z}{\partial z}\right) \tag{5.4}$$

$$c_p\frac{DT}{Dt}-\frac{1}{\rho}\frac{Dp}{Dt}=\frac{k}{\rho}\nabla^2 T+\frac{\Phi}{\rho} \tag{5.5}$$

where, t is the time, ρ is the density, p is the pressure, T is the temperature, (V_r, V_θ, V_z) is the velocity of (r, θ, z) components, c_p is the specific heat at constant pressure, k is the thermal conductivity, respectively. The normal stress σ and tangential stress τ are expressed as;

$$\left.\begin{aligned}
\sigma_r &= -p+2\mu\frac{\partial V_r}{\partial r}-\frac{2}{3}\mu\cdot div\mathbf{V}\\
\sigma_\theta &= -p+2\mu\left(\frac{1}{r}\frac{\partial V_\theta}{\partial \theta}+\frac{V_r}{r}\right)-\frac{2}{3}\mu\cdot div\mathbf{V}\\
\sigma_z &= -p+2\mu\frac{\partial V_r}{\partial z}-\frac{2}{3}\mu\cdot div\mathbf{V}\\
\tau_{r\theta} &= \tau_{\theta r}=\mu\left\{r\frac{\partial}{\partial r}\left(\frac{V_\theta}{r}\right)+\frac{1}{r}\frac{\partial V_r}{\partial \theta}\right\}\\
\tau_{z\theta} &= \mu\left(\frac{1}{r}\frac{\partial V_z}{\partial \theta}+\frac{\partial V_\theta}{\partial z}\right)\\
\tau_{zr} &= \mu\left(\frac{\partial V_r}{\partial z}+\frac{\partial V_z}{\partial r}\right)
\end{aligned}\right\} \tag{5.6}$$

$$\left.\begin{aligned}
\frac{D}{Dt} &= \frac{\partial}{\partial t}+V_r\frac{\partial}{\partial r}+\frac{V_\theta}{r}\frac{\partial}{\partial \theta}+V_z\frac{\partial}{\partial z}\\
\nabla^2 &= \frac{\partial^2}{\partial r^2}+\frac{1}{r}\frac{\partial}{\partial r}+\frac{1}{r}\frac{\partial^2}{\partial \theta^2}+\frac{\partial^2}{\partial z^2}\\
div\mathbf{V} &= \frac{1}{r}\frac{\partial(rV_r)}{\partial r}+\frac{1}{r}\frac{\partial V_\theta}{\partial \theta}+\frac{\partial V_z}{\partial z}
\end{aligned}\right\} \tag{5.7}$$

where, μ is the coefficient of viscosity. The function Φ in Eq.(5.5) is an energy

dissipation function, and is written as;

$$\begin{aligned}\Phi = 2\mu&\left\{\left(\frac{\partial V_r}{\partial r}\right)^2+\left(\frac{1}{r}\frac{\partial V_\theta}{\partial \theta}+\frac{V_r}{r}\right)^2+\left(\frac{\partial V_z}{\partial z}\right)^2\right\}\\&+\mu\left\{r\frac{\partial}{\partial}\left(\frac{V_\theta}{r}\right)+\frac{1}{r}\frac{\partial V_r}{\partial \theta}\right\}^2+\mu\left(\frac{1}{r}\frac{\partial V_z}{\partial \theta}+\frac{\partial V_\theta}{\partial z}\right)^2+\mu\left(\frac{\partial V_r}{\partial z}+\frac{\partial V_z}{\partial r}\right)^2\end{aligned} \tag{5.8}$$

When focusing on a steady and axisymmnetric vortical flow, above equations are simplified as;

$$\frac{1}{r}\frac{\partial(\rho V_r r)}{\partial r}+\frac{\partial(\rho V_z)}{\partial z}=0 \tag{5.1'}$$

$$\left(V_r\frac{\partial V_r}{\partial r}+V_z\frac{\partial V_r}{\partial z}\right)-\frac{V_\theta^2}{r}=\frac{1}{\rho}\left(\frac{\partial \sigma_r}{\partial r}+\frac{\sigma_r}{r}-\frac{\sigma_\theta}{r}+\frac{\partial \tau_{zr}}{\partial z}\right) \tag{5.2'}$$

$$V_r\frac{\partial V_\theta}{\partial r}+\frac{V_r V_\theta}{r}=\frac{1}{\rho}\left(\frac{\partial \tau_{r\theta}}{\partial r}+2\frac{\tau_{r\theta}}{r}+\frac{\partial \tau_{z\theta}}{\partial z}\right) \tag{5.3'}$$

$$\frac{DV_z}{Dt}=\frac{1}{\rho}\left(\frac{\partial \tau_{rz}}{\partial r}+\frac{\tau_{rz}}{r}+\frac{\partial \sigma_z}{\partial z}\right) \tag{5.4'}$$

$$c_p\left(V_r\frac{\partial T}{\partial r}+V_z\frac{\partial T}{\partial z}\right)-\frac{1}{\rho}\left(V_r\frac{\partial p}{\partial r}+V_z\frac{\partial p}{\partial z}\right)=\frac{k}{\rho}\left(\frac{\partial^2 T}{\partial r^2}+\frac{1}{r}\frac{\partial T}{\partial r}+\frac{\partial^2 T}{\partial z^2}\right)+\frac{\Phi}{\rho} \tag{5.5'}$$

$$\left.\begin{aligned}\sigma_r &= -p+2\mu\frac{\partial V_r}{\partial r}-\frac{2}{3}\mu\cdot div\mathbf{V}\\ \sigma_\theta &= -p+2\mu\frac{V_r}{r}-\frac{2}{3}\mu\cdot div\mathbf{V}\\ \sigma_z &= -p+2\mu\frac{\partial V_r}{\partial z}-\frac{2}{3}\mu\cdot div\mathbf{V}\\ \tau_{r\theta} &= \tau_{\theta r}=\mu r\frac{\partial}{\partial r}\left(\frac{V_\theta}{r}\right)\\ \tau_{z\theta} &= \mu\frac{\partial V_\theta}{\partial z}\\ \tau_{zr} &= \mu\left(\frac{\partial V_r}{\partial z}+\frac{\partial V_z}{\partial r}\right)\end{aligned}\right\} \tag{5.6'}$$

$$\left.\begin{aligned}\frac{D}{Dt} &= V_r\frac{\partial}{\partial r}+V_z\frac{\partial}{\partial z}\\ \nabla^2 &= \frac{\partial^2}{\partial r^2}+\frac{1}{r}\frac{\partial}{\partial r}+\frac{\partial^2}{\partial z^2}\\ div\mathbf{V} &= \frac{1}{r}\frac{\partial(rV_r)}{\partial r}+\frac{\partial V_z}{\partial z}\end{aligned}\right\} \tag{5.7'}$$

$$\Phi = 2\mu\left\{\left(\frac{\partial V_r}{\partial r}\right)^2 + \left(\frac{V_r}{r}\right)^2 + \left(\frac{\partial V_z}{\partial z}\right)^2\right\} + \mu\left\{r\frac{\partial}{\partial r}\left(\frac{V_\theta}{r}\right)\right\}^2 + \mu\left(\frac{\partial V_\theta}{\partial z}\right)^2 + \mu\left(\frac{\partial V_r}{\partial z} + \frac{\partial V_z}{\partial r}\right)^2 \quad (5.8')$$

In the VAB model, following set of vortical velocity component is assumed;

$$[V_r(r),\quad V_\theta(r),\quad V_z(z,r)] \qquad (5.9)$$

$$V_z(z,r) = z \cdot h(r) \qquad (5.10)$$

That is, the radial and tangential velocity components are assumed to be the function of r only and unchanged in the axial direction. The axial velocity component is a function of r and z, however, h is assumed to be a function of r only.

Here, non-dimensionalized thermo-physical properties are introduced as;

$$\left.\begin{aligned} &V_r' = \frac{V_r}{V_{\theta c}}, \qquad V_\theta' = \frac{V_\theta}{V_{\theta c}}, \qquad V_z' = \frac{V_z}{V_{\theta c}} \\ &p' = \frac{p}{\rho_\infty V_{\theta c}^2}, \qquad \rho' = \frac{\rho}{\rho_\infty}, \qquad T' = \frac{T}{T_\infty} \\ &r' = \frac{r}{r_c}, \qquad z' = \frac{z}{r_c} \end{aligned}\right\} \qquad (5.11)$$

where, $V_{\theta c}$ is a tangential velocity of the Rankine vortex at $r = r_c$. It is written as;

$$V_{\theta c} = \frac{\Gamma_\infty}{2\pi r_c} \qquad (5.12)$$

where, Γ_∞ is the vortex circulation. The subscript ∞ shows physical properties distant from the vortex core in the radial direction. The velocity components in Eq. (5.9) and Eq. (5.10) are non-dimensionalized as;

$$[V_r'(r'),\quad V_\theta'(r'),\quad V_z'(z',r')] \qquad (5.9')$$

$$V_z'(z',r') = z' \cdot h(r') \qquad (5.10')$$

The order of magnitude of the non-dimensional properties in Eq. (5.11) are estimated as;

$$\begin{aligned} &V_r' \sim \delta, \qquad V_\theta' \sim 1, \qquad V_z' \sim \delta \qquad (0 < \delta << 1) \\ &p' \sim 1, \qquad \rho' \sim 1, \qquad T' \sim 1 \\ &r' \sim 1, \qquad z' \sim 1 \end{aligned} \qquad (5.13)$$

By applying Eq. (5.11) to Eq. (5.1'), we obtain

$$\frac{1}{r'}\frac{\partial(\rho' V_r' r')}{\partial r'} + \frac{\partial(\rho' V_z')}{\partial z'} = 0$$

Note that *h'* in Eq. (5.10') is a function of only *r'*, and applying the order estimation, Eq. (5.13), to the above equation, we obtain

$$\frac{1}{r'}\frac{d(\rho' V_r' r')}{dr'} + \rho' h' = 0 \qquad (5.14)$$

Here, ρ' is assumed to be a function of *r'* only.

Next, application of Eq. (5.11), as well as Eq. (5.13), to Eq. (5.2') yields,

$$\rho' \frac{V_\theta'^2}{r'} = \frac{\partial p'}{\partial r'} \qquad (5.15)$$

When deriving the above equation, the Reynolds number R_e defined by Eq. (5.16) is used.

$$R_e = \frac{\rho_\infty V_{\theta c} r_c}{\mu} \sim \frac{1}{\delta} \qquad (5.16)$$

Application of Eq. (5.11), as well as Eq. (5.13), to Eq. (5.3') and (5.4') yields,

$$\rho' R_e \frac{V_r'}{r'}\frac{d(V_\theta' r')}{dr'} = \frac{d}{dr'}\left\{\frac{1}{r'}\frac{d(V_\theta' r')}{dr'}\right\} \qquad (5.17)$$

$$\frac{\partial p'}{\partial z'} = 0 \qquad (5.18)$$

Equation (5.18) shows that pressure is independent of *z'*, and a function of *r'* only. Therefore, Eq. (5.15) is rewritten as,

$$\rho' \frac{V_\theta'^2}{r'} = \frac{dp'}{dr'} \qquad (5.15')$$

Since density is assumed to be a function of *r'* only, as mentioned before, and pressure is also a function of *r'* only, as indicated by Eq. (5.18), temperature is also a function of *r'*.

Finally, application of Eqs. (5.11) and (5.13) to Eq. (5.5') yields,

$$\rho' P_r R_e V_r' \frac{dT'}{dr'} - P_r R_e (\gamma - 1) M_{oc}^2 V_r' \frac{dp'}{dr'} = \frac{1}{r'}\frac{d}{dr'}\left(r' \frac{dT'}{dr'}\right) + P_r (\gamma - 1) M_{oc}^2 F' \qquad (5.19)$$

where,

$$M_{oc} = \frac{V_{\theta c}}{\sqrt{\gamma R T_\infty}} \qquad (5.20)$$

$$F' = r'^2 \left\{\frac{d}{dr'}\left(\frac{V_\theta'}{r'}\right)\right\}^2 \qquad (5.21)$$

$$P_r = \frac{c_p \mu}{k} \tag{5.22}$$

The equation of state of the ideal gas is,

$$p = \rho RT \tag{5.23}$$

Application of Eq. (5.11) to the above equation yields,

$$p' = \frac{\rho' T'}{\gamma M_{oc}^2} \tag{5.24}$$

or

$$\frac{p}{p_\infty} = \rho' T' \tag{5.24'}$$

In summary the non-dimensional equations to be solved are;

$$\frac{1}{r'}\frac{d(\rho' V_r' r')}{dr'} + \rho' h' = 0 \tag{5.14}$$

$$\rho' \frac{V_\theta'^2}{r'} = \frac{dp'}{dr'} \tag{5.15'}$$

$$\rho' R_e \frac{V_r'}{r'}\frac{d(V_\theta' r')}{dr'} = \frac{d}{dr'}\left\{\frac{1}{r'}\frac{d(V_\theta' r')}{dr'}\right\} \tag{5.17}$$

$$\rho' P_r R_e V_r' \frac{dT'}{dr'} - P_r R_e (\gamma - 1) M_o^2 V_r' \frac{dp'}{dr'} = \frac{1}{r'}\frac{d}{dr'}\left(r' \frac{dT'}{dr'}\right) + P_r (\gamma - 1) M_{oc}^2 F' \tag{5.19}$$

where,

$$V_z' = z' h' \tag{5.11''}$$

The equations to be solved, Eqs.（5.14），（5.15’），（5.17），（5.19），（5.24），include 6 unknowns. Therefore, one variable must be modeled in order close this system. Now, non-dimenzional velocity $V/V_{\theta c}$ is rewritten as $\mathcal{V}$, and another non-dimenzional velocity $V/V_{\theta max}$ ($V_{\theta max}$; maximum tangential velocity of vortex) is rewritten as V'. In the VAB model, the following tangential velocity distribution is provided based on the experimental results;

$$\mathcal{V}_\theta = \frac{V_\theta}{V_{\theta c}} = r'\left(\frac{a}{a + r'^4}\right)^m \tag{5.25}$$

$$V_\theta' = \frac{V_\theta}{V_{\theta \max}} = r'\left(\frac{a+1}{a + r'^4}\right)^m \tag{5.25'}$$

where,

$$m = \frac{a+1}{4} \tag{5.26}$$

The factor a is determine to reproduce the actual tangential velocity of compressible vortex and is given as;

$$a = \begin{cases} 1.0 & \text{(laminar vortex)} \\ \\ 0.7 & \text{(turbulent vortex)} \end{cases} \qquad (5.27)$$

By setting $V_\theta = V_{\theta\max}$ at $r'=1$ in Eq. (5.25) for laminar flow, we obtain

$$\frac{V_{\theta\max}}{V_{\theta c}} = \left(\frac{a}{a+1}\right)^m \qquad (5.28)$$

The above equation shows how much the maximum tangential velocity decelerates in VAB model, compared to that of the Rankine vortex at an arbitrary value of *a*. The variation of $V_{\theta\max}/V_{\theta c}$ for $a = 0-1$ is shown in Fig. 5.3. $V_{\theta\max}/V_{\theta c}$ is 0.707 at $a = 1$ (laminar vortex) and 0.686 at $a = 0.7$ (turbulent vortex).

Here we introduce two new variables as;

$$U' = \rho' R_e V_r', \qquad H' = \rho' R_e h' \qquad (5.29)$$

By applying above equations to Eq. (5.14),

$$\frac{1}{r'}\frac{d(U'r')}{dr'} + H' = 0 \quad \text{[Conservation of mass]} \qquad (5.30)$$

Radial momentum equation is reduced to;

$$\rho'\frac{V_\theta'^2}{r'} = \frac{dp'}{dr'} \qquad \text{[Radial momentum equation]} \qquad (5.15')$$

Equation (5.17) can be expressed as follows using the first equation of Eq. (5.29);

$$\frac{U'}{r'}\frac{d(V_\theta' r')}{dr'} = \frac{d}{dr'}\left\{\frac{1}{r'}\frac{d(V_\theta' r')}{dr'}\right\} \qquad \text{[Tangential momentum equation]} \quad (5.31)$$

Substitution of Eq. (5.15') and (5.29) to Eq. (5.19) yields,

$$\frac{1}{r'}\frac{d}{dr'}\left(r'\frac{dT'}{dr'}\right) - P_r U'\frac{dT'}{dr'} = -P_r(\gamma-1)M_{oc}^2\left(F' + \frac{U'V_\theta'^2}{r'}\right)$$

$$\text{[Energy equation]} \qquad (5.32)$$

Equation of state, again, is,

$$p' = \frac{\rho' T'}{\gamma M_{oc}^2} \qquad (5.24)$$

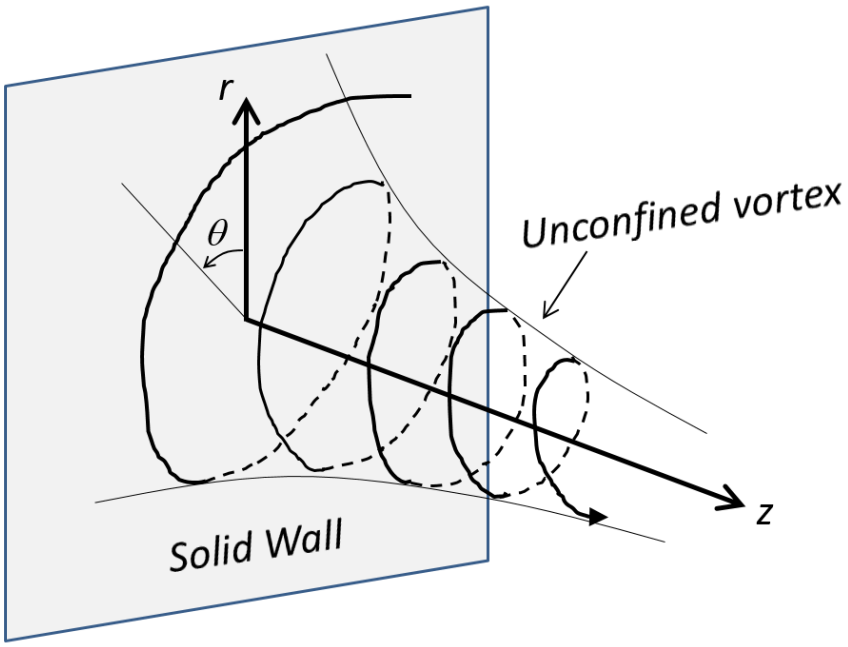

Fig. 5.2 Unconfined compressible vortex in cylindrical coordinate (r, θ, z)

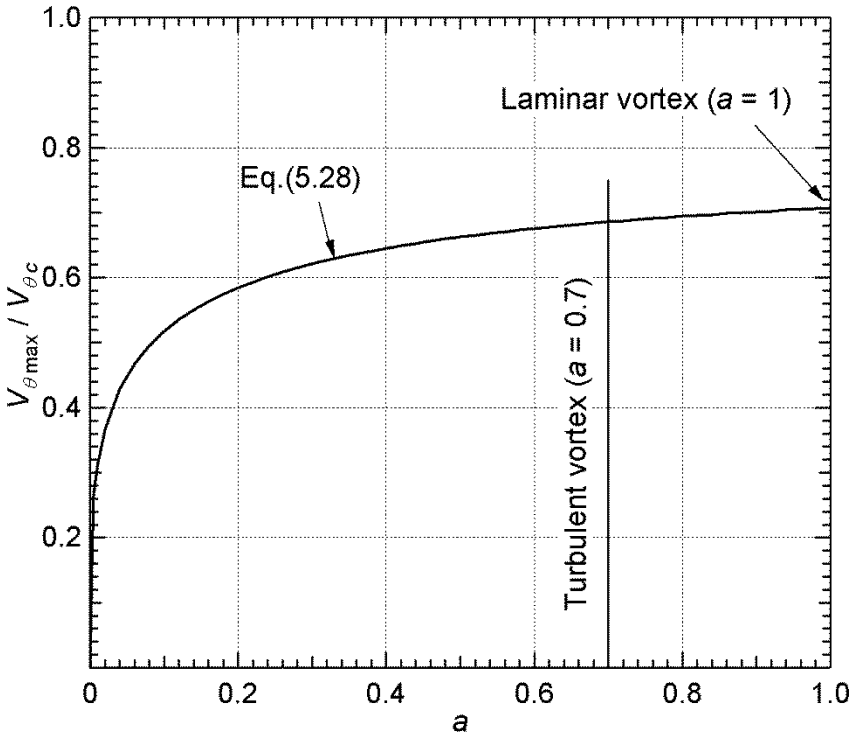

Fig. 5.3 Decay of maximum tangential velocity against the value of a

5.2.2 Laminar Vortex Solutions

For a laminar compressible vortex, the parameter *a* in Eq. (5.25) is set at 1 so that the tangential velocity equation closely reproduce the experimental tangential velocity of laminar compressible vortex. That is, from Eq. (5.25) tangential velocity is expressed as;

$$V_\theta = \frac{r'}{\sqrt{1+r'^4}} \tag{5.33}$$

The boundary conditions are;

$$\begin{aligned} &1)\ \text{at}\ \ r'=0; \quad V_\theta(r')=0,\ \ U'(r')=0,\ \ \frac{dH'(r')}{dr'}=0,\ \ \frac{dT'(r')}{dr'}=0 \\ &2)\ \text{at}\ \ r'=\infty; \quad V_\theta r'=1,\ \ T'(r')=1,\ \ \rho'(r')=1,\ \ \gamma M_{oc}^2 p'=1 \end{aligned} \tag{5.34}$$

It should be noted that above boundary conditions, except $V_\theta r'=1$, are also applicable to the turbulent vortex explained in the next section.

Mathematical solutions of newly introduced variables, U' and H', in Eq. (5.29) and T' which satisfy Eqs. (5.30)-(5.32) and Eq. (5.34) are obtained as;

$$\begin{cases} U' = \rho' R_e V_r' = -\dfrac{6r'^3}{1+r'^4} & (5.35) \\ H' = \rho' R_e h' = \dfrac{24r'^2}{\left(1+r'^4\right)^2} \qquad \left(V_z = z'\dfrac{H'}{\rho' R_e} = \dfrac{z'}{\rho' R_e}\dfrac{24r'^2}{\left(1+r'^4\right)^2} \right) & (5.36) \\ T' = 1+\dfrac{\gamma-1}{6}M_{oc}^2\left\{\tan^{-1}(r'^2)-\dfrac{r'^2}{1+r'^4}-\dfrac{\pi}{2}\right\} & (5.37) \end{cases}$$

Equation (5.37) is obtained under the condition of;

$$P_r = \frac{2}{3} \tag{5.38}$$

Finally density equation is derived. Derivation of Eq. (5.24) by r' yields;

$$\frac{dp'}{dr'} = \frac{1}{\gamma M_{oc}^2}\left(\frac{d\rho'}{dr'}T' + \rho'\frac{dT'}{dr'}\right) \tag{5.39}$$

By substituting Eq. (5.15') to Eq. (5.39);

$$\frac{d}{dr'}\ln\left(\rho' T'\right) = \gamma M_{oc}^2 \frac{V_\theta^2}{r'T'} \tag{5.40}$$

Integration of above equation about r', from 0 to r' yields;

$$\rho' = \frac{\exp\left[\gamma M_{oc}^2\left(\int_0^{r'}\frac{V_\theta^2}{r'T'}dr' - C\right)\right]}{T'} \tag{5.41}$$

The integration constant C in the above equation can be determined by the boundary condition of ρ' in Eq. (5.34) at $r' \to \infty$ as;

$$\lim_{r'\to\infty} \rho' = \frac{\lim_{r'\to\infty} \exp\left[\gamma M_{oc}^2 \left(\int_0^{r'} \frac{V_\theta^2}{r'T'} dr' - C\right)\right]}{\lim_{r'\to\infty} T'} = \frac{\lim_{r'\to\infty} \exp\left[\gamma M_{oc}^2 \left(\int_0^{r'} \frac{V_\theta^2}{r'T'} dr' - C\right)\right]}{1} = 1 \tag{5.42}$$

Therefore

$$C = \int_0^{\infty} \frac{V_\theta^2}{r'T'} dr' \tag{5.43}$$

By substituting Eq. (5.43) to Eq. (5.41), non-dimensionalized density equation can be obtained as;

$$\rho' = \frac{\exp\left[\gamma M_{oc}^2 \left(\int_{0c}^{r'} \frac{V_\theta^2}{r'T'} dr' - \int_0^{\infty} \frac{V_\theta^2}{r'T'} dr'\right)\right]}{T'} \tag{5.44}$$

Non-dimensionalized static pressure can be calculated by Eq. (5.24) or (5.24') using Eqs. (5.37) and (5.44). The EMS in the laminar VAB model is discussed in Ref.[38].

5.2.3 Turbulent Vortex Solutions

For a turbulent compressible vortex, the parameter a in Eq. (5.25) is set at 0.7 in order to closely reproduce the experimental tangential velocity of turbulent compressible vortex. Three velocity components and pressure are non-dimensionalized using maximum tangential velocity $V_{\theta max}$, not $V_{\theta mc}$.

$$V_r' = \frac{V_r}{V_{\theta\max}}, \qquad V_\theta' = \frac{V_\theta}{V_{\theta\max}}, \qquad V_z' = \frac{V_z}{V_{\theta\max}}, \qquad p' = \frac{p}{\rho_\infty V_{\theta\max}^2} \tag{5.11'}$$

Because of the difference in the representative velocity, representative Mach number in turbulent vortex also differs from Eq. (5.20) as;

$$M_{o\max} = \frac{V_{\theta\max}}{\sqrt{\gamma R T_\infty}} \tag{5.20'}$$

Density and temperature are non-dimensionalized as was shown in Eq.(5.11). The non-dimensional tangential velocity is provided by the following equation;

$$V_\theta' = r' \left(\frac{a+1}{a+r'^4}\right)^m \tag{5.25'}$$

Tangential Mach number is calculated as;

$$M_\theta = \frac{V_\theta}{\sqrt{\gamma RT}} = \frac{V'_\theta}{\sqrt{T'}} M_{o\max} = \frac{V'_\theta}{\sqrt{T'}} \left(\frac{a}{a+1} \right)^m M_{oc} \tag{5.45}$$

Calculated V'_θ using Eq. (5.25') at a = 0.7, is shown in Fig. 5.4. As can be seen in the figure, V'_θ has a rounded peak at around r'=1. Tangential Mach number is calculated by Eq. (5.45) and the results are shown in Fig. 5.5. The figure shows that the maximum Mach number exceeds 1.0 at M_{oc}=1.5.

Mathematical solution of U', defined in Eq. (5.29), obtained from the tangential momentum equation, Eq. (5.31), along with the tangential velocity Eq. (5.25) is

$$U' = \rho' R_e V'_r = -\left(\frac{4 b_1 m r'^7}{b_1 r'^8 + b_2 r'^4 + b_3} + \frac{12 a m r'^3}{b_1 r'^8 + b_2 r'^4 + b_3} \right) \tag{5.46}$$

where,

$$\left.\begin{aligned} b_1 &= -(2m-1) \\ b_2 &= -2a(m-1) \\ b_3 &= a^2 \end{aligned}\right\} \tag{5.47}$$

Calculated V'_r is shown in Fig. 5.6 at R_e = 10^4. The figure shows that radial velocity of the vortex has negative value; the gas flows inward direction to its center line.

Equation (5.30) can be solved using Eqs. (5.29), (5.30) and (5.46) as;

$$H' = \frac{16 m r'^2 \left\{ (b_2 - 3a) b_1 r'^8 + 2 b_1 b_3 r'^4 + 3 a b_3 \right\}}{\left(b_1 r'^8 + b_2 r'^4 + b_3 \right)^2} \tag{5.48}$$

Axial velocity is obtained from Eqs. (5.11") and (5.48) as;

$$V'_z = z' \frac{H'}{\rho' R_e} = \frac{z'}{\rho' R_e} \frac{16 m r'^2 \left\{ (b_2 - 3a) b_1 r'^8 + 2 b_1 b_3 r'^4 + 3 a b_3 \right\}}{\left(b_1 r'^8 + b_2 r'^4 + b_3 \right)^2} \tag{5.49}$$

Calculated V'_z is shown in Fig. 5.7 at z'=1 and R_e = 10^4. The figure shows that V'_z has maximum value at around r'= 0.6 and that V'_z is slightly negative between 1.3 < r' < 2.5.

The energy equation, Eq. (5.32), can be transformed as;

$$\frac{dY'}{dr'} - P_r U'Y' = -P_r(\gamma-1)M_{o\max}^2\left(r'F' + U'V_\theta'^2\right) \tag{5.50}$$

where,

$$Y' = r'\frac{dT'}{dr'} \tag{5.51}$$

In order to integrate Eq. (5.50), λ is introduced as;

$$\lambda = \lambda(r') = \exp\left(-\int_0^{r'} P_r U' dr'\right) \tag{5.52}$$

From Eqs. (5.51) and (5.52), we obtain

$$\frac{1}{\lambda}\left(Y'\frac{d\lambda}{dr'}\right) = -P_r U'Y'$$

Then, Eq. (5.50) can be transformed using above equation as;

$$\frac{dY'}{dr'} + \frac{1}{\lambda}\left(Y'\frac{d\lambda}{dr'}\right) = -P_r(\gamma-1)M_{o\max}^2\left(r'F' + U'V_\theta'^2\right)$$

$$\therefore \quad d\left(Y'\lambda\right) = -P_r(\gamma-1)M_o^2\left(r'F' + U'V_\theta'^2\right)\lambda\, dr'$$

Above equation can be integrated using the boundary conditions about T' in Eq. (5.34) as;

$$Y'\lambda = -P_r(\gamma-1)M_{o\max}^2\int_0^{r'}\left(\eta'F' + U'V_\theta'^2\right)\lambda(\eta')d\eta'$$

$$\therefore \quad \frac{dT'}{dr'} = -P_r(\gamma-1)M_{o\max}^2\frac{\int_0^{r'}\left(\eta'F' + U'V_\theta'^2\right)\lambda(\eta')d\eta'}{r'\lambda(r')}$$

Integration of above equation yields;

$$T' = -P_r(\gamma-1)M_{o\max}^2\int_0^{r'}\left\{\frac{\int_0^{\xi'}\left(\eta'F' + U'V_\theta'^2\right)\lambda(\eta')d\eta'}{\xi'\lambda(\xi')}\right\}d\xi' + C_1 \tag{5.53}$$

The integration constant can be determined using boundary condition of $T' \to 1$ as $r' \to \infty$;

$$1 = -P_r(\gamma-1)M_{o\max}^2\int_0^{\infty}\left\{\frac{\int_0^{\xi'}\left(\eta'F' + U'V_\theta'^2\right)\lambda(\eta')d\eta'}{\xi'\lambda(\xi')}\right\}d\xi' + C_1$$

$$\therefore \quad C_1 = P_r(\gamma-1)M_{o\max}^2\int_0^{\infty}\left\{\frac{\int_0^{\xi'}\left(\eta'F' + U'V_\theta'^2\right)\lambda(\eta')d\eta'}{\xi'\lambda(\xi')}\right\}d\xi' + 1 \tag{5.54}$$

By substituting Eq. (5.54) to Eq. (5.53),

$$T' = 1 + P_r(\gamma - 1) M_{o\max}^2 \left[\int_0^{\infty} \left\{ \frac{\int_0^{\xi'} \left(\eta' F' + U' V_\theta'^2 \right) \lambda(\eta') d\eta'}{\xi' \lambda(\xi')} \right\} d\xi' - \int_0^{r'} \left\{ \frac{\int_0^{\xi'} \left(\eta' F' + U' V_\theta'^2 \right) \lambda(\eta') d\eta'}{\xi' \lambda(\xi')} \right\} d\xi' \right]$$

$$= 1 + P_r(\gamma - 1) M_{o\max}^2 \left[J(\infty) - J(r') \right] \tag{5.55}$$

where,

$$J(r') = \int_0^{r'} \left\{ \frac{\int_0^{\xi'} \left(\eta' F' + U' V_\theta'^2 \right) \lambda(\eta') d\eta'}{\xi' \lambda(\xi')} \right\} d\xi'$$

$$= \int_0^{r'} \left\{ \int_0^{\xi'} \frac{\left(\eta' F' + U' V_\theta'^2 \right) \lambda(\eta')}{\xi' \lambda(\xi')} d\eta' \right\} d\xi' \tag{5.56}$$

The expression of λ, Eq. (5.52), is simplified by substituting Eq. (5.46) to Eq. (5.52) as;

$$\lambda(r') = \exp\left(\int_0^{r'} \frac{4 b_1 m P_r r'^7}{b_1 r'^8 + b_2 r'^4 + b_3} dr' + \int_0^{r'} \frac{12 a m P_r r'^3}{b_1 r'^8 + b_2 r'^4 + b_3} dr' \right)$$

$$= \exp(I_1 + I_2)$$

$$= \exp(I_1) \exp(I_2) \tag{5.57}$$

where,

$$I_1 = 4 b_1 m P_r \int_0^{r'} \frac{r'^7}{b_1 r'^8 + b_2 r'^4 + b_3} dr' = \ln \left\{ \frac{\left(b_1 r'^8 + b_2 r'^4 + b_3 \right)^{\frac{1}{2b_1}}}{\left(\frac{2b_1 r'^4 + b_2 - \sqrt{b_2^2 - 4 b_1 b_3}}{2b_1 r'^4 + b_2 + \sqrt{b_2^2 - 4 b_1 b_3}} \right)^{\frac{b_2}{2b_1 \sqrt{b_2^2 - 4 b_1 b_3}}}} \right\}^{b_1 m P_r} \tag{5.58}$$

$$I_2 = 12 a m P_r \int_0^{r'} \frac{r'^3}{b_1 r'^8 + b_2 r'^4 + b_3} dr' = \ln \left(\frac{2b_1 r'^4 + b_2 - \sqrt{b_2^2 - 4 b_1 b_3}}{2b_1 r'^4 + b_2 + \sqrt{b_2^2 - 4 b_1 b_3}} \right)^{\frac{3 a m P_r}{\sqrt{b_2^2 - 4 b_1 b_3}}}$$

By substituting Eq. (5.58) to Eq. (5.57),

$$\lambda(r')=\left(\frac{2b_1r'^4+b_2-\sqrt{b_2^2-4b_1b_3}}{2b_1r'^4+b_2+\sqrt{b_2^2-4b_1b_3}}\right)^{\frac{3amP_r}{\sqrt{b_2^2-4b_1b_3}}}\left\{\frac{\left(b_1r'^8+b_2r'^4+b_3\right)^{\frac{1}{2b_1}}}{\left(\frac{2b_1r'^4+b_2-\sqrt{b_2^2-4b_1b_3}}{2b_1r'^4+b_2+\sqrt{b_2^2-4b_1b_3}}\right)^{\frac{b_2}{2b_1\sqrt{b_2^2-4b_1b_3}}}}\right\}^{b_1mP_r} \quad (5.59)$$

Calculated T' by Eq. (5.55) is shown in Fig. 5.8 at $R_e = 10^4$. In this calculation, $J(100)$ is approximated to be $J(\infty)$. Figure 5.8 shows that $T > T_\infty$ for $r' > 1.7$, and $T < T_\infty$ for $r' < 1.7$. In addition to that, the larger M_{oc} is, the greater the maximum T' is and the smaller the minimum T' is.

After obtaining gas temperature by Eq. (5.55), gas density can be calculated by Eq. (5.44), which is independent of the value of a and is also applicable to the turbulent vortex.

$$\rho'=\frac{\exp\left[\gamma M_{o\max}^2\left(\int_0^{r'}\frac{V_\theta'^2}{r'T'}dr'-\int_0^{\infty}\frac{V_\theta'^2}{r'T'}dr'\right)\right]}{T'} \quad (5.44')$$

Non-dimensionalized static pressure can be calculated by Eq. (5.24) or (5.24') using Eqs. (5.55) and (5.44'). Calculated static pressure distributions are shown in Fig. 5.9 at $R_e = 10^4$. This figure shows that the larger the Mach number M_{oc} is, the smaller the non-dimensionalized pressure is, at an arbitrary radial position.

Non-dimensionalized total temperature distributions are calculated by Eq. (5.60) at $R_e = 10^4$ under the approximation of $M_r = M_z = 0$, and the results are shown in Fig. 5.10.

$$\frac{T_0}{T_\infty}=\frac{T_0}{T}\frac{T}{T_\infty}\approx\left(1+\frac{\gamma-1}{2}M_\theta^2\right)T' \quad (5.60)$$

Figure 5.10 shows that $T_0 > T_\infty$ for $r' > 0.58$, and $T_0 < T_\infty$ for $r' < 0.58$. In addition to that, the larger M_{oc} is, the greater the maximum T_0' is and the smaller the minimum T_0' is. The maximum T_0' for each M_{oc} is reached at $r' = 1.4$ and is greater than that of T'. On the other hand, the minimum T_0' for each M_{oc} is the same as that of T'. This is because static temperature equals total temperature at $r' = 0$. The calculated results in Fig. 5.10 well describe the temperature separation behavior of VT, although the VAB model is for an unconfined vortex. The thermo-fluid mechanism of having maximum and minimum total temperature in Fig. 5.10 will be examined in detail in Sec. 5.3.

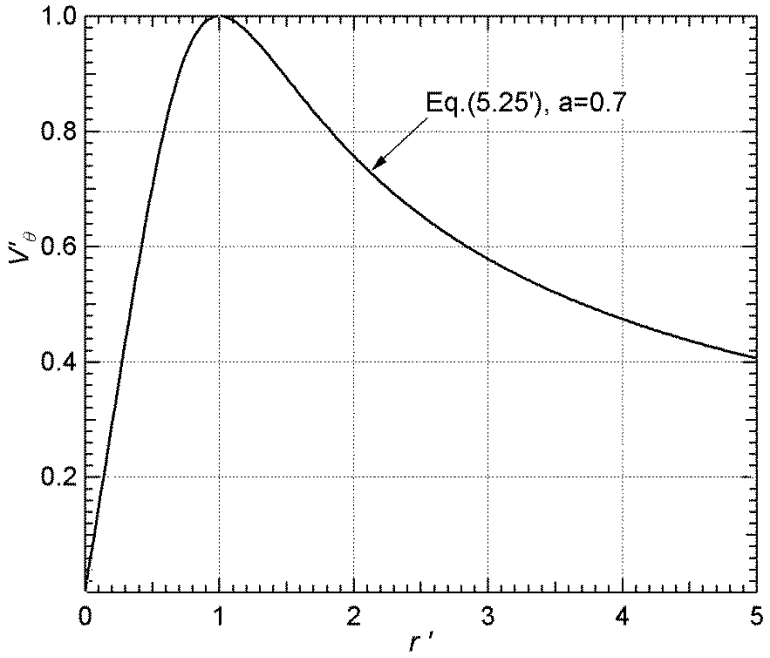

Fig. 5.4 Non-dimensionalized tangential velocity of compressible vortex (turbulent VAB model)

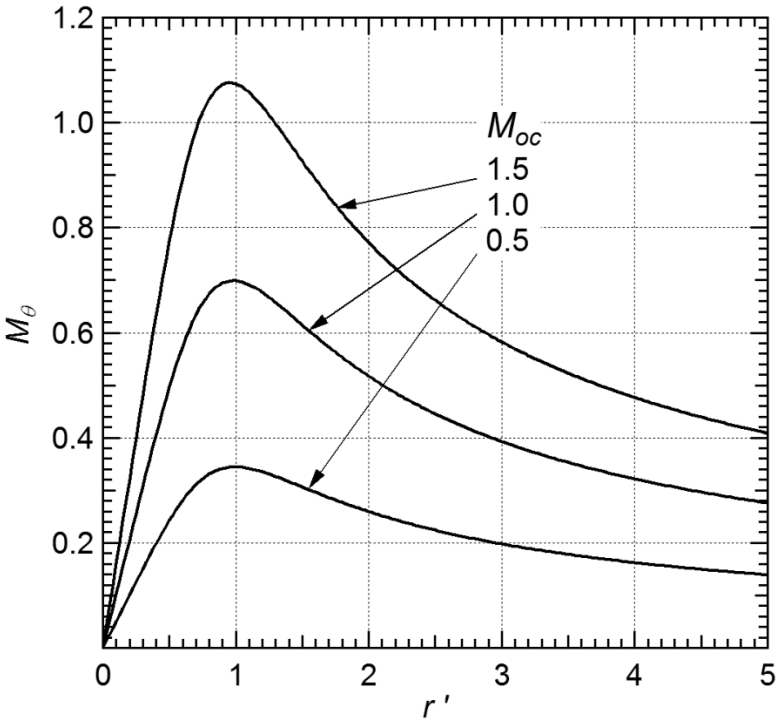

Fig. 5.5 Tangential Mach number of compressible vortex (turbulent VAB model)

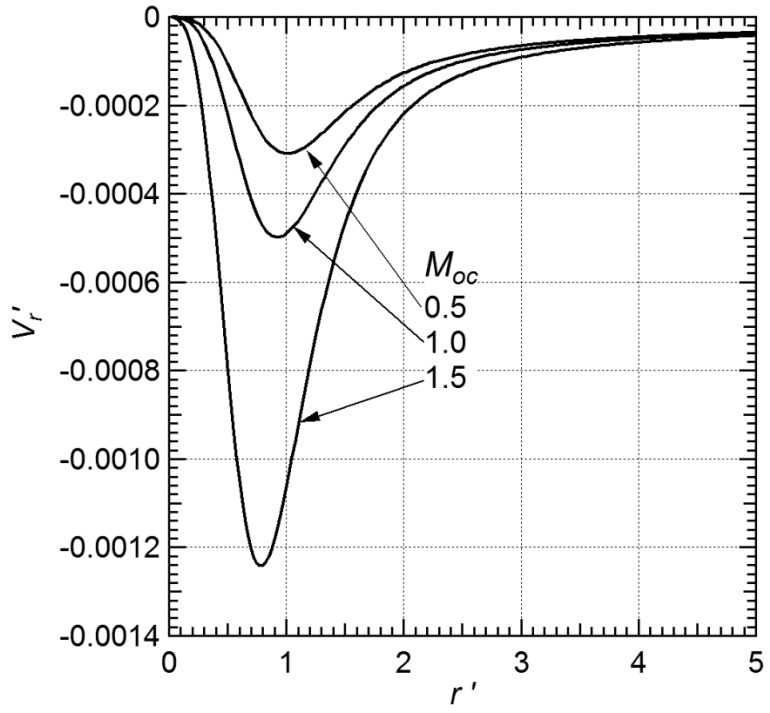

Fig. 5.6 Non-dimensionalized radial velocity of compressible vortex (turbulent VAB model, $R_e = 10^4$)

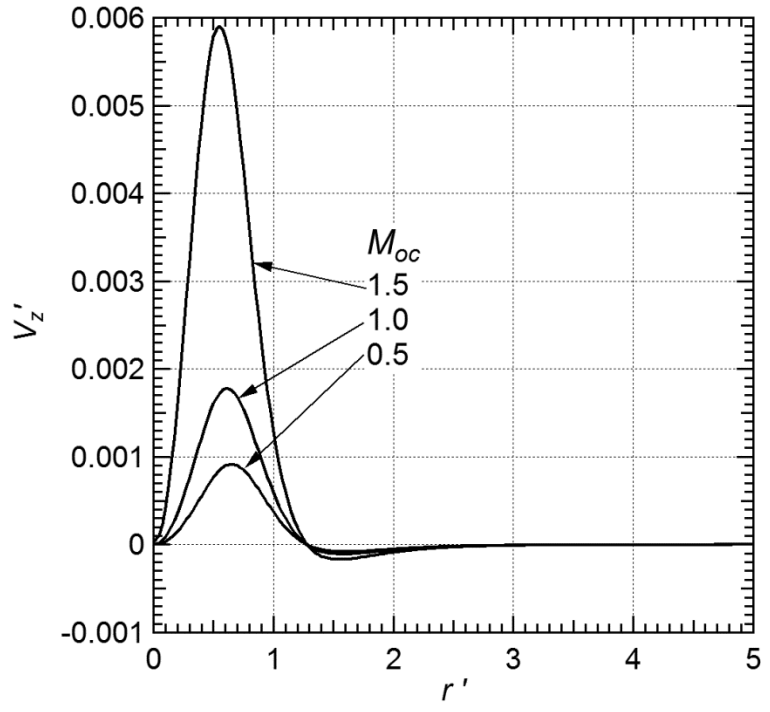

Fig. 5.7 Non-dimensionalized axial velocity of compressible vortex (turbulent VAB model, $z' = 1$, $R_e = 10^4$)

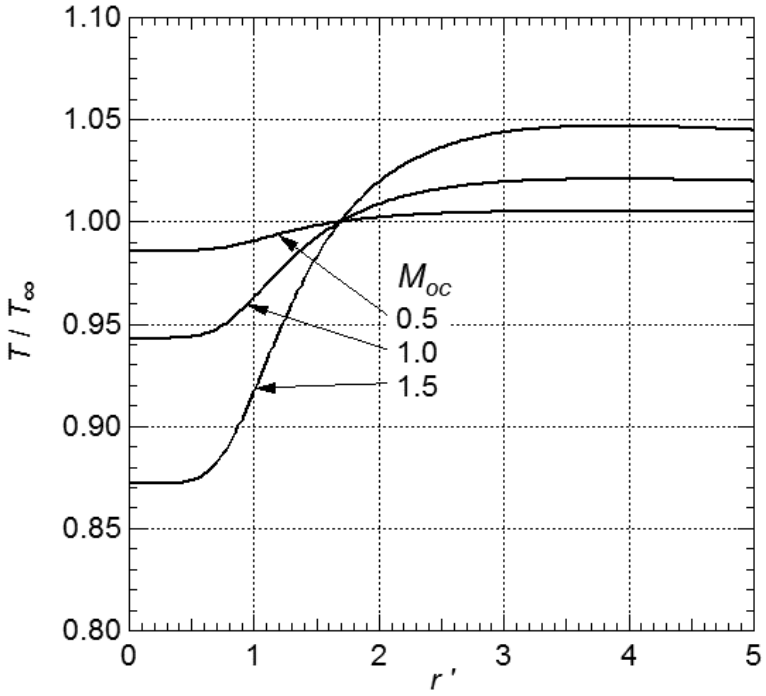

Fig. 5.8 Non-dimensionalized static temperature of compressible vortex (turbulent VAB model, $R_e = 10^4$)

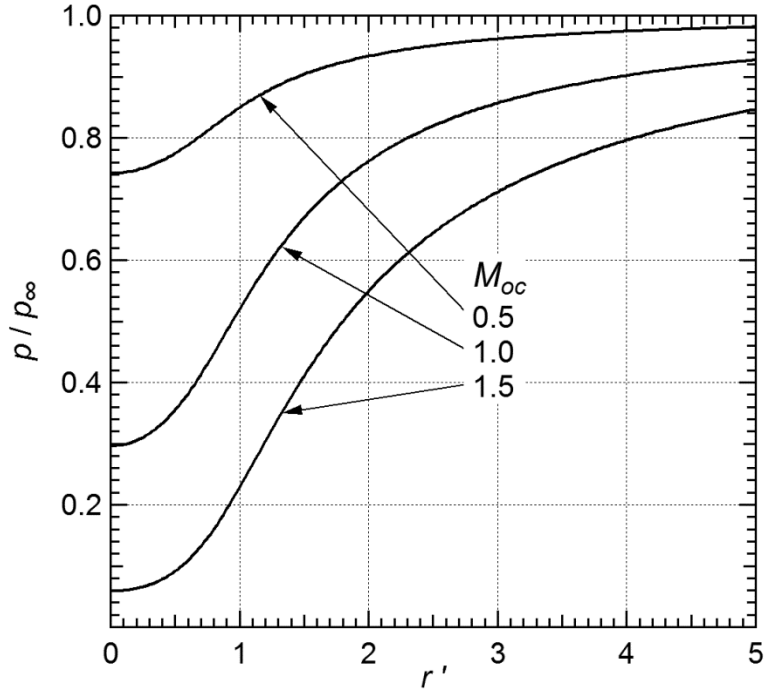

Fig. 5.9 Non-dimensionalized static pressure of compressible vortex (turbulent VAB model, $R_e = 10^4$)

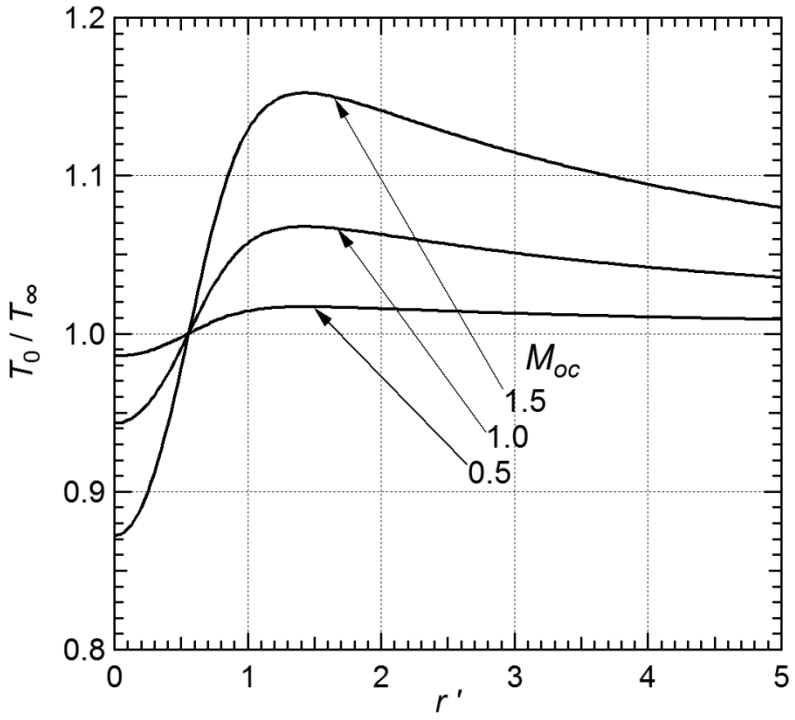

Fig. 5.10 Non-dimensionalized total temperature of compressible vortex (turbulent VAB model, $R_e = 10^4$)

5.2.4 Problems of VAB model

The VAB model of turbulent flow case is described in Ref.[43]. In the research work, $P_r = 0.7$ is used as Prandtl number of air. However, turbulent Prandtl number P_{rt} is not taken into account. It means that only heat conduction occurs as heat transfer in the model, although the flow is assumed to be turbulent. Therefore, P_r is replaced by $P_r + P_{rt}$ in this study. P_{rt} is experimentally known to be around 0.5 in a free jet or central part of a pipe flow, and around 1.0 close to solid wall [51]. In addition, Ref.[43] does not clearly describe how the ESM in a compressible vortex is explained using the VAB model. Therefore, evaluation equation of total temperature variation of fluid element is derived in the next section.

5.3 Thermo-fluid physics in turbulent compressible vortex

5.3.1 Evaluation equation of total temperature variation along stream line

In this subsection, evaluation equation to investigate the total temperature separation in a compressible vortex is derived. The conservation equation of total energy per unit mass is written in Cartesian coordinate as;

$$\frac{De}{Dt} + \frac{D}{Dt}\left(\frac{1}{2}\vec{V}^2\right) = \sum_{i=1}^{4} W_i + \frac{Q}{\rho} \tag{5.61}$$

where, e is the internal energy per unit mass. Kinetic energy per unit mass is written as;

$$\frac{1}{2}\vec{V}^2 = \frac{1}{2}\left(V_x^2 + V_y^2 + V_z^2\right)$$

W_1 in Eq. (5.61) is work done by pressure gradient on the fluid element;

$$W_1 = -\frac{1}{\rho}\left(u\frac{\partial p}{\partial x} + v\frac{\partial p}{\partial y} + w\frac{\partial p}{\partial z}\right) = \frac{1}{\rho}\frac{Dp}{Dt} = -\vec{V}\cdot\frac{1}{\rho}\,\mathrm{grad}\,p \tag{5.62}$$

W_2 in Eq. (5.61) is compression work done by the surrounding gas on the fluid element;

$$W_2 = -\frac{p}{\rho}\left(\frac{\partial u}{\partial x} + \frac{\partial v}{\partial y} + \frac{\partial w}{\partial z}\right) = -\frac{p}{\rho}\,\mathrm{div}\,\vec{V} \tag{5.63}$$

As can be understood from Eq. (5.63), W_2 is zero if the flow is incompressible. W_3 in Eq. (5.61) is work done by viscous force (f_x, f_x, f_x) on the fluid element;

$$W_3 = f_x u + f_y v + f_z w = \vec{V}\cdot\vec{f} \tag{5.64}$$

W_4 in Eq. (5.61) is heat generated per unit time in the fluid element due to viscous

dissipation;

$$W_4 = \frac{\Phi}{\rho} \tag{5.65}$$

where, Φ is the energy dissipation function. Q in Eq. (5.61) is heat transferred from the surrounding gas to the fluid element per unit time. When this is caused by heat conduction, Q is written as follows for the constant thermal conductivity;

$$Q = k\left(\frac{\partial^2 T}{\partial x^2} + \frac{\partial^2 T}{\partial y^2} + \frac{\partial^2 T}{\partial z^2}\right) = k\nabla^2 T \tag{5.66}$$

Navier-Stokes equations in Cartesian coordinate is written as;

$$\frac{D\vec{V}}{Dt} = -\frac{1}{\rho}\,\mathrm{grad}\,p + \vec{f} \tag{5.67}$$

Inner product of $\vec{V}$ and above equation yields;

$$\vec{V}\cdot\frac{D\vec{V}}{Dt} = -\frac{1}{\rho}\vec{V}\cdot\,\mathrm{grad}\,p + \vec{V}\cdot\vec{f}$$

$$\frac{D}{Dt}\left(\frac{\vec{V}^2}{2}\right) = -\frac{1}{\rho}\vec{V}\cdot\,\mathrm{grad}\,p + \vec{V}\cdot\vec{f}$$

$$= W_1 + W_3 \tag{5.68}$$

Subtraction of Eq. (5.68) from Eq. (5.61) yields,

$$\frac{De}{Dt} = W_2 + W_4 + \frac{Q}{\rho}$$

$$= -\frac{p}{\rho}\,\mathrm{div}\,\vec{V} \;+\; \frac{\Phi}{\rho} + \frac{Q}{\rho} \tag{5.69}$$

The mass conservation equation can be written as;

$$\frac{1}{\rho}\frac{D\rho}{Dt} + \mathrm{div}\,\vec{V} = 0 \tag{5.70}$$

The first term in the right hand side of Eq. (5.69) can be reduced to;

$$\frac{p}{\rho}\,\mathrm{div}\,\vec{V} = -\frac{p}{\rho^2}\frac{D\rho}{Dt} = p\frac{D}{Dt}\left(\frac{1}{\rho}\right) \tag{5.71}$$

Substitution of Eq. (5.71) in Eq. (5.69) leads to;

$$\frac{De}{Dt} + p\frac{D}{Dt}\left(\frac{1}{\rho}\right) = \frac{\Phi}{\rho} + \frac{Q}{\rho} \tag{5.72}$$

From the definition of specific enthalpy;

$$h = e + \frac{p}{\rho} \tag{5.73}$$

Differentiation of above equation leads to;

$$\frac{De}{Dt}+p\frac{D}{Dt}\left(\frac{1}{\rho}\right)=\frac{Dh}{Dt}-\frac{1}{\rho}\frac{Dp}{Dt} \tag{5.74}$$

Substitution of Eq. (5.74) in Eq.(5.72) leads to;

$$\frac{Dh}{Dt}-\frac{1}{\rho}\frac{Dp}{Dt}=\frac{\Phi}{\rho}+\frac{Q}{\rho} \tag{5.75}$$

Therefore, assuming specific heat at constant pressure is constant, above equation is written as;

$$c_p\frac{DT}{Dt}=\frac{1}{\rho}\frac{Dp}{Dt}+\frac{\Phi}{\rho}+\frac{Q}{\rho}$$

$$\therefore\quad c_p\frac{DT}{Dt}=\left(-W_1\right)+\frac{\Phi}{\rho}+\frac{Q}{\rho} \tag{5.76}$$

where, W_1 is expressed as follows in cylindrical coordinate;

$$W_1=-\vec{V}\cdot\frac{1}{\rho}\,\mathrm{grad}\,p=-\frac{1}{\rho}\left(V_r\frac{\partial p}{\partial r}+V_\theta\frac{\partial p}{\partial\theta}+V_z\frac{\partial p}{\partial z}\right)=-\frac{1}{\rho}V_r\frac{dp}{dr} \tag{5.77}$$

This equation explains that static temperature variation is determined by the balance between work done by pressure gradient on the fluid element, heat dissipation per unit mass Φ/ρ and transferred heat per unit mass Q/ρ.

Addition of Eq. (5.76) to Eq. (5.68) leads to;

$$\frac{D}{Dt}\left(c_pT+\frac{\vec{V}^2}{2}\right)=W_3+\frac{\Phi}{\rho}+\frac{Q}{\rho} \tag{5.78}$$

Therefore, above equation is written as;

$$\boxed{c_p\frac{DT_0}{Dt}=W_3+\frac{\Phi}{\rho}+\frac{Q}{\rho}} \tag{5.79}$$

where, first term on the right hand side of above equation are expressed as follows in cylindrical coordinate;

$$W_3=\vec{V}\cdot\vec{f}=f_rV_r+f_\theta V_\theta+f_zV_z \tag{5.80}$$

$$f_r=\frac{1}{\rho}\left[\frac{4}{3}\left(\frac{\partial^2V_r}{\partial r^2}+\frac{1}{r}\frac{\partial V_r}{\partial r}-\frac{V_r}{r^2}\right)+\frac{1}{3}\frac{\partial^2V_z}{\partial r\partial z}\right] \tag{5.81}$$

$$f_\theta=\frac{\mu}{\rho}\left(\frac{\partial^2V_\theta}{\partial r^2}+\frac{1}{r}\frac{\partial V_\theta}{\partial r}-\frac{V_\theta}{r^2}\right) \tag{5.82}$$

$$f_z = \frac{\mu}{\rho}\left(\frac{\partial^2 V_z}{\partial r^2} + \frac{1}{r}\frac{\partial V_z}{\partial r}\right) \tag{5.83}$$

In VAB model, $|V_r| << |V_\theta|$ and $|V_z| << |V_\theta|$ are assumed. Therefore Eq. (5.80) is simplified as;

$$W_3 \approx f_\theta V_\theta = \frac{\mu}{\rho} V_\theta \left(\frac{\partial^2 V_\theta}{\partial r^2} + \frac{1}{r}\frac{\partial V_\theta}{\partial r} - \frac{V_\theta}{r^2}\right) \tag{5.84}$$

Second and third terms on the right hand side of Eq. (5.78) in cylindrical coordinate are;

$$\frac{\Phi}{\rho} = \frac{\mu}{\rho}\left\{r\frac{\partial}{\partial r}\left(\frac{V_\theta}{r}\right)\right\}^2 \tag{5.85}$$

$$\frac{Q}{\rho} = \frac{k}{\rho}\left(\frac{\partial^2 T}{\partial r^2} + \frac{1}{r}\frac{\partial T}{\partial r}\right) \tag{5.86}$$

Equation (5.78) clearly shows that total temperature along the flow varies by the balance between viscous shear work per unit mass W_3, heat dissipation per unit mass Φ/ρ and transferred heat per unit mass Q/ρ.

Equations (5.76)-(5.78), (5.84)-(5.86) are non-dimensionalized as same as turbulent vortex, that is,

$$V_r' = \frac{V_r}{V_{\theta\max}}, \qquad V_\theta' = \frac{V_\theta}{V_{\theta\max}}, \qquad V_z' = \frac{V_z}{V_{\theta\max}}$$

$$p' = \frac{p}{\rho_\infty V_{\theta\max}^2}, \qquad \rho' = \frac{\rho}{\rho_\infty}, \qquad T' = \frac{T}{T_\infty}, \qquad T_0' = \frac{T_0}{T_\infty} \tag{5.87}$$

$$r' = \frac{r}{r_c}, \qquad z' = \frac{z}{r_c}$$

The non-dimensional form of Eqs. (5.76), (5.79) and terms included in these equation are written as follows using Eq. (5.87);

$$\frac{DT'}{Dt'} = \frac{(\gamma-1)M_{o\max}^2}{R_e}\left(-W_1' + \frac{\Phi'}{\rho'} + \frac{Q'}{\rho'}\right) \tag{5.88}$$

$$\boxed{\frac{DT_0'}{Dt'} = \frac{(\gamma-1)M_{o\max}^2}{R_e}\left(W_3' + \frac{\Phi'}{\rho'} + \frac{Q'}{\rho'}\right)} \tag{5.89}$$

$$R_e = \frac{\rho_\infty V_{\theta\max} r_c}{\mu} \tag{5.90}$$

$$W_1' = \frac{W_1}{\dfrac{\mu}{\rho_\infty V_{\theta\max} r_c}\dfrac{V_{\theta\max}^3}{r_c}} = \frac{R_e}{\rho'} V_r' \frac{dp'}{dr'} \tag{5.91}$$

$$W_3' = \frac{W_3}{\dfrac{\mu}{\rho_\infty V_{\theta\max} r_c}\dfrac{V_{\theta\max}^3}{r_c}} = \frac{V_\theta'}{\rho'}\left(\frac{d^2V_\theta'}{dr'^2} + \frac{1}{r'}\frac{dV_\theta'}{dr'} - \frac{V_\theta'}{r'^2}\right) \tag{5.92}$$

$$\Phi' = \frac{\Phi}{\dfrac{\mu V_{\theta\max}^2}{r_c^2}} = \left(\frac{dV_\theta'}{dr'} - \frac{V_\theta'}{r'}\right)^2 \tag{5.93}$$

$$Q' = \frac{Q}{\dfrac{\mu V_{\theta\max}^2}{r_c^2}} = \frac{1}{(\gamma-1)M_{o\max}^2}\frac{1}{P_r}\left(\frac{d^2T'}{dr'^2} + \frac{1}{r'}\frac{dT'}{dr'}\right) \tag{5.94}$$

5.3.2 Energy separation mechanism

In this study, P_r in VAB model is replaced by $P_r + P_{rt}$ to examine the ESM of $T_0 > T_\infty$ for $r' > 0.58$, and $T_0 < T_\infty$ for $r' < 0.58$ as was seen in Fig. 5.10, using evaluation equation Eq. (5.89). The working gas selected in this analysis is air. Therefore, the value of P_r and specific heat ratio γ are set at 0.7 and 1.4. Radial distributions of T_0' is calculated by Eq. (5.60) and summation of three terms in the right hand side (RHS) of Eq. (5.89), $(W_3' + \Phi'/\rho' + Q'/\rho')$, are calculated by Eqs. (5.92)-(5.94) at P_{rt} = 0, 0.7 and M_{oc}=1.5. The results are shown in Fig. 5.11. It can be seen in the figure that the maximum T_0' for P_{rt} = 0.7 is larger compared to that of P_{rt} = 0. In addition, T_0 is smaller than T_∞ in the core region of $r' <\sim 0.6$. Most importantly, it should be noted that for $r' > 1.4$ the value of $(W_3' + \Phi'/\rho' + Q'/\rho')$ is small but positive. This explains why T_0' increases from 1.0 as the gas flows inward direction from $r' >> 1$ until the gas reaches $r' = 1.4$. Then, the value of $(W_3' + \Phi'/\rho' + Q'/\rho')$ is 0 at $r' = 1.4$; leading T_0' to reach maximum value at $r' = 1.4$. And then, $(W_3' + \Phi'/\rho' + Q'/\rho')$ falls negative for $r' < 1.4$, causing T_0' to be smaller than 1. In summary, Fig. 5.11 shows that the balance of three elements consisting the RHS of Eq. (5.89) determine the variation of T_0', in other words EMS, in along the stream line.

Figure 5.12 shows the variations of three elements of the RHS of Eq. (5.89), W_3', Φ'/ρ' and Q'/ρ' in radial direction. As can be seen in the figure, W_3' and Φ'/ρ' are negative and positive, respectively, in the entire radial region. Heat transfer Q'/ρ' seems mostly positive; heat is transferred from outer to inner region of the vortex. However, Q'/ρ' is slightly negative in the range of $r' > 1.25$ for P_{rt} = 0 and $r' > 0.88$ for P_{rt} = 0.7. This is because the first term in the

parenthesis of the RHS of Eq.(5.94) is negative in the region and its absolute value is greater than the second term. It can be clearly seen in Fig. 5.12, regardless the value of P_{rt}, that for $r' > 1.4$ Φ'/ρ' (> 0) is greater than summation of W_3' and Q'/ρ', leading the RHS of Eq. (5.89) to be positive in the range of $r' > 1.4$. It means that a hotter gas in the peripheral region of the viscous compressible vortex is mainly generated by heat caused by viscous dissipation. On the other hand, in the range of $r' < 1.4$ the absolute value of W_3' is greater than summation of Φ'/ρ' and Q'/ρ', leading the RHS of Eq. (5.89) to be negative in the range of $r' < 1.4$. It means that a colder gas in the vortex center is mainly generated by W_3'; viscous shear work done on the surface of the fluid element. Since W_3' is negative, the viscous shear work is done by the fluid element to the surrounding gas. Although the present analysis is conducted for unconfined vortex, the above mentioned result, the ESM is mainly caused by viscous shear work in the vortex core, is supported by numerous experimental, theoretical and numerical works [17, 36, 48-49, 52-55].

Non-dimensionalized total temperature at $r' = 0$ can be obtained from Eq. (5.55) as;

$$T_0'(0) = T'(0) = 1 + \left(P_r + P_{rt}\right)(\gamma - 1) M_{o\max}^2 J(\infty) \qquad (5.95)$$

Above equation shows that the static/total temperature at $r' = 0$ depends on P_r, P_{rt}, γ, M_{omax} (or M_{oc}) and $J(\infty)$. From Eq. (5.56), $J(\infty)$ is expressed as;

$$J(\infty) = \int_0^{\infty} \left\{ \int_0^{\xi'} \frac{\left(\eta' F' + U' V_\theta'^2\right)\lambda(\eta')}{\xi' \lambda(\xi')} d\eta' \right\} d\xi' \qquad (5.56')$$

We can see that $J(\infty)$ is a function of P_r and P_{rt}. Calculated $J(\infty)$ is shown in Fig. 5.13 as a function of P_{rt} at $P_r = 0.7$, along with $\left(P_r + P_{rt}\right)J(\infty)$. In the figure, r' = 100 is regarded to be $r' = \infty$. It can be seen in Fig. 5.13 that the value of $\left(P_r + P_{rt}\right)J(\infty)$ is almost constant at around -0.29 in the range of $0.2 < P_{rt} < 1.0$. Therefore, Eq. (5.95) can be simplified as;

$$T_0'(0) = T'(0) \approx 1 - 0.29(\gamma - 1) M_{o\max}^2 \qquad (5.96)$$

Above equation clearly shows that the total temperature at the core of the vortex is smaller for a larger γ and a larger M_{omax} (or M_{oc}), and roughly independent of P_r and P_{rt}.

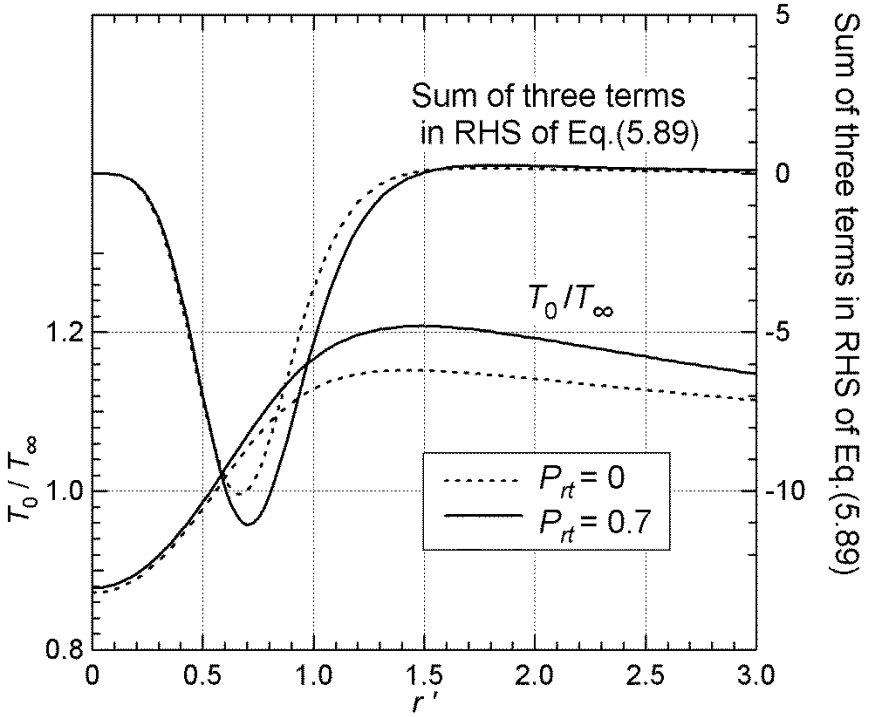

Fig. 5.11 Non-dimensionalized total temperature and summation of three terms in the R.H.S. of Eq.(5.89) at M_{oc}=1.5

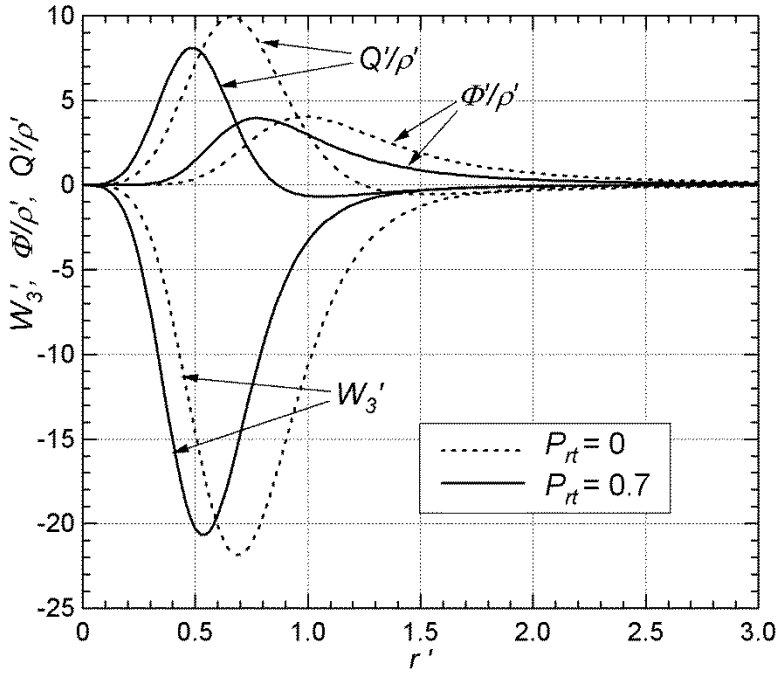

Fig. 5.12 W_3', Φ'/ρ' and Q'/ρ' at M_{oc}=1.5

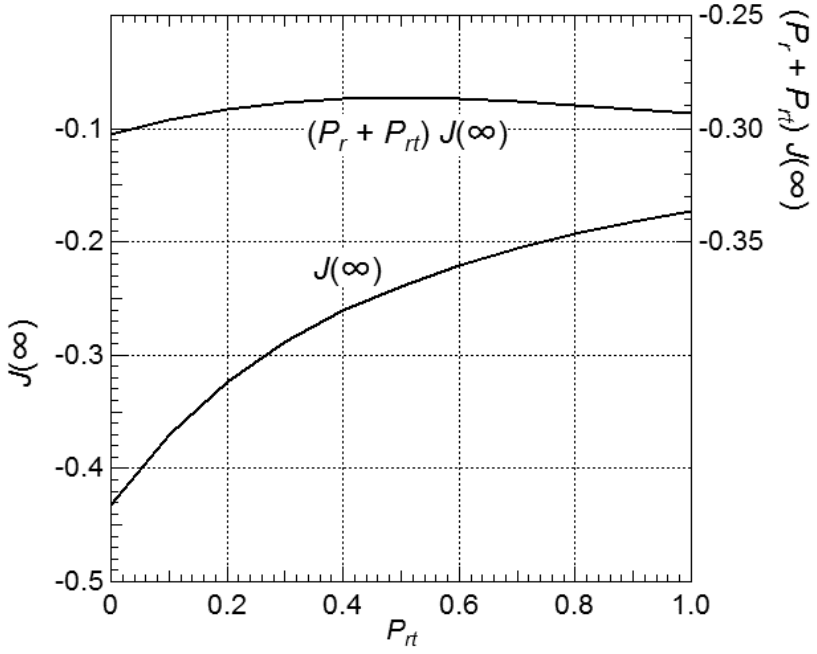

Fig. 5.13 $J(\infty)$ and $(P_r + P_{rt})J(\infty)$ vs P_{rt}

5.4 Conclusions

Mathematical model of an unconfined compressible vortex, VAB model, was examined in detail, expecting that the essential ESM of unconfined vortex is almost the same as the confined vortex; uni-flow/counter-flow VT. Total temperature distribution along the flow of the VAB model was especially investigated using total energy conservation equation as an evaluation equation, in order clarify the ESM in the compressible vortex. Main conclusions obtained by the present analysis are described as follows;

1) A hotter gas in the peripheral region of the vortex is mainly generated by heat generated by viscous dissipation.
2) A colder gas in the vortex center is mainly generated by W_3'; viscous shear work done on the surface of the fluid element to the surrounding gas. Since W_3' is negative, the viscous shear work is done by the fluid element to the surrounding gas. On the other hand, viscous dissipation and heat transfer towards the inner core have effects to raise the total temperature of the core region to some extent.
3) Total temperature in the core is smaller for a larger γ and a larger M_{omax} (or M_{oc}), and roughly independent of the summation of P_r and P_{rt}.

6. Conclusions

As explained in Chapter 1, the objective of this study is to clarify the energy separation mechanism (ESM) of VT. For the purpose of this objective, the experimental and analytical studies were carried out.

In order to clarify the flow structure of the cold exit flow, the total temperature and Pitot pressure of a cold flow center were measured. In addition, two simple flow visualization techniques were used to observe the flow at the cold exit, and the mixing temperature of cold and hot flows were measured to clarify the performance of VT used in this research. Main conclusions obtained in the present research are summarized as follows.

6.1 Total temperature probe

To measure the total temperature at the cold exit, 3 different probes were created. Those probes were named as Type 1, 2, and 3, respectively, and created by inserting a thermocouple into an acrylic tube with the tip of the tube protruding from the rod. The tip of the Type 3 is covered with sponge to decelerate the flow at the tip of the thermocouple. An evaluation experiment was conducted in a subsonic air jet flow from a converging nozzle to determine the relationship between the measurement angle and measured temperature. The results are summarized as follows;

1) The Type 3 total temperature probe has the smallest measurement error; the largest measurement errors of Type 1, 2, and 3 are −1.3°C, −1.1°C, and −0.7°C, respectively.
2) The effect of the measurement angle on the measured total temperature is negligibly small for Type 3.
3) Type 3 is chosen to measure the total temperature of cold and hot flows due to its smallest measurement error, and the ability to decelerate the flow at the tip of the thermocouple.

6.2 Pressure measurement

A pressure measurement using a Pitot pressure probe was conducted along the centerline at 3mm (x = 3mm) downstream of the cold exit. The inlet pressure p_{in}

was varied from 0.2 to 0.6 MPa. The cold fraction ε was varied from 0.1 to 1.0. The results are summarized as follows;

1) At an arbitrary inlet pressure, the Pitot pressure decreases from positive gauge value to negative gauge value when the cold fraction decreases.
2) The existence of a negative gauge pressure implies the possible occurrence of a flow reversal around the center of the cold flow.

6.3 Flow visualization

Two flow visualization techniques were created. The first technique uses an oil paint droplet, on a 0.75mm-diameter needle. The oil paint droplet on the needle was positioned along the centerline of the cold flow at x = 3mm from the cold exit. Another flow visualization technique uses a 0.70mm-diameter needle (SUS tube) with 10 small holes which can exudate colored oil (exudation needle). The exudation needle was inserted into the cold flow along the centerline and traversed along x direction. The results are summarized as follows;

1) The oil paint droplet moves downstream, upstream, or remains at one place, depending on the cold fraction.
2) The movement of the oil droplet in the downstream direction represents a direct flow. The movement of the oil droplet in the downstream direction represents a reversed flow. The static oil paint droplet indicates a stagnation point, which corresponds to the boundary point of direct/reversed flow.
3) At an arbitrary inlet pressure and x = 3mm, a direct flow inverts to a reversed flow at a specific value of the cold fraction when the cold fraction is decreased from 1.0.
4) The inversion of the cold flow direction at center line occurs at a smaller value of cold fraction and at a larger inlet pressure. It should be noted that, the reversed flow occurs when the Pitot pressure at x = 3mm is lower than atmospheric pressure.
5) The axial length of the reversed flow measured from the cold exit, x_s, increases as the cold fraction decreases.

6.4 Temperature measurement

A temperature measurement using the Type 3 probe was conducted along the

centerline at x = 3mm downstream from the cold exit. In addition, the mixing temperature of cold and hot flows were measured to clarify the performance of VT. The inlet pressure was varied from 0.2 to 0.6 MPa. The cold fraction was varied from 0.1 to 1.0. The results are summarized as follows;

1) At an arbitrary inlet pressure, the temperature differences between inlet temperature and cold flow temperature at the center of cold exit, $\Delta T_{t,cold}$ is almost constant at x = 3mm when the reversed flow occurs regardless of the value of the cold fraction.
2) On the other hand, when the direct flow occurs in the cold flow, $\Delta T_{t,cold}$ increases as the cold fraction decreases from 1.0 at an arbitrary inlet pressure. In other words, when $\Delta T_{t,cold}$ is plotted on a contour map with inlet pressure as horizontal axis and cold fraction as vertical axis, the maximum temperature differences measured at x = 3mm along the center line occurs around the boundary of direct/reversed flow or smaller cold fraction area under the boundary line at an arbitrary inlet pressure.
3) The mixing temperature of cold flow, $\Delta \bar{T}_{t,cold}$, increases as the cold fraction decreases. The mixing temperature of hot flow, $\Delta \bar{T}_{t,hot}$, decreases as the cold fraction decreases.
4) The maximum cooling capacity of VT is obtained at p_{in} = 0.6MPa and ε = 0.4.
5) The non-dimensional heat loss of VT is smaller than $\pm$1.6%, which is relatively small and negligible.

6.5 Mathematical model analysis of compressible vortex flow

A mathematical model analysis of an unconfined turbulent compressible vortex flows, VAB model, was examined in detail. Total temperature distribution along the flow obtained by the VAB model was investigated using total energy conservation equation as an evaluation equation, in order clarify the ESM in the turbulent compressible vortex. The results are summarized as follows;

1) The total temperature along the stream line varies depending on the balance between viscous shear work, viscous dissipation and heat transfer.
2) A hotter gas in the peripheral region of the vortex is mainly generated by heat caused by viscous dissipation.
3) A colder gas in the vortex center is mainly generated by viscous shear work

done on the surface of the fluid element to the surrounding gas. Since viscous shear work is negative, the viscous work is done by the fluid element to the surrounding gas. Viscous dissipation and heat transfer towards the inner core have effects to raise the total temperature of the core region to some extent.

4) The total temperature in the core is smaller for a larger specific heat ratio gas and at a larger representative Mach number of the vortex. In addition, the total temperature in the core roughly independent of the summation of laminar Prandtl number and turbulent Prandtl number.

6.6 Expected flow pattern and ESM

From the results of experiment and mathematical model analysis conducted in the present research, in addition to the numerical results of Ref.[36], the expected flow pattern and EMS of counter flow VT are summarized as follows;

1) A recirculation vortex is formed inside of the cold exit pipe.

2) The axial length of the recirculating vortex increases when the cold fraction decreases at an arbitrary inlet pressure.

3) When the cold fraction decreases from unity at an arbitrary inlet pressure, the pressure at the center of vortex chamber decreases since the axial length of reversed flow increases. A lower pressure in the vortex chamber means a lower static/total temperatures at the core of vortex chamber and a higher static/total temperatures at the outer region of the vortex in the vortex chamber.

4) When the inlet pressure increases at an arbitrary cold fraction, the tangential velocity increases, which results in a lower static/total temperatures at the core of the vortex chamber and a higher static/total temperatures at the outer region of the vortex in the vortex chamber.

References

1 G.J. Ranque, Experiences Sur la Detente Giratoire Avec Productions Simultanees d´un Echappement d´Air Chaud et d´un Echappement d´Air Froid, Journal de Physique et Le Radium, Vol.4, 1933, pp.112–114.

2 R. Hilsch, The Use of Expansion of Gases in a Centrifugal Field as Cooling Process, The Review of Scientific Instruments, Vol.18, pp.108–113, (1947).

3 S. Eiamsa-ard and P. Promvonge, Review of Ranque-Hilsch Effects in Vortex Tubes, Renewable and Sustainable Energy Rev., Vol. 12, 2008, pp.1822–1842.

4 D. Bizzarri, P. Hendrick, G. Heyen and P. Ngendakumana, Propulsion vehicle integration for reusable launcher using in-flight oxygen collection, Original Research Article, Aerosp. Sci. Technol., Vol. 12, No. 6, 2008, pp. 429–435.

5 H. Kubota, et al. (Toyota Industries Corporation), Exhaust Device and Exhaust Method in Internal Combustion Engine, Japanese Unexamined Patent Application Publication No.2010–196507.

6 K. Dincer, A. Avci and S. Baskaya, A. Berber, Experimental investigation and exergy analysis of the performance of a counter flow Ranque-Hilsch vortex tube with regard to nozzle cross-section areas, Int. J. Refrigeration, Vol. 33, 2010, pp. 954–962.

7 H. Takahama, Energy Separation of Gas by Vortex Tube, Tran. J. Soc. Mech. Eng., Vol. 68, No. 560, 1965, pp. 1255–1263 (in Japanese).

8 O. Aydin and B. Markal, A New Vortex Generator Geometry for a Counter-Flow Ranque-Hilsch Vortex Tube, Appl. Therm. Eng., Vol.30, 2010, pp.2505–2510.

9 H. Takahama, H. Yokosawa and T. Ohara, Studies on Vortex Tubes (Shortening of VT using diverging vortex chamber), Trans. J. Soc. Mech. Eng., Ser. B, Vol. 46, No. 404, 1977, pp.584–592 (in Japanese).

10 S.U. Nimbalkar, Quantitative observations on multiple flow structures inside Ranque-Hilsch vortex tube, PhD thesis, Graduate School New Brunswick, 2009.

11 S. Eiamsa-ard, Experimental investigation of energy separation in a counter-flow Ranque–Hilsch vortex tube with multiple inlet snail entries, Int. Commun. Heat and Mass Transfer, Vol. 37, 2010, pp. 637–643.

12 C.D. Fulton, Ranque's Tube, Refrigerating Engineering, Vol. 58, No. 5, pp. 473–479, 1950

13 J.E. Lay, An experimental and analytical study of vortex flow temperature separation by superposition of spiral and axial flows part 1 & part 2, Transactions of ASME: J. Heat Transfer, Vol. 81, No. 3, 1959, pp. 202–222

14 M. Kurosaka, Acoustic streaming in swirling flow and the Ranque-Hilsch vortex-tube effect, J. Fluid Mech., Vol. 124, 1982, pp. 139–172.

15 K. Stephan, S. Lin, M. Durst, F. Huang and D. Seher, An investigation of energy separation in a vortex tube. Int. J. Heat Mass Transfer , Vol. 26, 1983, pp. 341–348.

16 Y. Xue, M. Arjomandi and R. Kelso, Experimental study of the flow structure in a counter flow Ranque–Hilsch vortex tube, Int. J. Heat Mass Transfer., Vol. 55, 2012, pp. 5853–5860.

17 U. Behera, P.J. Paul, K. Dinesh and S. Jacob, Numerical investigations on flow behaviour and energy separation in Ranque–Hilsch vortex tube, Int. J. Heat Mass Transfer., Vol. 51, 2008, pp. 6077–6089.

18 G.J. Ranque, Method and apparatus for obtaining from a fluid under pressure two currents of fluids at different temperatures, United States Patent Office, Serial no. 646020, 1934.

19 E. Hihara , Non-Fron Technologies – New Trend of Natural Refrigerant－, Ohmsya, Ltd., 2004, pp. 28 (in Japanese).

20 H. Takahama, Studies on Vortex Tubes (Experiments on Separation Efficiency and Velocity/Temperature Distributions), Tran. J. Soc. Mech. Eng., Vol. 30, No. 219, 1964, pp. 1419–1427 (in Japanese).

21 M.H. Saidi and M.S. Valipour, Experimental modeling of vortex tube refrigerator, Appl. Therm. Eng. , Vol. 23, pp. 1971–1980, 2003.

22 Upendra Behera et al., CFD analysis and experimental investigations towards optimizing the parameters of Ranque–Hilsch vortex tube, Int. J. Heat Mass Transfer., Vol. 48, 2005, pp. 1961–1973.

23 S.U. Nimbalkar, M.R. Muller, An experimental investigation of the optimum geometry for the cold end orifice of a vortex tube, Appl. Therm. Eng., Vol. 29, 2009, pp. 509–514.

24 Y.T. Wu, Y. Ding, Y.B. Ji, C.F. Ma and M.C. Ge, Modification and Experimental Research on Vortex Tube, Int. J. Refrigeration, Vol. 30, 2007, pp.1042–1049.

25 B. Markal, O. Aydin and M. Avci, An Experimental Study on the Effect of the Valve Angle of Counter-Flow Ranque-Hilsch Vortex Tubes on Thermal Energy Separation, Exp. Therm. Fluid Sci., Vol.34, 2010, pp.966–971.

26 Kun Chang et al., Experimental investigation of vortex tube refrigerator with a divergent hot tube, Int. J. Refrigeration, Vol. 34, 2011, pp. 322–327.

27 M. Avci, The Effects of Nozzle Aspect Ratio and Nozzle Number on the Performance of the Ranque-Hilsch Vortex Tube, Appl. Therm. Eng., Vol. 50, 2013, pp.302–308.

28 O. Uluer, V. Kirmaci and S. Atas, Using the artificial neural network model for modeling the performance of the counter flow vortex tube, Expert Syst. Appl., Vol. 36, 2009, pp. 12256–12263.

29 M.E. Korkmaz, L. Gumusel and B. Markal, Using artificial neural network for predicting performance of the Ranque-Hilsch vortex tube, Int. J.Refrigeration, Vol. 35, 2012, pp. 1690–1696.

30 H. Khazaei, A.R. Teymourtash and M. Malek-Jafarian, Effects of gas properties and geometrical parameters on performance of a vortex

tube , Scientica Iranica B, Vol. 19, Vo. 3, 2012, pp. 454–462.

31 Y. Xue, M Arjomandi and R. Kelso, Flow visualization to determine the flow structure in a vortex tube, 17th Australasian Fluid Mechanics Conference, Auckland, New Zealand, 2010.

32 Y. Xue, M Arjomandi and R. Kelso, A critical review of temperature separation in a vortex tube, Exp. Therm. Fluid Sci., Vol. 34, 2010, pp. 1367–1374.

33 O. Aydin and M. Baki, An experimental study on the design parameters of a counter flow vortex tube, Energy, Vol. 31, 2006, pp. 2763–2772.

34 E.M. Winkler, Stagnation temperature probes for use at high supersonic speeds and elevated temperatures, Aeroballistic Research Report 256, 1954.

35 Mohammed Ameri and Behrooz Behnia, The Study of Key Design Parameters Effects on the Vortex Tube Performance, J. Therm. Sci., Vol.18, 2009, pp.370–376.

36 T. Dutta, K.P. Sinhamahapatra, and S.S. Bandyopadhyay, Numerical Investigation of Gas Species and Energy Separation in the Ranque-Hilsch Vortex Tube using Real Gas Model, Int. J. Refrigeration, Vol.34, 2011, pp.2118–2128.

37 Mohd Hazwan bin Yusof and H. Katanoda; Measurement of Reverse Flow Generated at Cold Exit of Vortex Tube , Proceedings of International Conference on Fluid Mechanics, Heat Transfer and Thermodynamics 2014, 2014, pp. 1248–1251.

38 H. Katanoda and Mohd Hazwan bin Yusof; Energy Separation Mechanism in Uni-Flow Vortex Tube using Compressible Vortex Flow, Proceedings of International Conference on Fluid Mechanics, Heat Transfer and Thermodynamics 2014, 2014, pp.1252–1255.

39 H. Takahama and N. Soga, Studies or Vortex Tubes: 2nd Report, (1) Reynolds Number (2) The Effects of the Cold Air Rate and the Partial Admission of Nozzle on the Energy Separation, Tran. J. Soc. Mech. Eng., Vol. 31, No. 225, 1965, pp. 787–794 (in Japanese).

40 B. Ahlborn and S. Groves, Secondary flow in a vortex tube, Fluid Dyn. Res., Vol. 21, No. 2, 1997, pp. 73–86.

41 L. M. Mack, The compressible viscous heat-conducting vortex, J. Fluid Mech., Vol. 8, 1958, pp. 284–292.

42 G. H. Vatistas and Y. Aboelkassem, Extension of the Incompressible n=2 Vortex into Compressible, AIAA J., Vol. 44, No. 8, 2006, pp. 1912–1915.

43 G. S. Badwal, A Model for Turbulent Compressible Vortices, Master's Degree Thesis, Concordia University, 2014.

44 M. Sibulkin, Unsteady, Viscous, Circular Flow, Part III. Application to the Ranque–Hilsch Vortex Tube, J. Fluid Mech., Vol. 12, 1962, pp. 269–293.

45 H. Takahama, Studies on Vortex Tubes: 3rd Report, Variations of Velocity, Temperature and Energy with Axial Distance, and Mechanism of Energy Separation, Tran. J. Soc. Mech. Eng., Vol. 32, No. 235, 1966, pp. 503–510 (in Japanese).

46 B. Ahlborn, et al., Limits of Temperature Separation in a Vortex Tube, J. Phys. D: Appl. Phys., Vol. 27, No. 3, 1994, pp. 480–488.

47 T. Amitani, T. Adachi and T. Kato, A Proposal for Temperature Separation Mechanism in a Large Scale Vortex Tube, Tran. J. Soc. Mech. Eng., Ser. B, Vol. 49, No. 440, 1983, pp. 877–884 (in Japanese).

48 N. F. Aljuwayhel, G.F. Nellis and S. A. Klein, Parametric and Internal Study of the Vortex Tube using a CFD Model, Int. J. Refrigeration, Vol. 28, No. 3, 2005, pp. 442–450.

49 T. Dutta, K. P. Sinhamahapatra, and S. S. Bandyopdhyay, Comparison of Different Turbulence Models in Predicting the Temperature Separation in a Ranque-Hilsch Vortex Tube, Int. J. Refrigeration, Vol. 33, 2010, pp. 783–792.

50 Y. Xue, M. Arjomandi and R. Kelso, Visualization of the Flow Structure in a Vortex Tube, Exp. Therm. Fluid Sci., Vol. 35, No. 8, 2011, pp. 1514–1521

51 O. Kuga, Turbulent Prandtl number of Turbulent Heat Convection in Circular Pipe, Tran. J. Soc. Mech. Eng., Vol. 31, No. 223, 1965, pp. 470–474 (in Japanese).

52 R. Kassner and E. Knoernschild, Friction Laws and Energy Transfer in Circular Flow, Wright–Patterson Air Force Base, Technical Report F-TR-2198ND OH, 1948.

53 O.V. Kazantseva, Sh. A. Piralishvili and A. A. Fuzeeva, Numerical simulation of swirling flows in vortex tubes, High Temp., Vol. 43, No. 4, 2005, pp. 608–613.

54 C.U. Linderstrom-Lang, The Three-Dimensional Distributions of Tangential Velocity and Total-Temperature in Vortex Tubes, J. Fluid Mech., Vol. 45, 1971, pp. 161–187.

55 R. G. Deissler and M. Perlmutter, Analysis of the Flow and Energy Separation in a Vortex Tube, Int. J. Heat Mass Transfer, Vol. 1, No. 2-3, 1960, pp. 173–191.

Acknowledgements

I wish to express my sincere gratitude to everyone who contributed to the completion of my study.

Alhamdulillah. I would like to thank Allah (God) for giving me this opportunity to study here in Kagoshima University. I learned a lot from Japanese people since I came here on 2006. I would like to thank my government, Malaysia for giving scholarship to Malaysian student like me to further our study abroad with its “Look East Policy”.

I would like to express my gratitude to my main supervisor, Professor Hiroshi Katanoda, who continuously gives me excellent guides through my study. I learned a lot from my main supervisor. I will never forget his passion to teach me everything he knows. I would like to acknowledge the excellent guides provided by Professor Hideo Ide, Professor Minoru Fukuhara, and Professor Eiji Kinoshita, who keeps giving me a great comments and guidance on my research. A special thanks to Associate Professor Chungpyo Hong for sharing his knowledge. Great thanks to my lab colleagues for their cooperation during my study here. Also thank to the staffs of Mechanical Engineering Department and Graduate School of Science and Engineering, Kagoshima University.

I also would like to thank my father, Yusof bin Hj. Talib, my mother, Romlah binti Jusoh, and my 6 siblings for their support throughout my study in Japan.

I also would like to send my deepest gratitude to my wife, Nur Syajaah binti Shahrin, and my daughter, Safa binti Mohd Hazwan, for giving me tremendous supports and encouragement throughout my study career.